Politecnico di Torino

ScuDo
Scuola di Dottorato ~ Doctoral School
WHAT YOU ARE, TAKES YOU FAR

Doctoral Dissertation
Doctoral Program in Energy Engineering (35^{th}cycle)

Adaptive Variable Structure Control System for Attitude Spacecraft Applications

By

Mauro Mancini

******

Supervisor(s):
Prof. Elisa Capello, Supervisor
Dr. Dimitri Peaucelle, Co-Supervisor
Prof. Luca Zaccarian, Co-Supervisor

Doctoral Examination Committee:
Prof. Dolores Alejandra Ferreira De Loza , Referee, Instituto Politecnico Nacional
Prof. Andrea Serrani, Referee, Ohio State University
Prof. Andrea Garulli, Università degli Studi di Siena
Prof. Giorgio Guglieri, Politecnico di Torino
Prof. Carlo Novara, Politecnico di Torino

Politecnico di Torino
2023

Declaration

I hereby declare that, the contents and organization of this dissertation constitute my own original work and does not compromise in any way the rights of third parties, including those relating to the security of personal data.

Mauro Mancini
2023

* This dissertation is presented in partial fulfillment of the requirements for **Ph.D. degree** in the Graduate School of Politecnico di Torino (ScuDo).

To any PhD students, my dear comrades.

Abstract

Whatever the mission tasked to a satellite (observation of the universe, Earth monitoring, rendezvous and docking), it is crucial for its success that the satellite has the proper attitude, i.e. the proper orientation in space. So, satellites have a dedicated on-board system that is responsible for generating the desired attitude, estimating the true attitude and controlling the actuators, to change the orientation in the desired direction. This role is assigned to the Guidance, Navigation, and Control (GNC) system, and it is clear from the description that the overall attitude error of a spacecraft consists of both the estimation and control errors.

The main focus of this thesis is the design of an Attitude Control System (ACS), whose requirements certainly depend on the space mission, but which usually provides a tree-axis stabilisation. Therefore, an ACS is usually required for both manoeuvring from one desired orientation to another and maintaining the desired orientation. Indeed, a space mission often involves multiple pointing modes. Moreover, the space environment should be counteracted, to avoid deviation of the satellite attitude during manoeuvres. For this reason, the attitude control algorithms developed in this thesis were designed to ensure both fast spacecraft manoeuvrability and fine pointing accuracy. Since attitude dynamics is inherently non-linear and characterised by uncertain parameters and unmodelled dynamics, robust non-linear control techniques based on Variable Structure Control (VSC) with sliding mode are considered for the ACS. Sliding Mode Control (SMC) offers high robustness against external disturbances and parametric uncertainties, but it suffers from chattering, i.e. high-frequency oscillations in the closed-loop dynamics. Therefore, techniques to eliminate chattering are addressed in the controller design. In addition, real actuators, i.e. reaction wheels, with limited actuating power are taken into account for the application of the control torques calculated by the ACS. Therefore, the attitude control algorithms are designed in such a way that the output of the control law does

not overload the actuators, thus actuator saturations are avoided even considering parametric uncertainties.

A further difficulty in tackling the design of the ACS is the flexibility of the satellite's structures. Indeed, modern spacecraft often have appendages with low stiffness, so they do not behave like a rigid body. The coupling between the flexibility of the structure and the attitude dynamics causes (I) vibrations of the flexible bodies and (II) internal torques disturbing the attitude dynamics. To study these effects, a three degree-of-freedom attitude dynamics simulator is constructed, with a mathematical model that includes uncertainties on the inertia tensor and a coupling matrix between the satellite's attitude dynamics and the flexible dynamics of the appendages. In addition, this simulator also includes the dynamics and saturations of the actuators and is used to validate the control algorithms designed in the thesis through numerical simulations.

Finally, the main outcome of this thesis is the development of an innovative control algorithm by combining adaptive control techniques and SMC. First the stability of the novel adaptive SMC algorithm is proven using Lyapunov functions, and then it is tested within the attitude dynamics simulator through extensive numerical simulations. The comparison between the results obtained with adaptive SMC and classical SMC shows that the combined use of adaptive control and SMC improves the robustness of the closed-loop system, the convergence speed and the pointing accuracy. In addition, both classical SMC and adaptive SMC are applied to a high fidelity simulator of the DEMETER spacecraft from CNES. In this case, the algorithms are designed to replicate the switching control law implemented on the real satellite, and the results show that the adaptive SMC developed in this thesis project succeeds in avoiding actuator saturations and thus steering to zero the attitude error of the DEMETER, while the classical SMC fails in this task.

Contents

List of Figures

List of Tables

Nomenclature

Acronyms / Abbreviations

ACS Attitude Control System

AOCS Attitude and Orbit Control System

BLFOSM Boundary-Layer First Order Sliding Mode

BLSMC Boundary-Layer Sliding Mode Control

CNES Centre National d'Études Spatiales

DOF Degree Of Freedom

ECI Earth-Centered Inertial

FEM Finite Element Method

FOC Fractional-Order Control

FOSM First Order Sliding Mode

FTSM Fast Terminal Sliding Mode

GNC Guidance Navigation and Control

ISMC Integral Sliding Mode Control

LQR Linear Quadratic Regulator

LVLH Local Vertical Local Horizontal

NDI Nonlinear Dynamic Inversion

NFTSM Nonsingular Fast Terminal Sliding Mode

NTSM Nonsingular Terminal Sliding Mode

PD Proportional-Derivative

RWs Reaction Wheels

SDRE State Dependent Riccati Equation

SMC Sliding Mode Control

SOSM Second Order Sliding Mode

STW Super-Twisting

TSM Terminal Sliding Mode

VSC Variable Structure Control

Chapter 1

Introduction

This chapter aims to introduce the topics addressed in the course of the doctoral project described by this thesis. Since the key topic of the work performed is the automatic attitude control for satellites, the importance of this task and also of the on-board system that is called upon to perform it are first introduced. After that, the close relationships between the automatic attitude control function and other functions performed by spacecraft on-board systems are described. Next, the problems a control designer faces in deriving automatic attitude control algorithm for satellites are briefly introduced, and then the control techniques studied by the scientific community in this field are presented. The introduction finally concludes by presenting the outline of the thesis.

Addressing the problem of the orientation, or also named attitude, of a satellite moving in space is crucially important in space missions. Indeed, a spacecraft consists of a number of instruments which are required to be pointed in specific directions for the space mission to be successful. These will include solar arrays to point towards the Sun, thermal radiators to point towards deep space, antennas to point towards ground stations, thrusters to point where thrust is desired, and of course the payload pointing requirement that is the reason for the existence of the space mission. Certainly, some of these instruments can benefit from pointing mechanisms that allow them to move arbitrarily with respect to the satellite's structure, but the orientation of all of them is more or less constrained by the attitude of the satellite's main structure. Thus, based on both the assembly of these objects on the satellite structure and the orbit designated for it, a specification for the orientation of the

satellite structure will emerge.
Depending on the mission specification, either active control or passive stabilisation of the attitude can be opted for. Passive attitude stabilisation is usually achieved by providing gyroscopic stiffness to the satellite (spinning spacecraft, momentum storage devices) or by exploiting the gravitational gradient (gravity-gradient stabilization), and has the function of reducing the effect of orbital disturbance torques by maintaining the satellite's orientation around an equilibrium point. In contrast, active attitude control uses actuators to perform attitude manoeuvres using a source of energy. The actuators typically used for active attitude control are reaction wheels, momentum wheels (that also provide gyroscopic stiffness), control moment gyros, magnetic torquers, and thrusters.
It follows from what has just been said that when dealing with active satellite attitude control, it is necessary to specify the desired orientation, determine the current orientation of the satellite and then control the actuators so as to rotate the satellite in the desired orientation. In space engineering, it is customary to group these three tasks under the name of guidance, navigation and control (GNC) function. Specifically in the field of satellite attitude, the guidance function consists of determining the desired orientation of the spacecraft, and then providing the reference for the controller to follow. Instead, the navigation function refers to the determination, at a given time, of the orientation of the spacecraft. To perform this task, firstly the satellite is equipped with sensors capable of measuring the orientation of the satellite with respect to a reference, e.g. Sun sensors, Earth sensors, star sensors, magnetometers, and GPS antennas. Then, the navigation function consists of filters, such as the Kalman filter, that merge these measurements and produces estimates of the actual orientation of the satellite. Finally, the control function refers to the algorithms that, based on both the actual and desired orientation of the spacecraft, calculate the control torques required to orient the vehicle as desired. The control torques are then physically applied by the actuation system, which consists of the actuators seen above. The scheme in Figure 1.1 shows the typical architecture of the GNC, schematising the connections between the three functions encompassed by the GNC system and the links with the other satellite systems as described above. The plant, which has not yet been mentioned, includes the attitude dynamics and kinematics and orbital disturbances, and will be analysed in Chapter 2.
For the moment, the focus is on the GNC system, which deals with techniques for determining the orientation of a spacecraft and then controlling it so that the

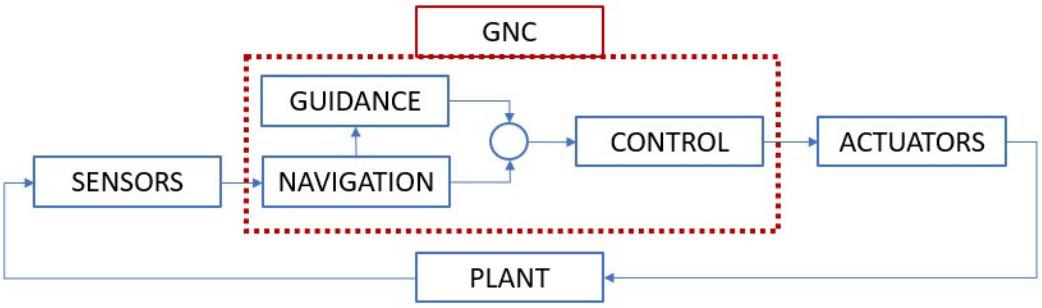

Fig. 1.1 General GNC system architecture

spacecraft points in some desired direction. Within the GNC system, the tasks of attitude determination and attitude control are obviously coupled from a practical point of view, but the pointing requirements for most space missions have been met by designing the attitude determination and control systems separately. This is also the approach taken in this thesis, where the attitude control system (ACS) is designed assuming that the orientation of the satellite is perfectly known, i.e. the navigation function is omitted. In this way, the ACS takes in input the error between the desired and actual orientation of the spacecraft and computes the control torque through the control algorithms. Even with this simplification, the design of the ACS encompasses several difficulties, including nonlinearity of the dynamic system, also characterised by parametric uncertainties and unmodelled dynamics, and limited actuation power. The importance of the application, coupled with the difficulties involved, have led the scientific community to investigate this field of research in depth, and countless publications appear in the literature to date. Among the first notable contributions is the article in reference [3], where the author provides a mathematical description of the attitude stabilisation problem and the necessary and sufficient conditions for the controllability of a rigid body in the case of one, two and three independent control torques. According to the results of this article, in [4] Lyapunov functions were used to prove that, whenever three independent torques are available, i.e. the spacecraft is *fully actuated*, the attitude can be fully controlled via a PD control law. Instead, in [5] the authors consider an *underactuated* spacecraft in which only two independent torques are available, concluding that in this case the problem of attitude regulation is not solvable by means of continuous (static or dynamic) time invariant control laws. Then, a time-varying control law achieving local asymptotic stability for underactuated spacecraft has been proposed in [6]. In the works just cited, the control laws use complete knowledge of the satellite's states,

i.e. angular positions and velocities. More complex is the attitude control problem for satellites where angular velocity is not measured. An original contribution for this case study is the article in reference [7], which propose a method based on passivity approach to replace the angular rate feedback control by a non-linear filter of the angular positions. The passivity theory is also used in [8], deriving an adaptive control scheme that achieves attitude tracking with global convergence. Another much studied issue is the design of closed-loop control algorithms for large-angle rotations. Two standard references for this issue are [9, 10], where control laws are formulated based on different attitude parameterization, and asymptotic stability is shown by using a Lyapunov function analysis. A further standard reference in spacecraft attitude control is the article [11], which is also very pertinent to the problem addressed in this PhD project. In fact, the authors of [11] consider the same attitude parameterisation used in this thesis, and study attitude stabilisation with large-angle manoeuvres, demonstrating that their control law stabilises the satellite regardless of the value of the system parameters. However, real actuators are not considered in [11], so the control torque does not suffer from saturation, as is the case in this thesis. More recently, several advanced control techniques have been proposed in the literature in preference to classical linear control methodologies, which do not appear suitable for attitude stabilization of modern satellites characterised by low-stiffness and reconfigurable structures. [12]
Satellite attitude control strategies in the literature include the state dependent Riccati equation (SDRE) techniques [13], whose main disadvantage is that it requires solving the Riccati equation repeatedly at each integration step. In order to mitigate the large computational effort, in [14] a neuro-fuzzy controller was developed by training a neuro-fuzzy network to approximate the SDRE controller. Other techniques investigated for satellite attitude control are nonlinear dynamic inversion (NDI)-based algorithms [15]. This type of approach usually cancels the system nonlinearity by transforming the original nonlinear dynamics into an entirely or partly linear version, thus enabling the use of conventional linear control techniques. One critical problem is that exact dynamic inversion may inherently suffer from lack of robustness due to to numerical errors, environmental uncertainties, external disturbances, and model simplifications [16]. Hence, researchers have devoted efforts to address this issue and enhanced versions, namely incremental NDI [17] and adaptive NDI [18] control, have been successfully proposed. Fractional-order control (FOC)-based strategies can be found in the literature to provide spacecraft attitude control. In [19], two

fractional-order proportional integral derivative methods are proposed to stabilise the rigid spacecraft rotational dynamics, while in [20, 21] the FOC is combined with sliding mode control to provide spacecraft attitude control. For these techniques, the selection of the fractional order is usually key, and it must be properly adjusted. A poor selection of this value can result in the degradation of the system stability as well as its robustness [16]. Backstepping-based techniques are also used for the design of spacecraft attitude control algorithms. In [22] an integrator backstepping algorithm based on quaternion feedback is used for attitude control of a micro satellite, while a backstepping attitude controller free of torque saturation is designed in [23]. According to [24], a drawback of backstepping-based control techniques is the sensitivity with respect to the numerical errors. Optimal control strategies are also investigated in the field of spacecraft attitude control: in [25] a H_∞ controller is used for attitude tracking control of a rigid spacecraft, in [26] a θ-D control technique is used for the capture and removal of large space targets, and in [27] a linear quadratic regulator (LQR)- based control is designed and tested in a six-degree-of-freedom spacecraft simulator testbed. These techniques require a cost function to be defined, which is crucial as the performance offered by the controller is only optimal with respect to the prescribed cost function. Furthermore, non-linear constraints, such as saturation, are generally not well managed.

Different from all these just described, but very interesting in this field of application, are the attitude control techniques based on variable structure control (VSC) with sliding mode. As a non-linear control technique, sliding mode control (SMC) is of particular interest as an algorithm for the ACS. Indeed, SMC has several appealing features, such as insensitivity to matched disturbances and uncertainties, ease of tuning and implementation, precision, and low computational effort. Owing to its characteristics, the application of sliding mode techniques for satellite attitude control has been studied in depth, and over the years the scientific community has conducted research to improve the performance provided by these techniques. A detailed literature review concerning the evolution of SMC techniques for satellite attitude dynamics is provided in Chapter 3, while here we limit to provide an overview of the research direction followed in this field in order to frame the motivations behind the work carried out in this project. Many of the works published in this field over the years address some of the native problems of SMC, which are therefore also critical in satellite attitude control applications. These include the high-frequency oscillations (chattering) in closed-loop dynamics, the speed of convergence of the

system towards equilibrium and the saturation of the actuators especially during the initial stages of the control process. In line with these issues, in this thesis we tackle chattering and actuator saturation in Chapter 3, and then also address SMC convergence speed in Chapter 4, combining adaptive control techniques with SMC algorithms. This combination has already been studied in the literature to adjust in real time some parameters of the SMC law to alleviate chattering, whereas in this work adaptive laws are used to to improve the robustness of the control system, the convergence speed of the algorithm and the tracking precision. The new control algorithm obtained by combining adaptive control and SMC is the main novelty of this thesis, and is applied for satellite attitude control. In particular, we address the problem of attitude stabilisation by including real effects such as flexibility of structures and saturation of actuators. To this end, the design of the control algorithms is based on a linearised model of attitude dynamics and proof of mathematical stability is provided through Lyapunov functions under the conditions in which this simplified system is valid. In addition, the control algorithms are tested through extensive numerical simulations using a simulator of a real satellite, namely the DEMETER, and an orbital simulator constructed in this thesis (details in Chapter 2), where the non-linear equations of attitude dynamics are implemented, including orbital disturbances, structure flexibility and actuator saturation. The results obtained are encouraging regarding the potential of the innovative adaptive SMC algorithm developed in this thesis, suggesting that the novel controller yields improved performance with respect to more standard SMC algorithm. On the one hand, numerical simulations show that, in the scenarios we examined, the adaptive SMC is more robust against unmodelled dynamics and parametric uncertainties, while increasing controller accuracy, convergence speed and reducing the risk of actuator saturation without chattering in closed-loop dynamics. On the other hand, from the mathematical analysis it can be inferred that that the adaptive SMC may improve the convergence speed and accuracy with respect to the original counterpart. In particular, these aspects are demonstrated under specific circumstances through Lyapunov functions. Finally, the rest of the thesis is divided into 5 chapters as follows. Chapter 2 first introduces the reference frames used to define the orientation of a satellite in space, and then describes the parameterisation employed to describe the satellite's attitude in a mathematical sense. Following this, equations are presented to describe the evolution of the attitude over time, entering into the attitude kinematics and dynamics. Regarding the dynamics in particular, first the satellite is analysed as

a rigid body, and then the equations are modified by introducing structure flexibility and parametric uncertainties. Finally, for both kinematics and dynamics, rigorous (non-linear) equations are provided, and then simplified, linear equations are derived that are more useful for controller design purposes.

Chapter 3 begins by introducing the origin and evolution of SMC, especially with regard to the techniques reported in the literature to alleviate chattering. The algorithms used in the continuation of the thesis are then formulated for a second-order system with only one input, providing the control laws and stability conditions. Afterwards, the control algorithms are used to manipulate the attitude dynamics of the satellites, comparing the results obtained with two different SMC algorithms with regard to chattering elimination, pointing accuracy and ease of tuning and implementation. Finally, the design of the SMC algorithms is conducted by including real-world issues such as actuator saturation, parametric uncertainties and unmodelled dynamics.

Chapter 4 is structured similarly to Chapter 3, but deals with SMC algorithms with time-varying sliding surface. The sliding surface is one of the characteristic components of SMC that heavily influences controller performance. Therefore, first a literature review on SMC algorithms with time-varying sliding surface is provided. After that, the logic of operation of the new adaptive SMC algorithm developed in this project is detailed and formulated for a second-order system with a single input, deriving mathematical proofs of stability and performance improvement over the classical SMC. Finally, the new algorithm is designed to be applied to both the mathematical models of attitude dynamics built in this thesis and the DEMETER satellite from CNES, in order to replicate the control law implemented on the real satellite.

The results of the numerical simulations performed in *Matlab/Simulink* environment are in Chapter 5. For each of the simulation scenarios described in Chapters 3 and 4, graphs of the most significant results obtained are presented, providing comments and highlighting salient aspects. Finally, the details of the flexible satellite attitude dynamics model are in Appendix A and Conclusions are drawn in Chapter 6.

Chapter 2

Mathematical models for spacecraft attitude analysis

This chapter first defines the attitude of the satellite, introducing the reference frames and parameters needed to describe it. Then, the evolution of the attitude over time is analysed, providing the equations necessary to describe this aspect mathematically. Then, we will see how the torques acting on the satellite modify its orientation, detailing the actuators and environmental disturbances from which these torques derive. In addition, the satellite's attitude dynamics will be analysed from both a rigid and flexible body perspective, with the latter detailing the methodology for modelling the satellite's flexible structures and the coupling between flexible and attitude dynamics. Finally, the equations are simplified with assumptions, reducing them to a useful form for controller design.
The main references for the attitude representations and attitude kinematics are [28–31], while for the attitude dynamics of the rigid body the main references are [28, 32–35]. Then, the references for the attitude dynamics of flexible spacecraft are provided in the corresponding section, whilst the orbital disturbances are well referred in [36, 37].

2.1 Attitude of a spacecraft

This section introduces the problem of determining the attitude of a spacecraft, i.e. determining its orientation in space. To this end, we first present the reference

systems often used in spacecraft attitude analysis. Then, some parameters allowing us to describe the attitude of the satellite are introduced. In particular, we will see how to use these parameters to quantify the rotation of the satellite with respect to a desired orientation, so as to derive the attitude error that the control system is required to correct.

2.1.1 Reference frames

The attitude of a satellite, as of any other vehicle, is normally described by the orientation of a frame attached to the satellite with respect to a second reference frame. Several reference systems are of particular interest for expressing the orientation of a satellite, but in this subsection we will only discuss those used in this thesis, while a more in-depth analysis can be found in references given above. In general, a reference frame is specified by the position of the origin and the orientation of the coordinate axes, with the latter being of particular interest for attitude analysis.

Body frame

The body frame is the system attached to the satellite. It is defined by an origin at a specific point on the body and by three Cartesian axes.The satellite inertia tensor is diagonal when referred to the central axes of inertia, thus simplifying the description of attitude dynamics. However, in real applications, there are stresses due to launch and thermal gradients in orbit or displacements of solar panels or antennas. Due to these phenomena, both the centre of mass and the main axes of inertia move in a manner that is difficult to characterise during the mission. For this reason, it is quite common to define the body coordinate system as the orientation of a sufficiently rigid navigation base, which is a subsystem of the spacecraft including the most critical attitude sensors and payload instruments. In this thesis, we partially include this aspect, as we are going to define a nominal inertia tensor with respect to the central axes, hence diagonal and with known and constant parameters. Next, uncertainties on the inertia matrix will be considered. A representation of a body frame $\mathfrak{F}_B$ with its origin at the centre of mass and Cartesian axes parallels to central axes of inertia is in Figure 2.1

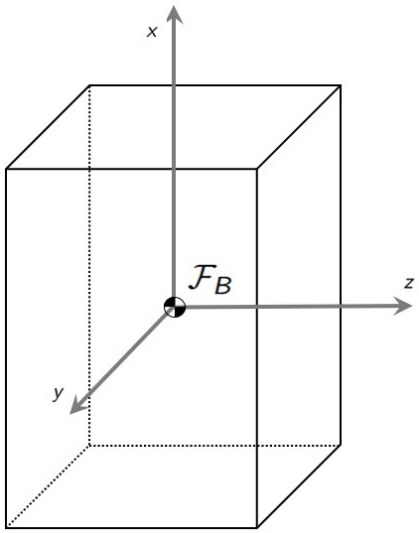

Fig. 2.1 The body frame $\mathfrak{F}_B$

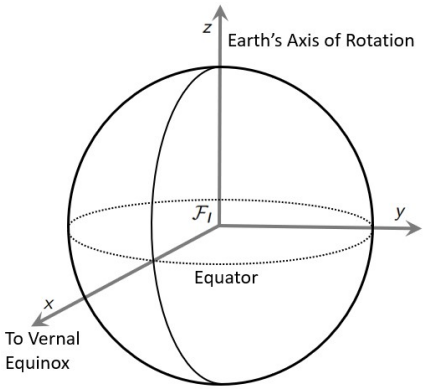

Fig. 2.2 The ECI frame $\mathfrak{F}_I$

The Earth-Centered Inertial (ECI) frame

The ECI frame $\mathfrak{F}_I$ is important in spacecraft attitude analysis because many satellites are inertial pointing spacecraft, i.e. their orientation with respect to the ECI frame has to be kept constant. This frame is defined with respect to the Earth's axis of rotation and the ecliptic plane, i.e. the plane of the Earth's orbit around the Sun. Then, the ECI frame is defined at one of the two point along the Earth's orbit where the equator plane and the ecliptic cross. Specifically, $\mathfrak{F}_I$ is centered in the Earth's center of the mass and is defined at the vernal equinox by taking the x_I axis in the direction from the Earth center to the vernal equinox, z_I is the Earth rotational axis and y_I follows the right hand rule. The frame is shown in Figure 2.2.

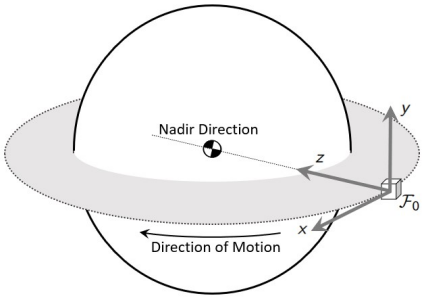

Fig. 2.3 The LVLH frame $\mathfrak{F}_0$

The Local Vertical Local Horizontal (LVLH) frame

The LVLH frame $\mathfrak{F}_0$ is another widely used frame in spacecraft attitude applications, especially for Earth-pointing spacecraft. Indeed, in this frame the z_0 axis points along the nadir vector, from the center of mass of the spacecraft (where is located the origin of $\mathfrak{F}_0$) toward the center of the Earth. Then, y_0 points along the direction opposite to the spacecraft's orbital angular velocity and z_0 follows the right hand rule. The $\mathfrak{F}_0$ frame is shown in Figure 2.3.

2.1.2 Attitude representations

It was mentioned at the beginning of the chapter that the study of the orientation of a satellite in space consists of defining the orientation of the body frame $\mathfrak{F}_B$ with respect to a second reference system, e.g. $\mathfrak{F}_I$ for inertial pointing satellite or $\mathfrak{F}_0$ for Earth pointing satellite. For this purpose, there are rotation matrices, or attitude matrices, so called because they specify the rotation that brings one reference frame to coincide with the other. They also allow the coordinates of a vector to be transformed from one reference frame to another. In 3-D space, a rotation matrix can be described by a minimum set of three parameters, for which many parametrizations could be used. In this thesis, only Euler angles and quaternions are described, which are used in the following to describe the attitude of the satellites. Other choices can be found in the references indicated at the beginning of the Chapter.

Euler Angles

This is a very common set of parameters to express the orientation between two reference frames. This representation expresses a rotation from an initial frame $\mathfrak{F}_1$ defined by the orthormal set of unit vectors $\mathfrak{F}_{1,i}$ $(i = x, y, z)$ as follows:

$$\mathfrak{F}_{1,x} = \begin{bmatrix} 1 \\ 0 \\ 0 \end{bmatrix}, \quad \mathfrak{F}_{1,y} = \begin{bmatrix} 0 \\ 1 \\ 0 \end{bmatrix}, \quad \mathfrak{F}_{1,z} = \begin{bmatrix} 0 \\ 0 \\ 1 \end{bmatrix},$$

to a final frame $\mathfrak{F}_2$ defined by the orthormal set of unit vectors $\mathfrak{F}_{2,i}$ $(i = x, y, z)$ like the above, as the product of three rotations: a first rotation from $\mathfrak{F}_1$ to an intermediate frame $\mathfrak{F}_{1_a}$, then to a second intermediate frame $\mathfrak{F}_{1_b}$, and finally to frame $\mathfrak{F}_2$. More precisely, those just mentioned are *principal rotations*, as they occur around a coordinated axis of the reference frame. For the result to be valid, two successive rotations cannot occur around the same axis, and a different set of Euler angles is obtained based on the order in which the three rotations take place. A complete description of all the possible sequences can be found in the references given in the beginning of this Chapter, here we confine ourselves to describing the 1-2-3 rotation sequence (Figure 2.4 taken from [38]), which is widely used in aerospace applications. The 1-2-3 rotation which brings $\mathfrak{F}_1$ to coincide with $\mathfrak{F}_2$ is as follows:

1) a first rotation about the x-axis of $\mathfrak{F}_1$, named *roll* angle ϕ , which brings the y, z axes of $\mathfrak{F}_1$ to coincide with the y, z axes of $\mathfrak{F}_{1_a}$. This is described by the rotation matrix $A(\phi)$:

$$A(\phi) = \begin{bmatrix} 1 & 0 & 0 \\ 0 & c_\phi & -s_\phi \\ 0 & s_\phi & c_\phi \end{bmatrix}, \tag{2.1}$$

where $s_\alpha = sin(\alpha)$ and $c_\alpha = cos(\alpha)$ as a general rule for the following,

2) a second rotation about the y-axis of $\mathfrak{F}_{1_a}$, named *pitch* angle θ, which brings the x, z axes of $\mathfrak{F}_{1_a}$ to coincide with the x, z axes of $\mathfrak{F}_{1_b}$. This is described by the rotation matrix $A(\theta)$:

$$A(\theta) = \begin{bmatrix} c_\theta & 0 & s_\theta \\ 0 & 1 & 0 \\ -s_\theta & 0 & c_\theta \end{bmatrix}, \tag{2.2}$$

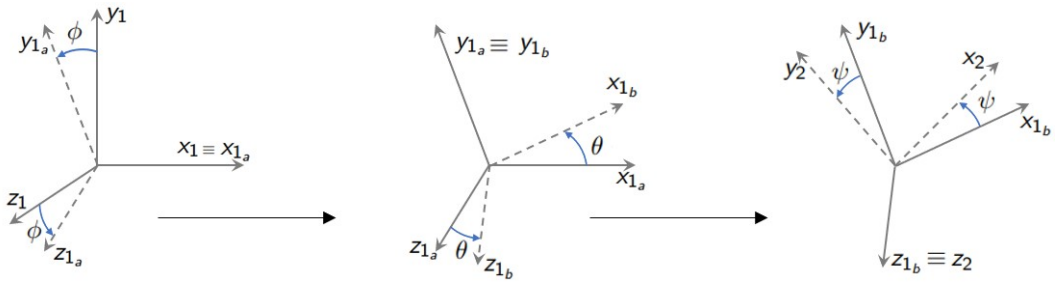

Fig. 2.4 Euler rotation sequence 1-2-3

3) a third rotation about the z-axis of $\mathfrak{F}_{1_b}$, named *yaw* angle ψ, which brings the x, y axes of $\mathfrak{F}_{1_b}$ to coincide with the x, y axes of $\mathfrak{F}_2$.

$$A(\psi) = \begin{bmatrix} c_\psi & -s_\psi & 0 \\ s_\psi & c_\psi & 0 \\ 0 & 0 & 1 \end{bmatrix}. \tag{2.3}$$

Recalling that products of rotation matrices are also rotation matrices, and successive rotations can be combined by multiplying the rotation matrices in the reverse order of the rotations, the rotation matrix from frame $\mathfrak{F}_1$ to frame $\mathfrak{F}_2$ with the sequence above is given by

$$A_{21}(\phi,\theta,\psi) = A(\psi)A(\theta)A(\phi) = \begin{bmatrix} c_\theta c_\psi & c_\phi s_\psi + s_\phi s_\theta c_\psi & s_\phi s_\psi - c\phi s_\theta c_\psi \\ -c_\theta s_\psi & c_\phi c_\psi - s_\phi s_\theta s_\psi & s_\phi c_\psi + c\phi s_\theta s_\psi \\ s_\theta & -s_\phi c_\theta & c_\phi c_\theta \end{bmatrix}, \tag{2.4}$$

which is fully parameterised by $\Theta = (\phi, \theta, \psi)$, thereby describing the orientation of $\mathfrak{F}_1$ with respect to $\mathfrak{F}_2$. Therefore, given a general vector $\mathbf{v}$ expressed as

$$\mathbf{v}_1 = v_{1_x}\mathfrak{F}_{1,x} + v_{1_y}\mathfrak{F}_{1,y} + v_{1_z}\mathfrak{F}_{1,z}$$

in frame $\mathfrak{F}_1$, it can be expressed in frame $\mathfrak{F}_2$ as follows:

$$\mathbf{v}_2 = A_{21}(\phi,\theta,\psi)\mathbf{v}_1 = v_{2_x}\mathfrak{F}_{2,x} + v_{2_y}\mathfrak{F}_{2,y} + v_{2_z}\mathfrak{F}_{2,z}, \tag{2.5}$$

and for the properties of the rotation matrices, we also have that

$$\mathbf{v}_1 = A_{21}^T(\phi,\theta,\psi)\mathbf{v}_2, \tag{2.6}$$

Quaternions

The Euler angles seen in the previous subsection have the advantage of presenting the orientation of a body with high intuitiveness, however they suffer from the problem of singularities. The singularity may occur for any three-dimensional parameterization of the rotation matrix. For the 1-2-3 sequence above, the singularity occurs for $\theta = \pm\pi/2$. In this case, ϕ and ψ are associated with the same rotation, and cannot be determined uniquely. By adding a redundant parameter to the set describing the rotation matrix, quaternions successfully solve this problem. To understand how quaternions can define a rotation, it is useful to recall the Euler's Theorem, which states that two generic reference frames can be brought to coincide with each other by a single rotation α around the same axis defined by the unit vector e_α. Then, this rotation can be described by the quaternions, which consists of a *scalar part* q_0 and a *vectorial part* q_v as follows:

$$q = \left[\underbrace{\cos\left(\frac{\alpha}{2}\right)}_{q_0},\ \underbrace{e_\alpha^T \sin\left(\frac{\alpha}{2}\right)}_{q_v^T}\right]^T = [q_0,\ q_{v_1},\ q_{v_2},\ q_{v_3}]^T . \tag{2.7}$$

Now, if e_α and α are such that they describe the same rotation (2.1)-(2.3), then the quaternions (2.7) describe the same rotation as the Euler angles $\Theta = (\phi, \theta, \psi)$ in (2.1)-(2.3). Quaternions used to parameterize rotations have unit norm, thus, the inverse of the quaternion is identical with its conjugate. Besides avoiding singularity problems, the use of quaternions has the advantage of high computational efficiency as they are purely algebraic and do not use trigonometric functions. The rotation matrix (2.4) describing the orientation between $\mathfrak{F}_1$ and $\mathfrak{F}_2$ can also be given in quaternion form as follows:

$$\begin{aligned} A_{21}(q) =& (q_0^2 - q_v^T q_v)\mathbf{I}_3 + 2q_v q_v^T - 2q_0 q_v^\times = \\ =& \begin{bmatrix} q_{v_1}^2 - q_{v_2}^2 - q_{v_3}^2 + q_4^2 & 2(q_{v_1}q_{v_2} + q_{v_3}q_4) & 2(q_{v_1}q_{v_3} - q_{v_2}q_4) \\ 2(q_{v_2}q_{v_1} - q_{v_3}q_4) & -q_{v_1}^2 + q_{v_2}^2 - q_{v_3}^2 + q_4^2 & 2(q_{v_2}q_{v_3} + q_{v_1}q_4) \\ 2(q_{v_3}q_{v_1} + q_{v_2}q_4) & 2(q_{v_3}q_{v_2} - q_{v_1}q_4) & -q_{v_1}^2 - q_{v_2}^2 + q_{v_3}^2 + q_4^2 \end{bmatrix}, \end{aligned} \tag{2.8}$$

being $\mathbf{I}_3$ the 3 by 3 identity matrix and $q_v^\times$ the skew symmetric matrix with the components of q_v as follows:

$$q_v^\times = \begin{bmatrix} 0 & -q_{v_3} & q_{v_2} \\ q_{v_3} & 0 & q_{v_1} \\ -q_{v_2} & -q_{v_1} & 0 \end{bmatrix}. \tag{2.9}$$

Therefore, as in (2.5) the vector $\mathbf{v}_1$ can be expressed in the frame $\mathfrak{F}_2$ through

$$\mathbf{v}_2 = A_{21}(q)\mathbf{v}_1, \tag{2.10}$$

with the transpose of $A_{21}(q)$ giving the inverse transformation as in (2.6).

Conversion

In the previous, the characteristics of both Euler angles and quaternions were presented. It is certainly useful to provide the transformation equations between the two representations of the attitude. The equation for the conversion depends on the order of rotation, in particular the Euler angles for a 1-2-3 rotation can be obtained from the quaternions as follows:

$$\begin{bmatrix} \phi \\ \theta \\ \psi \end{bmatrix} = \begin{bmatrix} \arctan\left(\frac{2(q_0 q_{v_1} + q_{v_2} q_{v_3})}{1-2(q_{v_1}^2 + q_{v_2}^2)}\right) \\ \arcsin\left(2(q_0 q_{v_2} - q_{v_3} q_{v_1})\right) \\ \arctan\left(\frac{2(q_0 q_{v_3} + q_{v_1} q_{v_2})}{1-2(q_{v_2}^2 + q_{v_3}^2)}\right) \end{bmatrix} \tag{2.11}$$

On the other side, it is also possible to obtain quaternions from the Euler angles. The equation allowing this conversion is as follows:

$$q = \begin{bmatrix} c_{\phi_2} c_{\theta_2} c_{\psi_2} + s_{\phi_2} s_{\theta_2} s_{\psi_2} \\ s_{\phi_2} c_{\theta_2} c_{\psi_2} - c_{\phi_2} s_{\theta_2} s_{\psi_2} \\ c_{\phi_2} s_{\theta_2} c_{\psi_2} + s_{\phi_2} c_{\theta_2} s_{\psi_2} \\ c_{\phi_2} c_{\theta_2} s_{\psi_2} - s_{\phi_2} s_{\theta_2} c_{\psi_2} \end{bmatrix} \tag{2.12}$$

where $s_{\alpha_2} = \sin(\alpha/2)$ and $c_{\alpha_2} = \cos(\alpha/2)$.

Attitude errors

As previously said, with "attitude of a spacecraft" we refer to the orientation of the spacecraft with respect to a reference frame. In particular, we address attitude error when the orientation of the satellite is referred to the *objective* reference frame, i.e. the reference frame that gives the desired orientation of the satellite during the mission. To express this concept more clearly, let us take the body frame $\mathfrak{F}_B$, the ECI frame $\mathfrak{F}_I$ in subsection 2.1.1, and the objective $\mathfrak{F}_D$. With these three reference frames, we can compute the attitude error as follows:

i) The orientation of $\mathfrak{F}_B$ relative to $\mathfrak{F}_I$ is given by the on-board sensors as $\Theta_B = (\phi, \theta, \psi)_B$, or q_B in terms of quaternions.

ii) The orientation of $\mathfrak{F}_D$ relative to $\mathfrak{F}_I$ is $\Theta_D = (\phi, \theta, \psi)_D$, or q_D in terms of quaternions.

iii) Following the two points above, $\mathfrak{F}_B$ can be brought to coincide with $\mathfrak{F}_D$ through two steps: a first rotation $\Theta_B = (\phi, \theta, \psi)_B$, which brings $\mathfrak{F}_B$ to coincide with $\mathfrak{F}_I$, and a second rotation $-\Theta_D = -(\phi, \theta, \psi)_D$, which brings $\mathfrak{F}_I$ to coincide with $\mathfrak{F}_D$. Therefore, the attitude error $\Theta_e = (\phi, \theta, \psi)_e$, i.e. the orientation of $\mathfrak{F}_B$ relative to $\mathfrak{F}_D$ is given by

$$\Theta_e = \Theta_B - \Theta_D, \tag{2.13}$$

or, in terms of quaternions:

$$q_e = q_D^* \otimes q_B \tag{2.14}$$

where q_D^* is the conjugate of q_D. It is worth specifying that (2.13) and (2.14) represent two different rotations, so Θ_e in (2.13) and q_e in (2.14) are not linked by (2.11) nor (2.12). However, one can calculate the attitude error q_e in quaternions with (2.14), and then obtain the representation in Euler angles of the same rotation by applying (2.11) to q_e.

Expressing the attitude error in this way is also more faithful to real applications, because on-board sensors allow the satellite's attitude to be measured with respect to a reference frame that, in general, is different from the target frame. As an example, star trackers allow the satellite's attitude to be measured with respect to an inertial reference frame, which is however oriented differently from the ECI frame.

2.2 Attitude kinematics and dynamics

This section investigates the kinematics of rotations, or attitude kinematics, by deriving the equations for the time derivatives of Euler angles and quaternions. Therefore, these equations will describe the time evolution of the satellite attitude. The kinematics of attitude covers those aspects of rotational motion that can be analysed without considering torques. When torques are introduced, one enters the field of dynamics. The discussion of dynamics begins by considering the fundamental role played by the satellite's angular momentum. We then analyse the dynamics under the assumption of a rigid satellite, and then introduce the flexibility of the structures. Here, the coupling between attitude dynamics and flexible dynamics will be analysed, specifying their mutual interaction. Finally, a description is given of the orbital perturbations that enter into attitude dynamics.

2.2.1 Attitude kinematics

Having examined how to describe the attitude of a body in space, i.e. the relative orientation between reference frames, let us now look at how its evolution in time can be described. To this end, this subsection presents the time derivatives of Euler angles and quaternions. For the purposes of this discussion, let us again consider the previously used frames $\mathfrak{F}_B$ (body frame), $\mathfrak{F}_D$ (objective frame), $\mathfrak{F}_I$ (ECI frame). Now, we define ω_e as the angular rate of $\mathfrak{F}_B$ with respect to $\mathfrak{F}_D$, given in $\mathfrak{F}_B$ coordinates. To this end, take ω_B as the angular rate of $\mathfrak{F}_B$ relative to $\mathfrak{F}_I$ given in $\mathfrak{F}_B$ coordinates and ω_D as the angular rate of $\mathfrak{F}_D$ relative to $\mathfrak{F}_I$ given in $\mathfrak{F}_D$ coordinates. For the rule of compositions of angular velocities, i.e. they are additive, ω_e is obtained as

$$\omega_e = \omega_B - A_{21}^T(\Theta_e)\omega_D, \quad \text{or} \quad \omega_e = \omega_B - A_{21}^T(q_e)\omega_D, \tag{2.15}$$

where $A_{21}^T(\Theta_e)$ ($A_{21}^T(q_e)$) is the transpose of the attitude matrix in (2.4) (in (2.8)), whose components are obtained putting there the Euler angles in (2.13) (the quaternions in (2.14)), giving the orientation of $\mathfrak{F}_B$ relative to $\mathfrak{F}_D$.

Attitude kinematics in terms of Euler angles

Using ω_e as in (2.15), the time evolution of the attitude error in terms of Euler angles (2.13) for a 1-2-3 rotation is as follows:

$$\dot{\Theta}_e = \begin{bmatrix} \dot{\phi}_e \\ \dot{\theta}_e \\ \dot{\psi}_e \end{bmatrix} = \underbrace{\frac{1}{c_\theta} \begin{bmatrix} c_{\psi_e} & -s_{\psi_e} & 0 \\ c_{\theta_e} s_{\psi_e} & c_{\theta_e} c_{\psi_e} & 0 \\ -s_{\theta_e} c_{\psi_e} & s_{\theta_e} s_{\psi_e} & c_{\theta_e} \end{bmatrix}}_{B(\Theta_e)} \omega_e = B(\Theta_e)\omega_e. \tag{2.16}$$

The kinematics in (2.16) is non-linear and the three components are coupled together. However, it is well known that for small attitude errors, i.e. $\Theta_e \approx 0$, we have $B(\Theta_e) \simeq \mathbf{I}_3$. Therefore, in this situation we can consider a linearised, decoupled kinematics given by

$$\dot{\Theta}_{e_i} = \omega_{e_i}, \quad i = x, y, z. \tag{2.17}$$

Attitude kinematics in terms of quaternions

Using ω_e as in (2.15), the time evolution of the attitude error in terms of quaternions (2.14) for a 1-2-3 rotation is as follows:

$$\dot{q}_e = \frac{1}{2} \left(q_{e_0} I_4 + \begin{bmatrix} 0 & q_{e_v}^T \\ q_{e_v} & q_{e_v}^\times \end{bmatrix} \right) \begin{bmatrix} 0 \\ \omega_{e_1} \\ \omega_{e_2} \\ \omega_{e_3} \end{bmatrix} \tag{2.18}$$

Also in this case, the kinematics (2.18) is non linear and the four components are coupled together. However, for small attitude error, i.e. $q_e \approx (1,0,0,0)^T$, (2.18) reduce to the following equation, which is linear and decoupled in the three axis:

$$\dot{q}_{e_i} = \frac{1}{2} \omega_{e_i}, \quad i = x, y, z. \tag{2.19}$$

Notes

As seen above, attitude kinematics is described by (2.16), which in turn involves Eqs. (2.13) and (2.15) focusing on the description using Euler angles. In the specific

case where the attitude mission requires inertial pointing with $\mathfrak{F}_B$ aligned to $\mathfrak{F}_I$, eqs. (2.13), (2.15), and (2.16) becomes as follows:

$$\Theta_e = \Theta_B, \tag{2.20}$$

i.e. the attitude error is given by the orientation of the frame $\mathfrak{F}_B$ with respect to the frame $\mathfrak{F}_I$,

$$\omega_e = \omega_B, \tag{2.21}$$

i.e. the angular rate error is given by the angular rate of the frame $\mathfrak{F}_B$ with respect to the frame $\mathfrak{F}_I$,

$$\dot{\Theta}_e = \dot{\Theta}_1 = B(\Phi_1)\omega_1, \tag{2.22}$$

which becomes as follows in its linearized form:

$$\dot{\Theta}_{e_i} = \dot{\Theta}_{B_i} = \omega_{B_i}, \quad i = x, y, z, \tag{2.23}$$

meaning that the time evolution of the attitude errors depends only on the orientation and the angular rates of the frame $\mathfrak{F}_1$. Similarly, if we consider the description of the attitude by quaternions in the same mission, eqs. (2.14), (2.15), (2.18), and (2.19) give:

$$q_e = q_B \tag{2.24}$$

$$\omega_e = \omega_B \tag{2.25}$$

$$\dot{q}_e = \dot{q}_B = \frac{1}{2}\left(q_{B_0} I_4 + \begin{bmatrix} 0 & q_{B_v}^T \\ q_{B_v} & q_{B_v}^{\times} \end{bmatrix}\right) \begin{bmatrix} 0 \\ \omega_{B_x} \\ \omega_{B_y} \\ \omega_{B_z} \end{bmatrix} \tag{2.26}$$

$$\dot{q}_{e_i} = \dot{q}_{B_i} = \frac{1}{2}\omega_{B_i}, \quad i = x, y, z. \tag{2.27}$$

2.2.2 Attitude dynamics of the rigid spacecraft

This section presents the rotational dynamics of the rigid spacecraft, thus deriving mathematical relations between the time evolution of the angular rate of the satellite and the internal/external torques acting on the satellite itself. When studying the attitude dynamics, the angular momentum of the spacecraft plays a fundamental role, therefore we first introduce this entity and its properties. Then, we analyze the attitude dynamics of the rigid spacecraft, referring the discussion to the body frame with its origin in the centre of the mass of the spacecraft and aligned with the central axes of inertia. Since the control laws developed in this thesis are designed to be implemented by RWs, this subsection specifically details the attitude dynamics equations for spacecraft equipped with this type of actuators. Next, the problem of saturations in reaction wheels is considered, analysing the conditions when this occurs. Finally, under certain assumptions that will be specified, simplified models of the attitude dynamics are derived to be used for the control algorithms design.

The angular momentum

In order to present the angular momentum of a rigid spacecraft, take again the body reference frame $\mathfrak{F}_B$, centred in the centre of mass and with the axes aligned with the central axes of inertia. Then, the angular momentum $H \in \mathbb{R}^3$ of this spacecraft in $\mathfrak{F}_B$ coordinates is as follows:

$$H = [J]_B \omega_B \tag{2.28}$$

where $\omega_B \in \mathbb{R}^3$ is as defined above, i.e. is the angular rate of the frame $\mathfrak{F}_B$ relative to the inertial and $[J]_B \in \mathbb{R}^{3,3}$ is the inertia tensor of the spacecraft expressed in $\mathfrak{F}_B$. In the following we refer to ω_B as ω and to $[J]_B$ as J for easy of notation, giving

$$[J]_B = J = \begin{bmatrix} J_{xx} & 0 & 0 \\ 0 & J_{yy} & 0 \\ 0 & 0 & J_{zz} \end{bmatrix}. \tag{2.29}$$

Often, spacecraft are equipped with reaction wheels (RWs) as actuators to provide the torques guaranteeing attitude control. RWs consist of a flywheel connected to an electric motor, which changes the flywheel's rotational speed by applying some torque around its axis of rotation, causing the spacecraft to start counter-rotating proportionally through conservation of angular momentum. Therefore, a reaction

wheel spins around its rotational axes, storing angular momentum to control the orientation of the spacecraft. In this case, the overall angular momentum of a rigid spacecraft fitted with RWs can be expressed as the sum of the angular momentum of the spacecraft body (2.28) together with the angular momentum of the wheels relative to the body $h_{\text{rw}} \in \mathbb{R}^3$:

$$H = J\omega + h_{\text{rw}}. \tag{2.30}$$

Due to the fact that a reaction wheel spins around its axis of symmetry, the components of h_{rw} are along the same direction, and must be expressed in $\mathfrak{F}_B$ frame to compute (2.30). When designing the attitude control algorithms in the following sections, we will assume the satellite is equipped with three RWs, arranged in a cluster whose centre of mass coincides with that of the satellite and in which each wheel has its axis of rotation aligned with a central axis of inertia. Therefore, let us specify (2.30) for this case:

$$H_i = J_{ii}\omega_i + h_{\text{rw}_i}, \quad i = x, y, z. \tag{2.31}$$

Equations above reveal that the angular momentum can be used to develop equations in ω that describe the attitude and rotational motion of the spacecraft. Indeed, for the conservation of angular momentum of isolated systems (such as spacecraft) we have:

$$\dot{H}\big|_B = m - \omega \times H, \tag{2.32}$$

where $\dot{H}\big|_B \in \mathbb{R}^3$ is the time derivative of H in the body frame $\mathfrak{F}_B$ which is rotating with angular speed ω with respect to the inertial and $m \in \mathbb{R}^3$ is the external torque acting on the system. Below, we further investigate (2.32), deriving the equations to describe the rotational dynamics of the spacecraft.

Attitude dynamics

Here, we investigate the attitude dynamics of a rigid spacecraft, thus characterized by $J = const$. The attitude dynamics of a rigid spacecraft can be described by the Euler's equation for the rotational dynamics, whose form depends on whether or not RWs (or other devices capable of storing angular momentum relative to the satellite body) are installed on board the satellite.

If the satellite has no such devices, the total angular momentum H is as in (2.28), and the left side of (2.32) yields:

$$\dot{H}\big|_B = J\dot{\omega}, \tag{2.33}$$

allowing us to obtain the Euler's equation for the rotational dynamics of rigid bodies as follows:

$$J\dot{\omega} = m - \omega \times J\omega. \tag{2.34}$$

As mentioned above, m is the external torque acting on the spacecraft, consisting of both orbital disturbances $d \in \mathbb{R}^3$ (see Subsection 2.2.4) and, if actuators are installed, control torques $u \in \mathbb{R}^3$, thus

$$m = d + u. \tag{2.35}$$

The actuators for attitude control providing an external torque u are named *reaction-types* actuators (thrusters, magnetorquers) and are able to manipulate the attitude of the spacecraft by changing the overall angular momentum of the system.
On the other side, if the spacecraft is equipped with RWs, the total angular momentum H is as in (2.30), and the left side of (2.32) yields:

$$\dot{H}\big|_B = J\dot{\omega} + \dot{h}_{\text{rw}}, \tag{2.36}$$

allowing us to obtain the Euler's equation for the rotational dynamics of spacecraft equipped with RWs as follows:

$$J\dot{\omega} = m - \omega \times (J\omega + h_{\text{rw}}) - \dot{h}_{\text{rw}}, \tag{2.37}$$

where $\dot{h}_{\text{rw}} \in \mathbb{R}^3$ is linked to the torque $\tau \in \mathbb{R}^3$ applied by the electric motor to which the wheel is attached as follows:

$$\dot{h}_{\text{rw}} = \tau. \tag{2.38}$$

By introducing (2.38) into (2.37), we can see that τ is effectively a control torque allowing to manipulate the orientation of the spacecraft. Furthermore, τ is a torque internal to the system, so it cannot vary the overall angular momentum H.

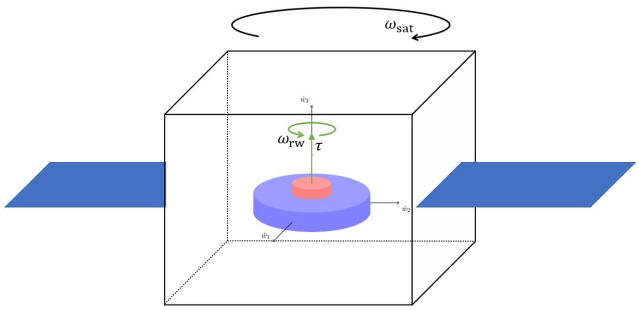

Fig. 2.5 A reaction wheel maneuvering a spacecraft. The reaction wheel consists of the electric motor (red) and the wheel (purple).

Reaction wheels

In contrast to reaction-type actuators, reaction wheels manipulate the satellite attitude by distributing angular momentum between the wheels and the satellite body. To better illustrate this point, take a spacecraft without reaction type actuators ($u = 0$) and free from orbital perturbation ($d = 0$), thus to obtain $m = 0$ in (2.37) and $H = const.$ due to the non-existence of external torques acting on the system. Furthermore, let us assume that the initial condition of the system are such that $\omega(0) = 0$ and $h_{\text{rw}}(0) = 0$, thus to obtain $H(t) = 0\ \forall t$. Due to (2.30), under these assumptions the following

$$J\omega(t) = -h_{\text{rw}}(t)\ \forall t \tag{2.39}$$

holds, meaning that if an electric motor is activated, thus to put into rotation the wheel to which it is attached, then the spacecraft body begin to counter-rotate proportionately through conservation of angular momentum. This is most clearly illustrated in Figure 2.5.

RWs are widely used as actuators to provide spacecraft attitude control, since a minimum set of three wheels can provide a 3-axis active control with high pointing accuracy without using a consumable propellant. Despite the great benefits that reaction wheels present, there are some issues on the performance that these actuators can develop. Firstly, there are structural constraints on the maximum rotational speed of the wheel, i.e. there is a maximum angular momentum $\overline{h_{\text{rw}}} \in \mathbb{R}$ that can be stored into the wheel. The second issue with RWs concerns the torque exchanged between the wheels and the spacecraft. In fact, the torque developed by the electric motor is closely related to the electrical power required to drive it, leading to a saturation value $\overline{\tau}$ on the maximum torque supplied. Following this discussion, and recalling

the assumption that the satellite has three RWs aligned with the central axes of inertia, it is concluded that the control law must ensure that the following conditions are met in order to avoid actuator saturation:

$$\tau_i \in [-\overline{\tau}, \overline{\tau}] \quad h_{\mathrm{rw}_i} \in [-\overline{h_{\mathrm{rw}}}, \overline{h_{\mathrm{rw}}}], \quad i = x, y, z. \tag{2.40}$$

According to (2.39) and (2.40), manoeuvres performed at high speeds can lead to saturation of the actuator, i.e. it can no longer store any angular momentum. If the initial conditions are $\omega(0) = \mathbf{0}_3$, $h_{\mathrm{rw}}(0) = \mathbf{0}_3$, $\mathbf{0}_3 = [0,\ 0,\ 0]^T$, and the satellite is free from external perturbations, we obtain from (2.39) that the angular rate must met the following condition to prevent angular momentum from saturation:

$$-\overline{h_{\mathrm{rw}}} \leq (J\omega)_i \leq \overline{h_{\mathrm{rw}}} \quad \Rightarrow \quad -(J^{-1}(\overline{h_{\mathrm{rw}}}\mathbf{1}_3))_i = -\overline{\omega}_i \leq \omega_i \leq \overline{\omega}_i = (J^{-1}(\overline{h_{\mathrm{rw}}}\mathbf{1}_3))_i \tag{2.41}$$

with $i = x, y, z$, $\mathbf{1}_3 = [1,\ 1,\ 1]^T$, and $\overline{\omega} \in \mathbb{R}^3$ the vectors with components the maximum permissible angular rate for each axis to prevent reaction wheels from saturation. Then, 2.41 becomes as follows if (2.31) holds:

$$|\omega_i| \leq \overline{\omega}_i = \frac{\overline{h_{\mathrm{rw}}}}{J_{ii}}. \tag{2.42}$$

If a wheel is saturated, it can no longer accumulate angular momentum, losing controllability of the satellite. In real applications, RWs store angular momentum not only to manoeuvre the satellite, but also to maintain its attitude despite external disturbances. To this end, RWs absorb the surplus of angular momentum injected into the system by the external non-conservative torque. This quantity of angular momentum is given by $\int_0^t d\ dt$, and spacecraft must be equipped with reaction-types actuators to discharge it.

Simplified model for attitude dynamics

Now, starting from the general equation of dynamics (2.37), we list below a number of assumptions (some of which have already been specified) that allow us to derive a simplified equation of dynamics that will be useful for synthesising the control algorithms in the sequel.

(i) the spacecraft body frame $\mathfrak{F}_1$ is aligned with the three central axis of inertia;

(ii) the actuation systems consists of three RWs arranged in a cluster whose center of mass coincides with the one of the spacecraft and the rotation axis of each wheel is aligned with a central axis of the spacecraft;

(iii) the spacecraft is spinning at low angular rates.

From the assumption (i) it follows that the inertia tensor J referred to $\mathfrak{F}_1$ is diagonal as in (2.29). Therefore, in the rotational dynamics (2.37) each degree of freedom (DOF) has a dedicated control channel. In addition, each wheel provides a control input that manipulates a single rotational DOF for the assumption (ii). Therefore, assumptions (i) and (ii) allows to decouple the three components of (2.37), thus enabling the control law to be derived separately for each rotational DOF. Also, from assumption (ii) we have $u = 0$ (no reaction-type actuators), obtaining $m = d$, i.e. the only external torques acting on the satellite are the orbital perturbations. Finally, assumption (iii) gives $\omega \approx \mathbf{0}_3$, allowing to neglect the cross product in (2.37). Following this discussion, the above assumptions together with (2.37) and (2.38) result in the following simplified dynamics equation

$$J_{ii}\dot{\omega}_i = d_i - \tau_i, \quad i = x, y, z, \tag{2.43}$$

where x, y, z are the coordinate axis of $\mathfrak{F}_B$ body reference frame.

Attitude dynamics error

Having reached this point, it is worth remembering that (2.37) (or (2.43) in its simplified form) describes the attitude dynamics of the $\mathfrak{F}_B$ body frame with respect to the inertial. However, when formulating control algorithms, the attitude dynamics error becomes of interest, and equations (2.37) (or (2.43)) gives the error only for an inertial pointing mission, i.e. for a mission where (2.21) holds. In a more general case, the attitude dynamics error $\dot{\omega}_e$ is obtained from (2.15) and the as

$$\dot{\omega}_e = \dot{\omega}_B - \dot{A}_{21}\omega_D - A_{21}\dot{\omega}_D, \tag{2.44}$$

where, $\dot{\omega}_B$ is in (2.37) (or (2.43) in its simplified form), while $\dot{A}_{21}$ is obtained from the rule of derivation of transformations matrix as

$$\dot{A}_{21} = -\omega_e \times A_{21} \quad \Rightarrow \quad \dot{A}_{21}\omega_D = \omega_e \times (A_{21}\omega_D), \tag{2.45}$$

being ω_e the angular rate of $\mathfrak{F}_B$ relative to $\mathfrak{F}_D$ as defined in (2.15). Finally, $\dot{\omega}_D$ is the time derivative of ω_D in $\mathfrak{F}_D$. Inserting (2.15), (2.44), and (2.45) into (2.37) we obtain the attitude dynamics error equation as:

$$J\dot{\omega}_e = -J(\omega_e \times (A_{21}\omega_D + A_{21}\dot{\omega}_D) + m - (\omega_e + A_{21}\omega_D) \times (J(\omega_e + A_{21}\omega_D) + h_{\text{rw}}) - \dot{h}_{\text{rw}}. \tag{2.46}$$

With the assumption (i)-(iii) and neglecting the usually very small gyroscopic and $\dot{\omega}_D$ terms for satellites actuated by reaction wheels, eq. (2.46) can be written in a simplified form as follows:

$$J_{ii}\dot{\omega}_{e_i} = d_i - \tau_i, \quad i = x, y, z. \tag{2.47}$$

It can be seen that, with these simplifications, eq. (2.47) is equal to equation (2.43). This is because by neglecting the gyroscopic terms and $\dot{\omega}_D$ in (2.46), one is actually neglecting the dynamics of $\mathfrak{F}_D$, i.e. the dynamics of the objective frame. As mentioned above, this approximation becomes acceptable for satellites actuated by RWs, because the manoeuvres that can be realised with these actuators are usually quite slow.

2.2.3 Attitude dynamics of the flexible spacecraft

This subsection first shows how to modify the equations obtained in the previous subsection when the inertia matrix J is affected by uncertainties. This is a very common case in real-world applications, either because of the stresses due to launch and thermal gradients in orbit, or because of the ability of some satellites to be reconfigured (displacement of solar panels or antennas). Next, we introduce the flexibility of structures in satellite attitude dynamics, specifying how the latter is coupled with flexible dynamics.

Dynamics equation for spacecraft with uncertain inertia

For this discussion, let us assume that the inertia matrix J is given by the sum of a known and constant term $J_0 \in \mathbb{R}^{3\times3}$, namely the nominal inertia, and an unknown term $\Delta J \in \mathbb{R}^{3\times3}$ enclosing the uncertainties due to the reconfigurability of the system and the characterisation errors of this parameter of the satellite. Thus, J is written as

follows:

$$J = J_0 + \Delta J. \tag{2.48}$$

The usefulness of analysing the equation of rotational dynamics for a satellite whose inertia J is traceable to a form as in (2.48) is due to the fact that for the design and stability proof of controllers it is useful to obtain $\dot{\omega}$ in explicit form, as will be seen in Chapter 3. Simplified mathematical models for attitude dynamics (2.43), (2.47) have been derived in the previous section, specifying that they will be used in the following chapters for controller design. Looking at (2.43), (2.47), the inverse of J is required to obtain $\dot{\omega}$ in explicit form. Since J consists of a known and an unknown term, it is useful to exploit this fact in order to formulate the inverse of J in the same way. A useful method for this purpose is the matrix inversion lemma [39, 40], which applies to the inverse of J in (2.48) and returns the following:

$$J^{-1} = (J_0 + \Delta J)^{-1} = J_0^{-1} + \hat{\Delta} J, \tag{2.49}$$

where

$$\hat{\Delta J} - J_0^{-1} \Delta J \left(\mathbf{I}_3 + J_0^{-1} \Delta J \right)^{-1} J_0^{-1}. \tag{2.50}$$

Now, the hypothesis that J is diagonal is also extended to J_0 and ΔJ, so that (2.50) becomes.

$$\frac{1}{J_{ii}} = \frac{1}{J_{0_{ii}}} + \hat{\Delta} J_{ii}, \quad i = x, y, z. \tag{2.51}$$

Therefore, introducing (2.51) into (2.43) we obtain the simplified attitude dynamics equation under assumptions (i)-(iii) and for uncertain J:

$$\dot{\omega}_i = \left(\frac{1}{J_{0_{ii}}} + \hat{\Delta} J_{ii} \right) (d_i - \tau_i), \quad i = x, y, z, \tag{2.52}$$

which is useful because it allows uncertainties to be isolated from known terms, which can thus be used to guide controller design, as will be shown in Chapter 3.

Flexible dynamics

Here, we derive a mathematical model for studying the structural dynamics of flexible appendage attached to rigid spacecraft base. For an easier understanding of this topic, the reader can supplement the reading with Appendix A, where the treatment described below is applied to a satellite with flexible solar panels. In this

way, we intend to characterise the coupling effect between the flexible and rigid structures, which arises in two ways. On the one hand, the deformations due to the low stiffness of the appendages disturb the attitude of the rigid base, on the other hand, the attitude manoeuvres of the rigid base excite the flexible dynamics causing vibrations of the appendages. In this thesis, the coupling between attitude and flexible dynamics is studied through the hybrid-coordinates method firstly proposed in [41], which allows to derive a mathematical model for the flexible appendages employing a combination of the discrete and modal coordinate, deriving a matrix δ describing the coupling effect. In order to obtain the coupling matrix δ, each flexible appendage of the spacecraft is first modeled as a collection of elastically interconnected, discrete rigid sub-bodies. Then, through a Finite Element Method (FEM) analysis the natural modes of the appendages are evaluated, obtaining both the natural frequency and eigenvectors associated to each flexible mode. Finally, the eigenvectors provide the coupling matrix δ, while the parameters of the flexible dynamics equation are obtained from the natural frequencies. Therefore, a δ matrix must be computed for each flexible appendage through its natural modes. In order to obtain the natural modes of each appendage, the FEM analysis is conducted without including structural damping nor external loads applied to the appendage. In general, the equations of motion for a linear and undamped structure may be expressed as a function of the mass matrix M and the stiffness matrix K as follows:

$$M\ddot{v} + Kv = 0, \tag{2.53}$$

where v is the flexible displacement vector and can be expressed as follows for a linear system, in which free vibrations are harmonic:

$$v = \Phi e^{i\Omega t}, \tag{2.54}$$

with Φ and Ω the eigenvector and the natural frequency associated to a specific natural mode. Substituting (2.54) and its second-time derivative into (2.53), and rearranging the equation into an eigenvalue problem as in [42], it becomes:

$$(K - \lambda M)\Phi = 0, \tag{2.55}$$

where Φ enclose the eigenvectors describing each mode shape, while λ is the eigenvalue for each mode and it is related to system's natural frequency since

$\lambda = \Omega^2$. In this work, FEM softwares *Patran/Nastran* was used to solve the (2.55), obtaining the matrices of natural frequencies Ω and of eigenvectors Φ describing each natural mode of a flexible appendage. The latter is obtained in the following form for each flexible appendage installed in the spacecraft:

$$\Phi = \begin{bmatrix} \Phi_1^1 & \Phi_1^2 & \dots & \Phi_1^N \\ \Phi_2^1 & \ddots & & \vdots \\ \vdots & & \ddots & \vdots \\ \Phi_n^1 & \dots & \dots & \Phi_n^N \end{bmatrix} \tag{2.56}$$

where n is the number of sub-bodies each appendage is divided in, and N is the number of natural modes. Each element Φ_i^j of the matrix (2.56) is the eigenvector associated to the natural mode j and corresponding to the centre of the mass of the sub-panel i. Therefore, Φ_i^j is as follows:

$$\Phi_i^j = [T_1, T_2, T_3, R_1, R_2, R_3]^T, \tag{2.57}$$

where $T_1,\ T_2,\ T_3$ are the translational eigenvectors, and $R_1,\ R_2,\ R_3$ are the rotational eigenvectors. Therefore, $\Phi \in \mathbb{R}^{6n \times N}$ as results from (2.56). However, for the construction of the mathematical model of the flexible dynamics we will only consider the first m modes, so that we obtain a truncated matrix $\overline{\Phi} \in \mathbb{R}^{6n \times m}$, with $m < N$. As mentioned above, $\overline{\Phi}$ is used to compute the coupling matrix $\delta \in \mathbb{R}^{m \times 3}$ as follows [41, 43]:

$$\delta = -\overline{\Phi}^T M \left(\Sigma_{0I} - \Sigma_{I0} R^{\times} - r^{\times} \Sigma_{I0} \right), \tag{2.58}$$

where the other quantities are as follows:

- $M \in \mathbb{R}^{6n \times 6n}$ is the generalized inertia matrix of sub-bodies, defined in 6×6 partitioned matrix:

$$M_i = \begin{bmatrix} m_{\text{sub}_i} \mathbf{I}_3 & \mathbf{0}_3 \\ \mathbf{0}_3 & J_{\text{sub}_i} \end{bmatrix}, \quad M = \begin{bmatrix} M_1 & \dots & \mathbf{0}_6 \\ \vdots & \ddots & \vdots \\ \mathbf{0}_6 & \dots & M_n \end{bmatrix}, \tag{2.59}$$

  where $m_{\text{sub}_i}, J_{\text{sub}_i} \in \mathbb{R}^{3 \times 3}$ are the mass of the sub-body i and the inertia tensor of the sub-body i referred to the central axis of inertia, respectively.

- Σ_{0I}, $\Sigma_{I0} \in \mathbb{R}^{6n\times 3}$ consist of 6×3 matrices repeated n times as follows:

$$\Sigma_{0I_i} = \begin{bmatrix} \mathbf{0}_3 \\ \mathbf{I}_3 \end{bmatrix}, \quad \Sigma_{0I} = \begin{bmatrix} \Sigma_{0I_1} \\ \vdots \\ \Sigma_{0I_n} \end{bmatrix} \tag{2.60}$$

$$\Sigma_{I0_i} = \begin{bmatrix} \mathbf{I}_3 \\ \mathbf{0}_3 \end{bmatrix}, \quad \Sigma_{I0} = \begin{bmatrix} \Sigma_{I0_1} \\ \vdots \\ \Sigma_{I0_n} \end{bmatrix} \tag{2.61}$$

  , where $\mathbf{0}_3 \in \mathbb{R}^{3\times 3}$ is the null matrix and $\mathbf{I}_3 \in \mathbb{R}^{3\times 3}$ is the identity matrix.

- $R^\times \in \mathbb{R}^{3\times 3}$ is the skew-symmetric matrix with the components of R, which is the position vector from the center of the mass of the spacecraft to the point on the interface between the rigid body and the flexible appendage.

- $r^\times \in \mathbb{R}^{6n\times 3}$ consists of 6×3 matrices repeated n times as follows:

$$r^\times_{i,0} = \begin{bmatrix} r_i^\times \\ \mathbf{0}_3 \end{bmatrix}, \quad r^\times = \begin{bmatrix} r^\times_{1,0} \\ \vdots \\ r^\times_{n,0} \end{bmatrix} \tag{2.62}$$

  where $r_i^\times \in \mathbb{R}^{3\times 3}$ is the skew-symmetric matrix with the components of r_i, which is the position vector from the point on the interface between the rigid body and the flexible appendage and the center of mass of the sub-body i.

For a better understanding of R and r_i the reader can refer to Figure A.10. Therefore, δ results from (2.58) as a $m\times 3$ matrix, with m the number of natural modes taken into account to build $\overline{\Phi}$. Before giving the details on how δ rules the coupling between flexible and attitude dynamics, let us recall that when a linear elastic structure is vibrating in free or forced vibration, its deflected shape at any given time is a linear combination of all of its normal modes. Therefore, the distribution of flexible displacement v over the appendage is given by:

$$v = \Sigma_i v_i = \Sigma_i \left(\Phi_i \eta_i\right), \tag{2.63}$$

where v_i is the vector of physical displacement consistent with the *i-th* shape mode Φ_i, i.e. the *i-th* column of the Φ matrix in (2.56), and $\eta \in \mathbb{R}^m$ is the modal coordinate

vector. Under the assumption of small elastic deformations, the dynamics equation of η for the flexible appendage attached to the spacecraft is as follows:

$$\ddot{\eta} + C\dot{\eta} + K\eta = -\delta\dot{\omega}, \tag{2.64}$$

where $K \in \mathbb{R}^{m\times m}$ and $C \in \mathbb{R}^{m\times m}$ are the structural stiffness and damping matrix, respectively. K is computed from the natural frequency Ω of the system, which in turn is obtained from the FEM analysis, while C is computed by scaling K with a parameter $\gamma \in \mathbb{R}^{+}$ as follows:

$$K = \begin{bmatrix} \Omega_1^2 & \dots & 0 \\ \vdots & \ddots & \vdots \\ 0 & \dots & \Omega_m^2 \end{bmatrix}, \quad C = \gamma K. \tag{2.65}$$

Eq. (2.64) shows that the flexible dynamics is forced by a term proportional to the angular acceleration of the satellite $\dot{\omega}$, proving that attitude dynamics is coupled to flexible dynamics via the δ matrix as mentioned above. Below, we also show that the δ matrix also specify how the flexible dynamics perturb the attitude dynamics.

Attitude dynamics

In order to derive the attitude dynamics equation for the spacecraft with flexible appendages, consider again the total angular momentum H of the satellite actuated by RWs. For the rigid spacecraft, H is as in (2.30), however the flexibility of the appendages adds the following contribution to the total angular momentum [44, 45]:

$$H_{\text{flex}} = \delta^T \dot{\eta}, \tag{2.66}$$

thus the total angular momentum is

$$H = J\omega + h_{\text{rw}} + \delta^T \dot{\eta}. \tag{2.67}$$

Now, the attitude dynamics equation is obtained from (2.32) by computing the time derivative of (2.67), which results in:

$$J\dot{\omega} = m - \omega \times (J\omega + h_{\text{rw}} + \delta^T \dot{\eta}) - \dot{h}_{\text{rw}} - \delta^T \ddot{\eta}, \tag{2.68}$$

with m as in (2.35) and $\dot{h}_{\text{rw}}$ as in (2.38). Compared to the rotational dynamics equation of rigid spacecraft (2.37), Eq. (2.68) involves a term in $\ddot{\eta}$, which proves that the flexible dynamics perturb the attitude dynamics by means of a torque $\delta\ddot{\eta}$, due to the flexible displacement of the appendages.
Finally, the complete mathematical model for the attitude dynamics of flexible spacecraft actuated by RWs is given by (2.68), (2.64), and (2.38).

Simplified model for attitude dynamics

Now, it can be useful to derive a simplified model to be used for attitude control algorithms design as was done in Subsection (2.2.2). For the same validity assumptions (i)-(iii) of the simplified attitude dynamics equation for the rigid satellite (2.43), it is straightforward to obtain the following simplified attitude dynamics equation for the flexible satellite:

$$J_{ii}\dot{\omega}_i = d_i - \tau_i - (\delta^T\ddot{\eta})_i, \quad i = x,y,z. \tag{2.69}$$

Furthermore, combining (2.51) with (2.69) we obtain a simplified attitude dynamics equation of the flexible spacecraft with uncertain parameters, that will be useful for control algorithm design in next chapter:

$$\dot{\omega}_i = \left(\frac{1}{J_{0_{ii}}} + \hat{\Delta J}_{ii}\right)\left(d_i - \tau_i - (\delta^T\ddot{\eta})_i\right), \quad i = x,y,z. \tag{2.70}$$

2.2.4 Orbital disturbances

This subsection details the orbital perturbations affecting the attitude dynamics spacecraft, which have been incorporated into the dynamics equations in the previous sections via the disturbance torque d. These perturbations arise from the environment in which the satellite moves, for an Earth orbit the most relevant disturbance torques are due to the magnetic field, the solar radiation pressure, the aerodynamic drag, and the gravity-gradient.

Magnetic torque

The magnetic torque is due to the interaction between the Earth's magnetic field and the equivalent magnetic dipole of the satellite, resulting from the electronic compo-

nents onboard. As a result of this interaction, the satellite undergoes a disturbance torque given by

$$d_m = m \times b, \tag{2.71}$$

where m is the spacecraft magnetic dipole moment and b is the Earth's magnetic field, which mostly depends on the instantaneous altitude of the satellite, the intensity and direction of which depend mainly on the satellite's altitude along its orbit.

Solar radiation pressure torque

This disturbance torque is due to the photons emitted by the sun which exchange momentum with the surface of the spacecraft and its magnitude depends by the activity of the Sun, due to seasonal variations according to the Sun's cycles. Therefore, the pressure exerted by the photons on the surfaces of the spacecraft results in a force directed towards the optical center of pressure of the satellite. Then, the force produce a torque around the center of the mass of the spacecraft if the latter does not coincide with the optical center of pressure. This torque is zero when the spacecraft is in the sun's shadow, of course. Instead, when the spacecraft is in the sun's light the torque d_s depends on the solar radiation pressure p, the spacecraft lit area S_{la} normal to sun unit vector s, directed from the sun towards the spacecraft, and the distance from body center of mass to spacecraft optical center of pressure c_{ps} as follows:

$$d_s = -p \left[c_{ps} \int_{S_{la}} (n \cdot s) dS \right] \times s, \tag{2.72}$$

where the integral over S_{la} of $n \cdot s$ gives the the spacecraft projected area normal to sun vector.

Aerodynamic drag torque

This torque is due to the residual air particles in space environment and and mainly disturbs satellites in low Earth orbits. Although these molecules are very few in number, collisions occur with great relative speed, so this effect cannot be neglected. Since the density is so low that fluid mechanics theories based on a continuous model do not apply, the interaction between the atmosphere and the spacecraft must be treated at the molecular level. Assuming that the impact velocity between molecules and satellite is the satellite's own translation velocity v, taking S_{fa} the spacecraft

surface facing the flow, n the unit outward normal to the surface element dS, ρ_a the atmospheric density and c_{pa} the distance between the center of aerodynamic pressure and the center of the mass, the aerodynamic torque d_a acting on the spacecraft is:

$$d_a = c_{pa} \times \left(-\rho_a v \int_{S_{fa}} (n \cdot v) dS \right) \tag{2.73}$$

Gravity-gradient torque

This torque is due to the fact that the gravitational force of the Earth decreases quadratically with distance from the Earth's center. Therefore, any satellite is subject to the gravitational gradient, i.e. not all parts of the body experience equal gravitational force, which results in a disturbance torque. Giving the Earth gravitational parameter μ, the orbital position of the spacecraft center of mass r, and the inertia matrix of the spacecraft J, the torque due to the gravity effects can be evaluated as:

$$d_g = \frac{3\mu}{|r|^5} r \times [J] r \tag{2.74}$$

Chapter 3

Sliding mode control

In this chapter, first the history and evolution of Sliding Mode Control (SMC) is introduced, outlining the features, advantages and disadvantages of this control technique. Special attention is paid to chattering and the techniques reported in the literature to overcome this shortcoming, which is the most severe in SMC. Next, the SMC algorithms analysed in this thesis are described. First, in Section 3.2 the control algorithms are formulated to manipulate the dynamics of a second-order system with a single input. Next, in Section 3.3 the control algorithms are used to manipulate satellite attitude dynamics. To this end, two techniques for chattering reduction are initially compared, evaluating their effectiveness in this respect as well as for pointing accuracy and design complexity in the context of satellite attitude control. Then, real system issues such as actuator saturations and parametric uncertainties are considered, designing the controller so that the actuators can realise the output of the control law and the closed-loop system is stable.

3.1 Overview on sliding mode control

Sliding mode control (SMC) is a non-linear Variable Structure Control (VSC) method that was first introduced by V. Utkin in his work published in 1977 [46]. Here, it is stated that the design of first order sliding mode control (FOSM), i.e. the first generation of SMC, consists of defining:

- a sliding variable as a function of the system output and its time derivatives;

- a discontinuous control law to force the system's trajectories.

Then, the control law must first drive the value of the sliding variable to zero, i.e. the system is driven in a domain named sliding surface, and then it must maintain the system on the sliding surface in spite of uncertainties and perturbations [47]. If the control law works as described, for appropriately chosen sliding surface the output of the system can meet the desired reference input [48]. In particular, the sliding surface is designed to give the desired trajectories of the system in the state-space during the sliding phase, so that state errors tend to zero at this stage.
Based on the above description, the sliding mode control process can be split into two time stages: the *reaching phase*, in which the sliding variable is non-zero, and the *sliding phase*, in which the sliding variable is null. In fact, as soon as the control process is activated, the initial conditions of the system will generate a non-zero sliding variable, i.e. the system is not on the sliding surface. So, during reaching phase the states of the system move towards the sliding surface, following a system trajectory generated by the continuous control input [49]. Then, the reaching phase ends as soon as the sliding variable is zero, at which point the system is on the sliding surface and the sliding phase begins. During this phase the discontinuous control input keeps the system on the sliding surface, and the output error tends to zero as the closed-loop system moves along the trajectory defined by the sliding surface.
FOSM offers the following main advantages:

- the closed-loop system is insensitive to bounded matched uncertainties/disturbances when it is in sliding phase [50];
- the closed-loop system converge in finite time on the sliding surface [51], [52];
- reduced order of the sliding equations [53].

These advantages, together with the ease of tuning and implementation also with low computational power, have made SMC algorithms very attractive in the control community, providing solutions in a variety of practical applications. Nevertheless, FOSM suffers from the following drawbacks:

- chattering;
- the closed-loop system in sliding motion is not insensitive to unmatched uncertainties/disturbances;

- the sliding variables converge in finite time but the state errors only converge asymptotically;
- the sliding surface design is restricted to have relative degree one with respect to the control, i.e., higher order derivatives are required for the sliding surface design.

In particular, this Chapter focuses on chattering issue, that was the main obstacle to implementation of SMC theory at its outset [54]. In fact, this is a high frequency motion in the vicinity of the sliding surface that can lead both to degrade the system efficiency and to damage the mechanical moving parts of the system [55]. Then, there are tipically three causes of chattering: (I) fast dynamics neglected in the model, (II) finite sampling time of the controller, and (III) control law discontinuities across the sliding surface, with the latter becoming more critical the greater the control gain [56]. Because of its criticality, the chattering phenomenon has been extensively analysed since the origin of SMC, and several techniques emerged to overcome this drawback. Among these, the use of Boundary-Layer Sliding Mode [48, 57], higher order sliding mode control [58–60], control gains adaptation based on adaptive rules or fuzzy logic [61–64], and extended state and disturbance observers [65, 66] are mentioned in the literature.
The idea of Boundary-Layer Sliding Mode Control (BLSMC) to alleviate chattering is to smooth out the discontinuity of the control law in a small area neighbouring the sliding surface, i.e. the boundary layer [67, 68]. In other words, outside the boundary layer the control law ensures that the latter is attractive, hence invariant: all trajectories of the system reach and then remain within the boundary layer. Instead, inside it, the control law is interpolated, replicating the ideal control with a smoother function. Certainly, this solution alleviates chattering, but at the same time leads to tracking with reduced precision rather than 'perfect' tracking, i.e. the error does not asymptotically tend to zero [53].
As mentioned above, chattering is also caused by the discontinuous control that excites the unmodelled dynamics. This problem, typical of FOSM, is alleviated by higher order sliding controllers (HOSM), in which not only the sliding variable is brought to zero, but also its $k-1$ successive derivatives ($k-$order sliding mode) [69]. In these algorithms, discontinuous control is 'hidden' in the derivative of the sliding variable, which allows for a considerable reduction in chattering [47]. In particular, in Second Order Sliding mode control (SOSM) the discontinuous control appears

in the first time derivative of the sliding variable, which is driven to zero as well as the sliding variable itself [70, 71]. The concept of SOSM was introduced during the second half of the 1980s with the Twisting algorithm, which seemed to solve the chattering issue for system of relative degree one [58, 72]. However, the chattering reduction strategy in Twisting SMC required knowledge of the derivative of the sliding variable, which emerged as a critical issue in this algorithm [69]. This was solved during the 1990s by a new SOSM named Super-Twisting (STW) algorithm [58, 73]. In fact, STW allows both to replace the discontinuous controller with a continuous one and to alleviate the chattering with no knowledge of the time derivative of the sliding variable [72, 69, 74]. Nevertheless, the STW design requires the boundaries of the disturbance gradient to be know [75], and the chattering can only be mitigated, but not completely removed [76]. Furthermore, the tuning of control parameters to ensure both compensation of uncertainties and chattering reduction is a tricky task, and the reduction of the amplitude of high-frequency oscillations with respect to the FOSM is not always achieved. [55].

As mentioned above, other techniques to reduce chattering include the use of extended state and disturbance observers and control gains adaptation based on adaptive rules or fuzzy logic. However, these methods were not investigated in this work, which is why they are only briefly described below. The observer-based approach allows the high-frequency component of the implant dynamics to be bypassed, so that the unmodelled dynamics are not excited and ideal sliding arises [77]. However, This approach reduces the problem of robust control to the problem of exact robust estimation and, consequently, can lead to the deterioration of robustness with respect to the plant uncertainties/disturbances due to the mismatch between the observer and plant dynamics [78]. Finally, the purpose of adapting control gains is to establish a sliding mode in finite time with no over-estimation of the gains with respect to the a priori unknown true value of uncertainties [61]. Thus, the adaptation aims to achieve control gains to be as small as possible whereas sufficient to counteract the uncertainties/perturbations. Certainly, smaller control gains can alleviate chattering, so the development of control algorithms with adaptation has attracted the attention of many scientists and control engineers [62]. Another aspect that makes this approach fascinating is the possibility of designing a SMC without the knowledge of uncertainties/disturbances limits. However, the design of adaptive laws is a challenging task, as some of the solutions presented overestimate the gains, do not guarantee tracking performance, or requires the usage of low pass filters/estimators and the

knowledge of the disturbances bounds [79–82].
Given this overview on SMC, the sections below delve into the equations and design of FOSM and STW, which are the algorithms subsequently used for satellite attitude control.

3.2 Sliding mode control for second order scalar system

This section details the SMC control algorithms that will be employed next for satellite attitude control purposes. Instead, here we consider a second-order dynamic system with a single input, and SMC algorithms will be designed to manipulate the dynamic system so that it follows a reference trajectory. First, the equations of the FOSM algorithm are detailed and the stability of the closed-loop system is proven. Next, the BLSMC approach is applied to modify the classical FOSM algorithm with the aim of eliminating chattering in the closed-loop dynamics, and the reduction in tracking accuracy is characterised in a mathematical perspective. Finally, the design procedure for the STW control algorithm is given, emphasising the equations required to set the gains of this controller.

3.2.1 First order sliding mode control

The purpose of this subsection is to recall both the equations and the design of a FOSM to manipulate a second-order dynamic system with a single input. All results reported in this subsection are already found in the literature (see in exchange [83]). In order to present classical FOSM, consider the following nonlinear second order system with a single input:

$$\begin{aligned} \dot{x}_1 &= x_2 \\ \dot{x}_2 &= f(x) + u + d \end{aligned} \tag{3.1}$$

where $x = [x_1, x_2] \in \mathbb{R}^2$ is the state vector, f is a known function describing the features of the system, and d is an unknown, bounded disturbance such that $|d| < \overline{d}$. Furthermore, d acts in same channel of the control input u, i.e. d is a matched disturbance. The control problem is to make the dynamics in (3.1) follow a feasible

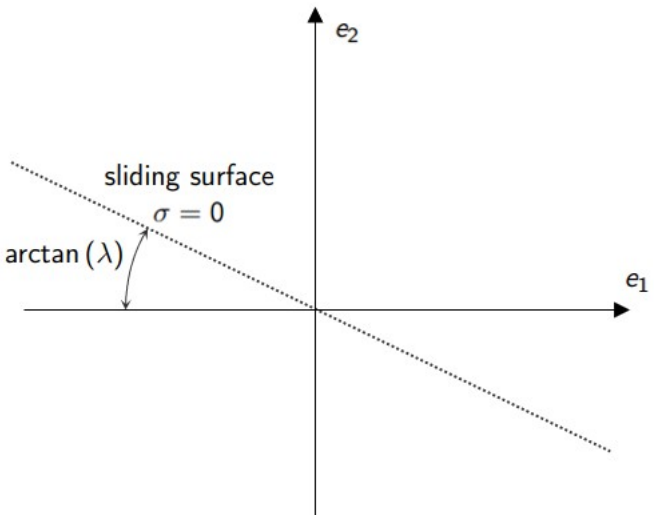

Fig. 3.1 The sliding surface

reference trajectory $x^* = [x_1^*, x_2^*] \in \mathbb{R}^2$, with $\dot{x}_1^* = x_2^*$. So, the error $e = [e_1, e_2] \in \mathbb{R}^2$ is defined as follows:

$$e_1 = x_1^* - x_1 \tag{3.2a}$$

$$e_2 = x_2^* - x_2 = \dot{e}_1 \tag{3.2b}$$

and the control objective is to steer to zero the tracking error e_1.
As pointed out above, the design of a FOSM control algorithm consists of defining both the sliding surface and the control law. The sliding surface is the domain of space where the sliding variable is null, the latter is chosen to be linear as follows:

$$\sigma = e_2 + \lambda e_1, \quad \lambda \in \mathbb{R}^+ \tag{3.3}$$

So, in the phase plane (e_1, e_2) the sliding surface $\sigma = 0$ is a straight-line whose slope is given by the parameter λ, as Fig. (3.1) shows. Before dealing with convergence properties during sliding phase, system (3.1) must be brought to the sliding surface. Thus, the control problem is to design a control law able to keep the system on the domain $\sigma = 0$. In order to achieve this task, the control law is selected as follows in

FOSM:

$$u = u_{\text{eq}} + u_{\text{sw}} \tag{3.4a}$$

$$u_{\text{eq}} = \dot{x}_2^* - f(x) + \lambda e_2 \tag{3.4b}$$

$$u_{\text{sw}} = k\,\text{sign}(\sigma), \quad \text{sign}(\sigma) = \begin{cases} 1 & \text{if} \quad \sigma > 0 \\ -1 & \text{if} \quad \sigma < 0 \\ 0 & \text{if} \quad \sigma = 0 \end{cases} \tag{3.4c}$$

Before giving the theorem for the finite-time convergence at $\sigma = 0$ for the closed-loop system (3.1), (3.3), (3.4), the following property (proved in [84]) is recalled.

Lemma 3.1. *Consider the system*

$$\dot{z} = g(z,t), \quad y = h(z,t), \tag{3.5}$$

where f and g are continuous in t and locally Lipschitz in $x \in \mathbb{R}$, and take the quadratic Lyapunov function

$$V(z,t) = y^2. \tag{3.6}$$

If there exist real numbers $\alpha > 0$ and $\beta \in (0,1)$ satisfying the following:

$$\dot{V}(z,t) \leq -\alpha V^{\beta}(z,t) \quad \forall (z,t) :\ V > \bar{y}^2 \tag{3.7}$$

then the output of system (3.5) converges in finite time to the set

$$\mathfrak{B}_{\bar{y}} = \{z,\ |y| \leq \bar{y}\} \tag{3.8}$$

and the reaching time T is bounded by:

$$T \leq \frac{\max\left\{0,\ V_{y_0}^{(1-\beta)} - V_{\bar{y}}^{(1-\beta)}\right\}}{\alpha(1-\beta)} \tag{3.9}$$

Theorem 3.1. *The trajectories of the system (3.1), (3.3) with the control law (3.4) are proved to converge in finite-time to $\sigma = 0$ if $k > \overline{d}$, and the reaching time is*

bounded as follows:

$$T \leq 2\frac{\sqrt{V_{\sigma_0}}}{k-\overline{d}} \tag{3.10}$$

with $\sigma_0 = \sigma(0)$ *and* $V_{\sigma_0} = V(\sigma_0)$.

Proof. of Theorem 3.1

Consider the following candidate quadratic Lyapunov function

$$V = \sigma^2, \tag{3.11}$$

whose derivative is:

$$\dot{V} = 2\sigma\dot{\sigma} \tag{3.12}$$

$\dot{\sigma}$ is obtained by computing the time-derivative of the sliding variable (3.3):

$$\dot{\sigma} = \dot{e}_2 + \lambda\dot{e}_1 = \dot{x}_d - \dot{x}_2 + \lambda\dot{e}_1 \tag{3.13}$$

$\dot{x}_2$ is as in Eq. (3.1), and from Eq. (3.2b) it is $\dot{e}_1 = e_2$. So, the following is obtained:

$$\dot{\sigma} = \dot{x}_2^* - f(x) - u - d + \lambda e_2 \tag{3.14}$$

Introducing Eq. (3.14) into Eq. (3.12), the latter becomes:

$$\dot{V} = 2\sigma\left(\dot{x}_2^* - f(x) - u - d + \lambda e_2\right) \tag{3.15}$$

because $u = u_{\text{eq}} + u_{\text{sw}}$, with u_{eq} as in Eq. (3.4b) and u_{sw} as in Eq. (3.4c):

$$\dot{V} = 2\sigma\left(-k\ \text{sign}(\sigma) - d\right) = 2\left(-k\sigma\ \text{sign}(\sigma) - \sigma d\right) \tag{3.16}$$

since $\sigma \cdot \text{sign}(\sigma) = |\sigma|$, and $-\sigma d < |\sigma|\overline{d}$:

$$\dot{V} \leq 2\left(-k|\sigma| + \overline{d}|\sigma|\right) = 2\left(-k + \overline{d}\right)|\sigma| = -2\left(k - \overline{d}\right)\sqrt{V_{\sigma_0}} \tag{3.17}$$

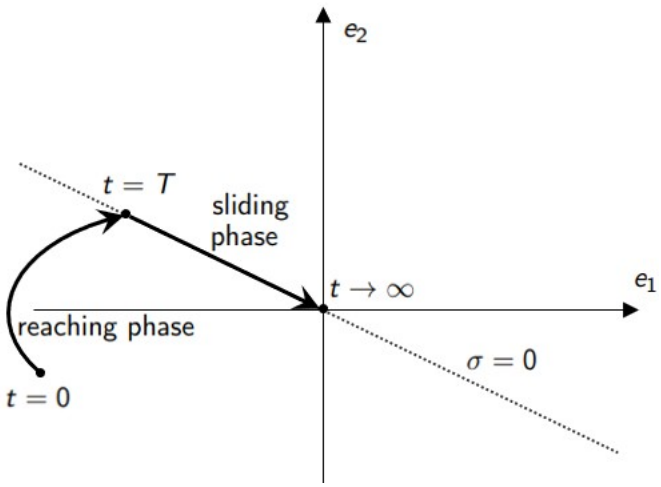

Fig. 3.2 Reaching phase and sliding phase

Due to Eq. (3.17), Lemma 3.1 applies for $z = x$, $y = \sigma$, $\alpha = 2(k - \overline{d}) > 0$, $\beta = 1/2 \in (0,1)$, and $\overline{y} = 0$ and the proof is complete. □

At this point it has been proven that in FOSM $\exists\ T$ s.t. $\sigma = 0\ \forall\ t \geq T$. So the reaching phase ends for $t = T$, after that the system remains in the domain $\sigma = 0$ and is in sliding motion. Now, consider the trajectories of the system during sliding phase, which can be described by the following homogeneous linear time-invariant differential equation resulting from the combination of Eqs. (3.2b), (3.3), and Theorem 3.1:

$$\begin{cases} e_2 &= \dot{e}_1 \\ \sigma &= e_2 + \lambda e_1 = 0 \end{cases} \implies \quad \dot{e}_1 + \lambda e_1 = 0 \tag{3.18}$$

Equation above reveals that if $\lambda > 0$ is chosen, both e_1 and e_2 asymptotically converge to zero during sliding phase. Finally, a qualitative example of the trajectory followed by the closed-loop system is in Fig. 3.2.

3.2.2 Boundary-layer first order sliding mode control

This subsection focuses on the application of BLSMC method to FOSM algorithm described in Subsection 3.2.1. The resulting control algorithm is named Boundary-Layer First Order Sliding Mode (BLFOSM), and consists of smoothing out the discontinuities of the control law (3.4c) in a thin boundary layer neighbouring the

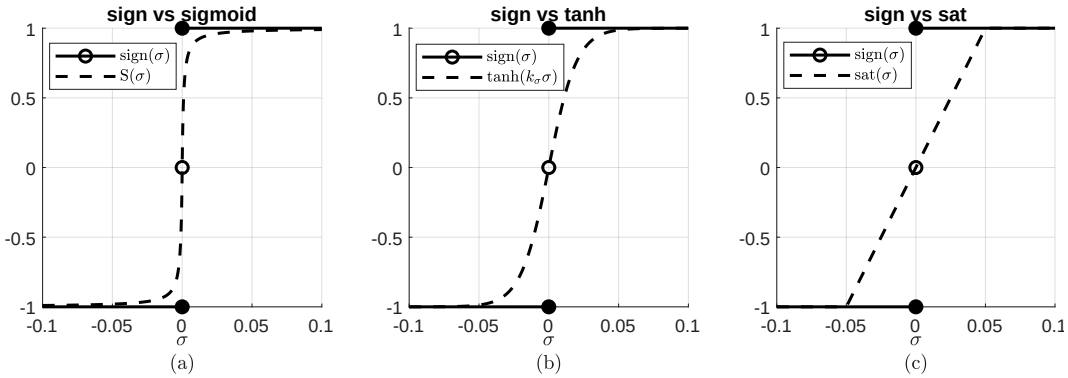

Fig. 3.3 Sign function approximation

sliding surface $\sigma = 0$ (Eq. 3.3). In the literature, several functions have been proposed to approximate the $sign(\sigma)$ function in Eq. (3.4c), including:

- Sigmoid function: $S(\sigma) = \frac{\sigma}{|\sigma|+\varepsilon}$, Fig. 3.3a. Here, ε is a small positive scalar whose value defines the level of approximation of the *sign* function. In particular: $\lim_{\varepsilon \to 0} S(\sigma) = \text{sign}(\sigma)$. In that case, Eq. (3.4c) is replaced by the following:

$$u_{\text{sw}} = k\, S(\sigma) \tag{3.19}$$

- Hyperbolic tangent function: $\tanh(k_\sigma \sigma)$, Fig. 3.3b. Here, k_σ is a positive gain whose value defines the level of approximation of the *sign* function. In particular: $\lim_{k_\sigma \to \infty} \tanh(k_\sigma \sigma) = \text{sign}(\sigma)$. In that case, Eq. (3.4c) is replaced by the following:

$$u_{\text{sw}} = k \tanh(k_\sigma \sigma) \tag{3.20}$$

- Saturation function: $\text{sat}(\sigma)$, Fig. 3.3c. Here, $\overline{\sigma}$ is a small positive scalar such that:

$$\text{sat}(\sigma) = \begin{cases} \frac{\sigma}{\overline{\sigma}} & \text{if} \quad |\sigma| \leq \overline{\sigma} \\ \text{sign}(\sigma) & \text{if} \quad |\sigma| > \overline{\sigma} \end{cases} \tag{3.21}$$

  Then, $\lim_{\overline{\sigma} \to 0} \text{sat}(\sigma) = \text{sign}(\sigma)$. In that case, Eq. (3.4c) is replaced by the following:

$$u_{\text{sw}} = k\, \text{sat}(\sigma) \tag{3.22}$$

Although the above functions allow a reduction of chattering, they also decrease the tracking accuracy with respect to FOSM. In fact, the approximation of the *sign*

function with a smoother one does not allow the closed-loop system to stay exactly on the sliding surface. Rather, during reaching phase the closed-loop system converges to a boundary layer neighboring the sliding surface (fig. 3.4), and after that the trajectories move inside this set. The dimensions of the boundary layer depends on which function is chosen to smooth out the discontinuities. In exchange, for the saturation function we can state the following corollary:

Corollary 3.1. *The system (3.1), (3.3), with the control law (3.4a), (3.4b), (3.21), and (3.22) is proved to converge in finite time to the boundary layer*

$$\mathfrak{B}_{\overline{\sigma}} = \{x \in \mathbb{R}^2,\ |\sigma| \leq \overline{\sigma}\} \tag{3.23}$$

if $k > \overline{d}$*. The reaching time is bounded as follows:*

$$T \leq 2\frac{\max\left\{0,\ \sqrt{V_{\sigma_0}} - \sqrt{V_{\overline{\sigma}}}\right\}}{k - \overline{d}} \tag{3.24}$$

Proof. of Corollary 3.1
The proof is still based on Lemma 3.1, and is similar to Proof 3.2.1 of Theorem 3.1. In fact, $\forall \sigma : |\sigma| > \overline{\sigma}$, we have $\text{sat}(\sigma) = \text{sign}(\sigma)$ according to Eq. (3.21). Therefore, Eq. (3.17) is obtained $\forall \sigma : |\sigma| > \overline{\sigma}$ and Lemma 3.1 applies for $z = x$, $y = \sigma$, $\alpha = 2(k - \overline{d}) > 0$, $\beta = 1/2 \in (0,1)$, and $\overline{y} = \overline{\sigma}$. □

Since the BLFOSM only guarantees that σ converges within the set (3.23) (but does not necessarily converge on the sliding surface), this control algorithm can not guarantee that the tracking errors asymptotically converge to zero during sliding phase, which was the case in FOSM. Instead, BLFOSM can only ensure that the tracking error converges to a set around zero whose dimensions depend on both $\overline{\sigma}$ and λ. In order to establish this set, consider the equations governing the sliding phase in BLFOSM. From Eqs. (3.18) and (3.23), the compensated dynamic is as follows:

$$\dot{e}_1 + \lambda e_1 = \sigma \in [-\overline{\sigma},\ \overline{\sigma}] \tag{3.25}$$

Now, it is worth referring to the following lemma, which comes from [85, Theorem 4.18].

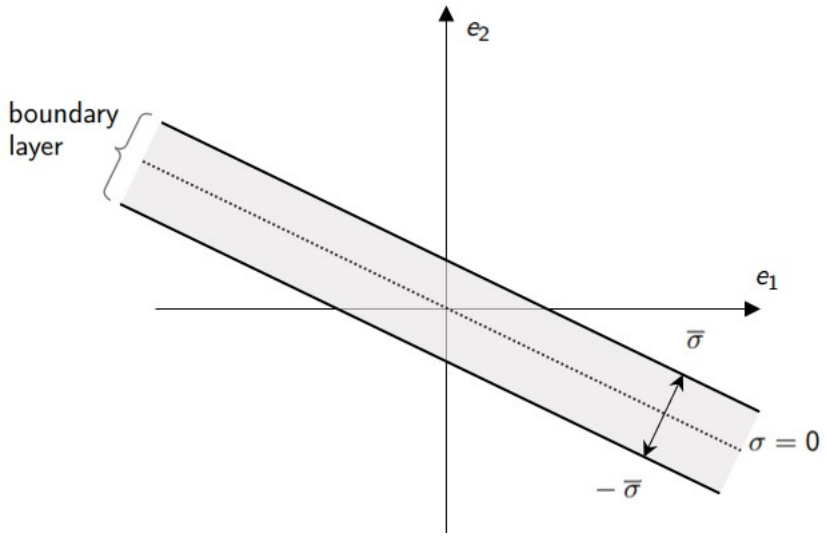

Fig. 3.4 The boundary layer neighbouring the sliding surface

Lemma 3.2. *Consider the system*

$$\dot{z} = g(z,t) \tag{3.26}$$

where g is continuous in t and locally Lipschitz in $x \in \mathbb{R}$, and take the square Lyapunov function:

$$V(z,t) = z^2. \tag{3.27}$$

Assume that, for some $\varepsilon > 0$ along the trajectories of (3.26), for any interval $[\underline{V}, \overline{V}]$ where $\varepsilon < \underline{V} < \overline{V}$, there exists $\upsilon > 0$ such that:

$$V(z,t) \in [\underline{V}, \overline{V}] \implies \dot{V}(z,t) < -\upsilon. \tag{3.28}$$

Then, the output of system (3.26) globally asymptotically converge to a set

$$\mathfrak{B}_{\overline{z}} = \{(z,t) : V(z,t) \leq \varepsilon\}. \tag{3.29}$$

Theorem 3.2. *When the system (3.1) is governed by the compensated dynamics (3.25) (and this is true $\forall\, t \geq T$) the tracking error e_1 asymptotically converge to a*

set $\mathfrak{B}_e$ defined as:

$$\mathfrak{B}_e = \left\{ e_1 : \; e_1^2 \leq \left(\frac{\overline{\sigma}}{\lambda} \right)^2 \right\} \tag{3.30}$$

Proof. of Theorem 3.2
Consider the candidate Lyapunov function

$$V = e_1^2 \tag{3.31}$$

which is in the same form as (3.26). Then, its time derivative is given by:

$$\dot{V} = 2e_1\dot{e}_1 \tag{3.32}$$

According to Eq. (3.25), it is $\dot{e}_1 = -\lambda e_1 + \sigma$, so equation above becomes as follows:

$$\dot{V} = 2e_1\left(-\lambda e_1 + \sigma\right) = -2\left(\lambda e_1^2 + e_1\sigma\right) \leq -2\left(\lambda e_1^2 + |e_1|\overline{\sigma}\right) = 2|e_1|\left(-\lambda|e_1| + \overline{\sigma}\right). \tag{3.33}$$

Now, we apply Lemma 3.2 with $\varepsilon = \left(\frac{\overline{\sigma}}{\lambda}\right)^2$. For each $\underline{V} > \varepsilon$, so that $\underline{V} - \varepsilon > 0$, we obtain from 3.33,

$$V > \underline{V} \implies |e_1|^2 \geq \underline{V} \implies \dot{V} \leq -2\lambda\underline{V}(V - \varepsilon) \leq -2\lambda\underline{V}(\underline{V} - \varepsilon) = -\upsilon < 0 \tag{3.34}$$

which shows 3.28 and the results follows from Lemma 3.2 □

3.2.3 Super-twisting sliding mode control

In this subsection, the equations of STW algorithm are applied to the dynamic system (3.1) in order to drive to zero the tracking error e_1 (Eq. 3.2a). All results reported in this subsection are already found in the literature (see in exchange [1]).
For the design of the STW control algorithm, the sliding variable σ is selected as in Eq. (3.3). Thus, the $\sigma-$dynamics is the same as in Eq. (3.14), but it should be first

rewritten as follows for controller design purposes:

$$\dot{\sigma} = m + n \cdot u \tag{3.35}$$

From the comparison between Eqs. (3.14) and (3.35) it results that:

$$m = \dot{x}_2^* - f(x) - d + \lambda e_2, \quad n = -1 \tag{3.36}$$

Furthermore, assume that for some positive constants C, K_m, K_M, q, and U_M the following hold:

$$|\dot{m}| + U_M |\dot{n}| \leq C, \quad 0 \leq K_m \leq n \leq K_M, \quad \left|\frac{m}{n}\right| \leq q U_M, \quad 0 < q < 1 \tag{3.37}$$

Now, the control law in the STW algorithm is selected as follows:

$$u = u_1 + u_2 \tag{3.38a}$$

$$u_1 = -\gamma |\sigma|^{\frac{1}{2}} \operatorname{sign}(\sigma) \tag{3.38b}$$

$$\dot{u}_2 = \begin{cases} -u & \text{if} \quad |u| > U_M \\ -\eta \operatorname{sign}(\sigma) & \text{if} \quad |u| \leq U_M \end{cases} \tag{3.38c}$$

Finally, the convergence properties of σ, $\dot{\sigma}$ are stated in the following theorem, exposed and proved in [1].

Theorem 3.3. *The trajectories of system (3.35) with the control law (3.38) converge in finite time to $\sigma = \dot{\sigma} = 0$ if*

$$K_m \eta > C, \quad \gamma > \sqrt{\frac{2}{K_m \eta - C}} \frac{(K_m \eta + C) K_M (1+q)}{K_m^2 (1-q)} \tag{3.39}$$

The control input u (3.38a) enters in finite time the segment $[-U_M, U_M]$ and stays there. It never leaves the segment, if the initial value is inside at the beginning.

A typical phase portrait of the STW algorithm is shown in Fig. (3.5). At this point, it has been proven that in STW algorithm the closed-loop system reach the sliding surface in finite time. After that, the trajectories lies in the domain $\sigma = 0$ during sliding phase. Thus, the convergence properties of the tracking error e_1 are the same as discussed in Subsection 3.2.1.

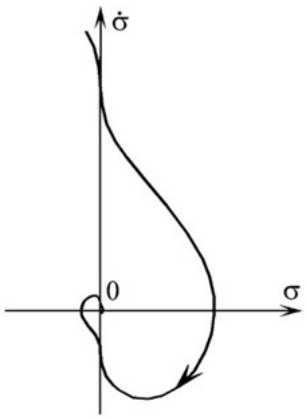

Fig. 3.5 Phase portrait in STW [1]

3.3 Sliding mode control for spacecraft applications

This Section presents the SMC algorithms developed in this thesis for spacecraft attitude control purposes. As explained in detail in the previous chapter, attitude stabilisation involves highly non-linear kinematics and dynamics, leading to a robust line of research in this field [86]. The various control techniques proposed by the scientific community have been briefly presented in the Introduction. Instead, below we present an overview of the SMC applications for spacecraft attitude control. The first application of SMC to spacecraft attitude control was proposed in [87], a work that pioneered a series of SMC controllers proposed for this field. In order to avoid chattering in the closed-loop dynamics, both BLFOSM [88] and HOSM [89] are proposed with linear sliding surface to achieve attitude tracking asymptotically, but for HOSM control, the theoretical analysis is complex and computation burden is heavy [90]. To improve convergence rate, attitude stabilization with terminal sliding mode (TSM) was further proposed in [91]. Combining the advantage of TSM with conventional SMC, the fast TSM (FTSM) is applied in [92] to accelerate the algorithm convergence speed while simultaneously guaranteeing the spacecraft attitude error dynamics to converge to small regions in finite time. Although TSM algorithms are able to achieve the finite-time stability, they may suffer from the singularity issue. Therefore, a non-singular TSM (NTSM) which successfully avoid this drawback of traditional TSMC was proposed in [93, 94]. Moreover, a non-singular FTSM (NFTSM) control strategy was developed in [95] for attitude control of a flexible spacecraft. NFTSM allows to combine the advantage of NTSMC and the conventional SMC, thereby accelerating the algorithm convergence speed while

simultaneously guaranteeing the finite-time stability and the avoidance of singularity problem.
In this project, we used the control algorithms seen in Section 3.2 to provide attitude control of satellites. Therefore, these algorithms will be brought to bear on the mathematical models of spacecraft attitude dynamics presented in Chapter 2. With a view to realising attitude control systems as close as possible to the 'flyable' format as required by EASA standards [96], several practical aspects were considered in the design of the control algorithms:

- attenuation of the chattering, which ruins the closed-loop dynamics and degrades the actuators for attitude control;
- compliance with hardware constraints, i.e. avoidance of actuator saturation in order to achieve feasible manoeuvre profiles. Also, the limited update frequency of the controller is considered.
- robustness against both the parametric uncertainties and environmental disturbances which affects the spacecraft attitude dynamics as seen in Chapter 2;
- tracking accuracy, in order to obtain a depointing error as small as possible;
- control effort, so that the control algorithm does not require an excessive amount of power to activate the actuators.

The following subsections delve into the design of SMC for spacecraft attitude dynamics, expounding the algorithms developed during this phase of the work to address the issues above.

3.3.1 Chattering attenuation in SMC

This work aims to investigate the performance developed by both BLFOSM and STW algorithms to control the spacecraft attitude dynamics. The comparison seeks to evaluate the performance developed by the two SMC algorithms, with a focus on tracking accuracy, complexity and chattering elimination, also with low update frequency of the controller. An attitude maneuver for inertial pointing is considered as practical application, and the following assumptions are used to synthesise the control law:

- the spacecraft is supposed to be rigid and with three known principal central axes of inertia;
- the actuation systems consists of three RWs, which are arranged in a cluster whose center of mass coincides with the one of the spacecraft;
- the rotation axis of each wheel is aligned with a principal central axis of the spacecraft;
- the body frame (see Chapter 2) is attached to the principal central axis of the spacecraft;
- the objective of the maneuver is to align the body frame with the inertial frame;
- both the spacecraft and the reaction wheels are started with zero-angular speed;
- the angular momentum absorbed by the wheels to counteract the external disturbances is neglectable;
- small orientation angles are considered between body frame and inertial frame.

According to these assumptions, it follows that:

- each wheel provides active control around one axis of the spacecraft, so that each DOF has a dedicated control channel and a control law can be derived separately for each axis;
- the kimenatics and dynamics errors equations are given by Eqs. (2.27) and (2.43), respectively, as explained in Chapter 2.

Therefore, the complete mathematical model used for control design consists of three SISO systems as follows:

$$\begin{cases} \dot{q}_{v,i} &= \frac{1}{2}\omega_i \\ \dot{\omega}_i &= \frac{1}{J_{ii}}(\tau_i + d_i) \end{cases} \qquad i = x,y,z \tag{3.40}$$

Where the subscript i will be used in the rest of the subsection to indicate a generic satellite axis, i.e. x, y, and z of the body frame. For each of them, a sliding variable is first defined through the states of the system (3.40), so that the tracking errors converge to zero when the system is in sliding mode. After that, both the FOSM

and STW control laws are derived to ensure the system is able to reach the sliding surface.
Since for each axis the attitude control problem is a second-order dynamic system, the following conventional sliding variable is selected for both FOSM and STW algorithms:

$$\sigma_i = J_{ii}\left(\omega_i + \lambda q_{v,i}\right), \quad \lambda \in \mathbb{R}^+, \tag{3.41}$$

where λ is selected to be the same for the three axes, which implies that the three sliding surfaces have the same inclination. Furthermore, $\lambda \in \mathbb{R}^+$ ensures that $\sigma_i = 0$ is a stable domain. This can be proven by introducing the first of Eq. (3.40) into Eq. (3.41):

$$\sigma_i = J_{ii}\left(2\dot{q}_{v,i} + \lambda q_{v,i}\right) \tag{3.42}$$

which becomes an homogeneous linear differential equation for $\sigma_i = 0$, so both $q_{v,i}$ and ω_i asymptotically converge to zero.

Attitude control with FOSM algorithm

The FOSM control law to manage the spacecraft attitude dynamics is as follows:

$$\tau_i = -k\ \mathrm{sign}(\sigma_i) - \frac{1}{2}J_{ii}\lambda_i\omega_i, \quad i = (x,y,z) \tag{3.43}$$

in which the control gain $k \in \mathbb{R}^+$ is the same for the three axes and is selected to be

$$k > \overline{d}, \quad \overline{d} = \left\|(d_x,\ d_y,\ d_z)\right\|_\infty \tag{3.44}$$

Note that this choice is conservative, as it relates the choice of the control gain for each axis to the worst-case scenario. One could also choose the control gain according to the magnitude of disturbance for each axis, while still guaranteeing stability and reducing the control effort, especially if the magnitudes of disturbance are significantly different on each the axes. However, in satellite attitude control it is quite common practice to select the same control gain for each axis. Then, the finite time convergence of the closed-loop system (3.40) - (3.44) to $\sigma_i = 0$ is proven by using Lemma 3.1 and the following quadratic Lyapunov function:

$$V = \sigma_i^2 \tag{3.45}$$

whose time derivative is given by:

$$\dot{V} = 2\sigma_i \dot{\sigma}_i \tag{3.46}$$

$\dot{\sigma}_i$ is obtained by introducing Eq. (3.40) in the time-derivative of Eq. (3.41):

$$\dot{\sigma}_i = J_{ii}\left(\dot{\omega}_i + \lambda \dot{q}_{v,i}\right) = \tau_i + d_i + \frac{1}{2} J_{ii} \lambda \omega_i \tag{3.47}$$

so, $\dot{V}$ becomes as follows:

$$\dot{V} = 2\sigma_i \left(\tau_i + d_i + \frac{1}{2} J_{ii} \lambda \omega_i \right) \tag{3.48}$$

then, the control law (3.43) is inserted, with k as in Eq. (3.44):

$$\dot{V} = 2\sigma_i \left(-k \operatorname{sign}(\sigma_i) + d_i\right) \leq -2\left(k - \overline{d}\right) |\sigma_i| = -2\left(k - \overline{d}\right) \sqrt{V_{\sigma_{0_i}}} \tag{3.49}$$

Due to Eq. (3.49), Lemma 3.1 applies for $z = (q_{v,i}, \omega_i) \in \mathbb{R}^2$, $y = \sigma_i$, $\alpha = 2(k - \overline{d}) > 0$, $\beta = 1/2 \in (0,1)$, and $\bar{y} = 0$. The proof is complete and the closed-loop system reaches the sliding manifold $\sigma_i = 0$ in finite time. After that, the dynamics is ruled by Eq. (3.42) and the errors asymptotically converge to zero. Finally, apart from λ, the only control parameter to be selected is k, which is obtained via the upper limit of the external torque $\overline{d}$, dependent on orbital disturbances as described in Chapter 2.

Chattering attenuation in FOSM

A major focus of this work, as mentioned at the beginning of the subsection, is the evaluation of BLSMC techniques for FOSM algorithm. For this reason, an hyperbolic tangent (*tanh*) is used to replace the *sign* function in the control law (3.43) to mitigate the chattering effect as follows:

$$\tau_i = -k \tanh(k_\sigma \sigma_i) - \frac{1}{2} J_{ii} \lambda_i \omega_i \tag{3.50}$$

with the sliding variable σ_i defined in Eq. (3.41). Instead, k_σ is a positive gain that mitigate the level of approximation of the *sign* function, as in Eq. (3.20). This is shown in Fig. (3.6), where the *tanh* function is plotted with different values of the

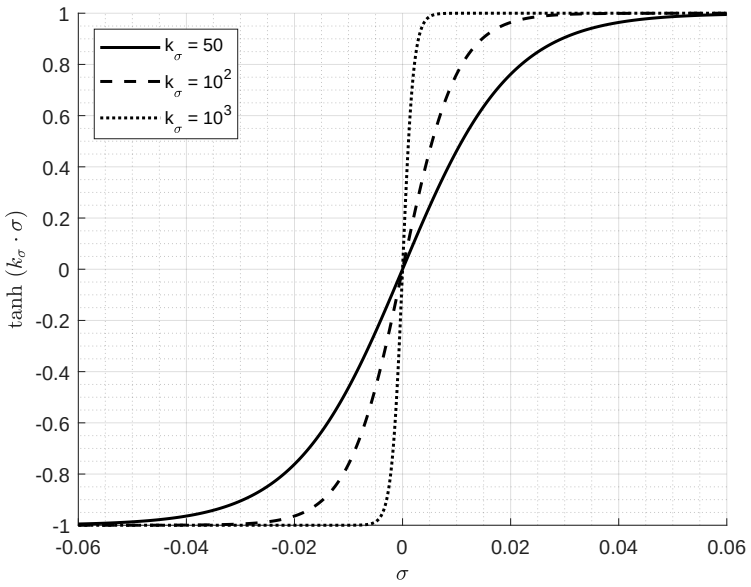

Fig. 3.6 Effect of k_σ on the hyperbolic tangent

gain k_σ. In the case $k_\sigma = 10^2$ the *tanh* function is equivalent to the *sign* function for any $|\sigma| > 0.03$ (approximately), while $tanh(k_\sigma \sigma) < sign(\sigma)\ \forall\ 0 < |\sigma| < 0.03$. Therefore, the value of k_σ determines the dimension of the boundary layer (Fig. 3.4) in which the trajectories of the closed-loop system move after the reaching phase ends. The larger k_σ is, the smaller the boundary layer and thus the tracking accuracy improves, as stated in Theorem 3.2. On the other hand, the larger k_σ is, the higher the risk of chattering because the slope of the *tanh* function is higher. In this work, the value of k_σ was found by iteration through the numerical simulations. Nevertheless, the dimension of the boundary layer can be found as follows:

Proposition 3.1. *The trajectories of system (3.40), (3.41), (3.44), (3.50) are proved to converge in finite time to the set*

$$\mathfrak{B}_{th\sigma} = \left\{ (q_{v,i}, \omega_i) \in \mathbb{R}^2,\ |\sigma_i| \leq \frac{1}{k_\sigma} arctanh\left(\frac{\overline{d}}{k}\right) \right\} \tag{3.51}$$

Proof. of Proposition 3.1
Take a quadratic Lyapunov function $V = \sigma_i^2$ as in (3.45), whose time derivative is computed as in Eqs. (3.46)-(3.48). Introducing the control law (3.50) into (3.48), the following is obtained:

$$\dot{V} = 2\sigma_i \left(-k \tanh(k_\sigma \sigma_i) + d_i\right), \tag{3.52}$$

where $\sigma_i \tanh(k_\sigma \sigma_i) = \tanh(k_\sigma |\sigma_i|)$ is used to obtain:

$$\begin{aligned} \dot{V} &= -2k \tanh(k_\sigma |\sigma_i|) + 2\sigma_i d_i \leq \\ &\leq -2\left(k \tanh(k_\sigma |\sigma_i|) - \overline{d}\right) |\sigma_i| = -2\left(k \tanh(k_\sigma |\sigma_i|) - \overline{d}\right) \sqrt{V_{\sigma_{0_i}}} \end{aligned} \tag{3.53}$$

and observing the term in brackets we have that

$$k \tanh(k_\sigma |\sigma_i|) - \overline{d} > 0 \quad \Leftrightarrow \quad \forall \sigma_i : \ |\sigma_i| > \frac{1}{k_\sigma} \operatorname{arctanh}\left(\frac{\overline{d}}{k}\right) \tag{3.54}$$

implying that condition (3.7) is verified for each

$$V > \left(\frac{1}{k_\sigma} \operatorname{arctanh}\left(\frac{\overline{d}}{k}\right)\right)^2. \tag{3.55}$$

Therefore Lemma 3.1 applies for $z = (q_{v,i}, \omega_i) \in \mathbb{R}^2$, $y = \sigma_i$, $\alpha = 2\left(k \tanh(k_\sigma |\sigma_i|) - \overline{d}\right)$, $\beta = 1/2$, and $\overline{y} = \frac{1}{k_\sigma} \operatorname{arctanh}\left(\frac{\overline{d}}{k}\right)$ and the proof is complete. □

Attitude control with STW algorithm

In order to design the STW control law, the σ_i-dynamics must be given in the same format as the Eq. (3.35). From the time derivative of σ_i in Eq. (3.47) it is obtained that:

$$m_i = d_i + \frac{1}{2} J_{ii} \lambda \omega_i, \quad n_i = 1 \tag{3.56}$$

Then, the design of STW algorithm requires the definition of some positive constants that depend on m_i, n_i, and the time-derivatives according to Eq. (3.37). Since in this case $m_i = m_i(\omega_i)$, it was decided to derive an upper limit for ω_i using conservation of angular momentum. In fact, due to the assumptions made about the null initial velocity of the satellite and reaction wheels and the exchange of angular momentum between them during the manoeuvre, as described in Chapter 2, it is:

$$J_{ii} |\omega_i| = |h_{rw,i}| \tag{3.57}$$

therefore, an upper bound of the angular rate $\overline{\omega}_i$ is found by imposing the avoidance of saturation of angular momentum of the reaction wheels:

$$J_{ii}\,|\omega_i| = |h_{rw,i}| \leq \overline{h_{rw}} \quad \Leftrightarrow \quad |\omega_i| \leq \overline{\omega}_i = \frac{\overline{h_{rw}}}{J_{ii}}. \tag{3.58}$$

Of course, due to the accumulation of angular momentum into the wheel to counteract the external disturbance, (3.58) should be modified so that manoeuvring the satellite requires only a fraction of the total angular momentum available as follows:

$$\overline{\omega}_i = \upsilon \frac{\overline{h_{rw}}}{J_{ii}}, \quad 0 < \upsilon < 1. \tag{3.59}$$

Also given $|d_i| \leq \overline{d}$, the upper bound for $|m_i|$ is obtained:

$$|m_i| \leq |d_i| + \frac{1}{2}\lambda J_{ii}\,|\omega_i| \leq \overline{m}_i = \overline{d} + \frac{1}{2} J_{ii}\lambda\,\overline{\omega}_i \tag{3.60}$$

After that, the time derivatives of m_i and n_i are derived from Eq. (3.56):

$$\dot{m}_i = \dot{d}_i + \frac{1}{2}\lambda J_{ii}\dot{\omega}_i, \quad \dot{n}_i = 0 \tag{3.61}$$

Then, the upper bound for $\dot{m}_i$ is derived as follows:

- $\dot{d}_i$ is the time derivative of the external torque due to orbital perturbations. As discussed in Subsection 2.2.4, the orbital disturbance torque is given by the sum of various effects, some of which produce a constant torque, while others produce a torque that varies according to position along the orbit. Therefore, the disturbance has a very small time variation, even compared to its magnitude. Thus, the upper limit of $\dot{d}_i$ is assumed to be an order of magnitude smaller than $\overline{d}$:

$$\left|\dot{d}_i\right| \leq \overline{\dot{d}} = \frac{\overline{d}}{10} \tag{3.62}$$

- $\dot{\omega}_i$ is function of both d_i and τ_i according to Eq. (3.40). It was already explained that $|d_i| \leq \overline{d}$, moreover, the torque developed by the reaction wheels is upper bounded by $\overline{\tau}$ as described in Chapter 2:

$$|\dot{\omega}_i| \leq \frac{|\tau_i| + |d_i|}{J_{ii}} \leq \overline{\dot{\omega}} = \frac{\overline{\tau} + \overline{d}}{J_{ii}} \tag{3.63}$$

Finally, combining Eqs. (3.61), (3.62), and (3.63) gives:

$$|\dot{m}_i| \leq \left|\dot{d}_i\right| + \frac{1}{2}\lambda J_{ii}\left|\dot{\omega}_i\right| \leq \overline{\dot{m}}_i = \overline{\dot{d}} + \frac{1}{2}J_{ii}\lambda\,\overline{\dot{\omega}} \tag{3.64}$$

At this point, the strategy to tune the control gains (Eqs. 3.37, 3.39) of the STW control law (3.38a) is as follows:

1. Since $0 < q < 1$, it is selected $q = \frac{1}{2}$;
2. from $\left|\frac{m}{n}\right| \leq q$ it is obtained $U_{M,i} = \frac{\overline{m}_i}{n \cdot q}$;
3. from $|\dot{m}| + U_M\,|\dot{n}| \leq C$ it is obtained $C_i = \overline{\dot{m}}_i$;
4. Since $0 \leq K_m \leq n \leq K_M$, it is selected $K_{m,i} = K_{M,i} = n_i$;
5. finally, η_i and γ_i are selected according to Eq. (3.39) in order to guarantee the finite time convergence of the closed-loop system on the sliding surface with the control law (3.38).

In STW algorithm, apart from λ, there are seven gains to be tuned for which an upper limit must be found on ω_i, $\dot{\omega}_i$, and $\dot{d}_i$.

Case of study

In this work two different SMC algorithms are compared:

- BLFOSM, with the control law in Eq. (3.50);
- STW, in which the control law is taken from Eq. (3.38) and it is:

$$\tau_i = \tau_{1,i} + \tau_{2,i} \tag{3.65a}$$

$$\tau_{1,i} = -\gamma_i\,|\sigma_i|^{\frac{1}{2}}\,\mathrm{sign}(\sigma_i) \tag{3.65b}$$

$$\dot{\tau}_{2,i} = \begin{cases} -\tau_i & \text{if} \quad |\tau_i| > U_{M,i} \\ -\eta_i \cdot \mathrm{sign}(\sigma_i) & \text{if} \quad |\tau_i| \leq U_{M,i} \end{cases} \tag{3.65c}$$

The control laws (3.50) and (3.65) are applied to the dynamics system (2.26), (2.37), and (2.38) to simulate an inertial pointing maneuver. Furthermore, the numerical

simulations are performed at two different values of update frequency, a smaller one to account for the hardware limitations of the real controller and a larger one to approach the ideal SMC that requires an infinite update frequency. The numerical simulations are carried out in Matlab/Simulink for the same initial conditions in order to compare the performance of the two control laws listed above with both high and low update frequency values and to assess the impact of the update frequency value on the performance developed by each controller. The parameters of both the maneuvers and the controllers are listed in Section 5.1, where the most relevant results are also shown.

Discussion of the results

This preliminary work was useful for comparing the BLFOSM and STW algorithms in terms of several factors, such as chattering elimination, tracking accuracy, ease of tuning, and their behaviour with regard to hardware constraints. This allowed the following to be observed:

- Tuning the BLFOSM controller is much simpler than tuning the STW controller, both in terms of the number of parameters to be set and their level of intuitiveness. In fact, in addition to λ, in the BLFOSM only two parameters need to be set, i.e. k and k_σ. Since k is closely related to the torque required by the reaction wheels, it is also straightforward to tune the BLFOSM so that torque saturation is avoided. Also k_σ has an intuitive meaning, as it directly gives the dimension of the boundary layer. On the other hand, tuning the STW entails setting 7 parameters, requiring the manipulation of the σ-dynamics and deriving upper bounds on ω, $\dot{\omega}$, and $\dot{d}$. Moreover, the correlation between these parameters and the torque computed by the STW control law is not as direct as in the BLFOSM.

- The BLFOSM algorithm allows to preserve the ease of tuning of FOSM while avoiding chattering even when the controller is operating at a low refresh rate. In fact, the BLFOSM does not seem to be affected by the refresh rate, developing similar performance whether working at a high or low frequency. On the other hand, the STW has been shown to be affected by the refresh rate, offering better performance at 1000 Hz than at 10 Hz. Despite the better pointing accuracy shown by the STW, it was decided to focus the next steps of

the research on the BLFOSM due to its easy of implementation and tuning, as well as the fact that it is not affected by the refresh rate. Furthermore, the BLFOSM appears to be less computationally expensive than the STW, whose control law includes more mathematical operations involving numerical integration. In fact, numerical simulations performed with BLFOSM were faster than those performed with STW.

- In the BLFOSM, it is straightforward to prevent torque saturation by setting control gain k to be less than the maximum torque that can be developed by the electric motor. However, no mathematical relationship has been established to fix k so that torque saturation is avoided for certain. Moreover, this is not enough to ensure that the angular momentum of the wheels does not saturate during the maneuver, as was sometimes found in numerical simulations. In particular, saturation was found in the initial stages of the control process, i.e. during the reaching phase. For this reason, the next step of the research is to study the reaching phase, looking for mathematical rules to set the control parameters so as to avoid saturation of the angular momentum.

3.3.2 BLFOSM design including actuators constraints

This work focuses on the design of BLFOSM algorithm for attitude control systems of spacecraft subject to actuators constraints. The control objective is to perform an attitude maneuver for inertial pointing, and the same assumptions listed in subsection 3.3.1 are assumed. Thus, the actuation system consist of reaction wheels, and the objective is to design the control algorithm in order to avoid saturation of the wheels during the manoeuvre. In particular, the control law must ensure that:

i. the control input τ does not exceed the maximum torque $\overline{\tau}$ that can be supplied by the brushless electric motors;

ii. the angular momentum stored into the wheels h_{rw} does not exceed the maximum angular momentum they can store $\overline{h_{\text{rw}}}$.

In particular, the angular momentum stored into the wheels is closely related to the angular rate of the spacecraft during the maneuver, as explained in Chapter 2. Therefore, the saturation of the actuation system may arise if the maneuver is

performed at high angular speeds.
BLFOSM is the control algorithm aimed at the realisation of the objective proposed in this work. As briefly introduced in Section 3.1, the SMC process can be split into two time stages: first, the system's trajectories reach the sliding surface during the reaching phase, and then the trajectories moves on the sliding surface during sliding phase. Therefore, during sliding phase the closed-loop system follows the dynamics prescribed by the sliding surface, but during reaching phase the trajectories move outside the sliding surface, so the states of the system are unconstrained. As a consequence, the angular rates of the spacecraft may exceed the threshold during this stage, leading to saturation of the actuators. Starting from the BLFOSM control law (Eq. 3.50), the behaviour of the dynamic system (3.40) during reaching phase is investigated, deriving a mathematical relation between the time-evolution of the sliding variable and the angular rate over this stage. After that, a novel strategy is used to define the control parameters of the BLFOSM algorithm. Taking into account both the saturation values of the actuators and the spacecraft parameters, this strategy successfully avoid the saturation problem.

Tuning with compliance of actuator constraints

The same assumptions listed in subsecion 3.3.1 are assumed, thus the control problem is reduced to manage a second-order dynamic system for each axis of the spacecraft. Similar to Eq. (3.41), here the sliding variable is selected as follows:

$$\sigma_i = J_{ii}\left(\omega_i + \lambda q_{v,i}\right), \quad \lambda \in \mathbb{R}^+, \quad i = x,y,z \tag{3.66}$$

with J_{ii} the inertia of the spacecraft about the i-axis and λ the inclination of the sliding surface for the i-axis. Keeping in mind Eq. (3.40), the sliding variable can also be presented as follows:

$$\sigma_i = \left(\frac{d}{dt} + \frac{\lambda}{2}\right) 2J_{ii} q_{v,i} \tag{3.67}$$

and its time derivative is given by:

$$\dot{\sigma}_i = \left(\frac{d}{dt} + \frac{\lambda}{2}\right) 2J_{ii}\dot{q}_{v,i} = \left(\frac{d}{dt} + \frac{\lambda}{2}\right) J_{ii}\omega_i \tag{3.68}$$

therefore $J_{ii}\omega_i$ is obtained as the output of a first-order linear filter fed with $\dot{\sigma}_i$. Furthermore, from the assumptions it is $\omega_i(t=0)=0$ at the start of the control process, thus the output of first order filter is bounded as follows during reaching phase:

$$J_{ii}\,|\omega_i| < \frac{|\dot{\sigma}_i|}{\lambda/2} \tag{3.69}$$

Thus, in order to avoid the saturation of the angular momentum it should be:

$$J_{ii}\,|\omega_i| < \frac{|\dot{\sigma}_i|}{\lambda/2} \leq \overline{h_{\mathrm{rw}}} \tag{3.70}$$

Now, an upper bound for $|\dot{\sigma}|$ is derived from the σ-dynamics, i.e. from the derivative of Eq. (3.66):

$$\dot{\sigma}_i = J_{ii}\,(\dot{\omega}_i + \lambda\,\dot{q}_{v,i}) \tag{3.71}$$

Introducing both the dynamic system (3.40) and the control law (3.50), $\dot{\sigma}_i$ becomes as follows:

$$\dot{\sigma}_i = \tau_i + d_i + \frac{1}{2}J_{ii}\lambda\,\omega_i = -k\,\tanh\left(k_\sigma\sigma_i\right) + d_i \tag{3.72}$$

and the upper bound can be found with the triangle inequality:

$$|\dot{\sigma}_i| \leq |k\,\tanh(k_\sigma\sigma_i)| + |d_i| < k + \overline{d} \tag{3.73}$$

with $\overline{d}$ the upper bound of the external torque as in Eq. (3.44). Introducing Eq. (3.73) into Eq. (3.70), the following condition on λ is found to prevent actuator saturation:

$$\frac{|\dot{\sigma}_i|}{\lambda/2} < \frac{k+\overline{d}}{\lambda/2} \leq \overline{h_{\mathrm{rw}}} \quad \Rightarrow \quad \lambda \geq \frac{k+\overline{d}}{\overline{h_{\mathrm{rw}}}/2} \tag{3.74}$$

To compute λ, the gain k should be established. As briefly mentioned above, this gain is defined without saturation of the wheel torque, i.e. $|\tau_i| \leq \overline{\tau}$. From the control law (3.50), the triangle inequality, and Eq. (3.69) we have:

$$|\tau_i| \leq |k \tanh(k_\sigma \sigma_i)| + \left|\frac{1}{2} J_{ii} \lambda \omega_i\right| < k + \frac{1}{2}\lambda \overline{h_{\text{rw}}} \leq \overline{\tau} \tag{3.75}$$

Introducing Eq. (3.74) into equation above, the following condition on k is found to avoid torque saturation:

$$k + \frac{\overline{h_{\text{rw}}}}{2} \frac{k + \overline{d}}{\overline{h_{\text{rw}}}/2} \leq \overline{\tau} \quad \Rightarrow \quad k \leq \frac{\overline{\tau} - \overline{d}}{2} \tag{3.76}$$

From Eqs. (3.44) and (3.76) we obtain two bounds regarding the control gain k:

$$\begin{cases} k \leq \frac{\overline{\tau} - \overline{d}}{2} \\ k > \overline{d} \end{cases} \tag{3.77}$$

The first one comes out from the condition to avoid the saturation on the torque, while the second one derives from the reachability condition. This system leads to a constraint on the choice of the actuators. In fact, they must provide a maximum torque given by

$$\overline{\tau} > 3\overline{d} \tag{3.78}$$

in order to satisfy both the conditions in system (3.77). Finally, for each spacecraft axis the controller is defined by the control law (3.50) with the gains as in Eqs. (3.74) and (3.76).

Case of study

The control law (3.50), with the control parameters as in Eqs. (3.74) and (3.76) is applied to the same scenario that was used for numerical simulations of subsection 3.3.1. Therefore, the dynamics system used for simulations is given by (2.26), (2.37), and (2.38), and same spacecraft, actuation system, and initial conditions of subsection 3.3.1 are taken into account. Next, the results are compared with those obtained in Section 5.1 using the same control law (3.50), but with gains as in Table

5.2. The parameters of the numerical simulations are listed in Section 5.2, where the most relevant results are also shown.

Discussion of the results

The purpose of this work was to define a strategy to derive the control parameters of BLFOSM control law to avoid saturation of the reaction wheels during the maneuver. Therefore, the output of the control law defined in this paper can be realised by actuators of a real system, in contrast to the control law with the same structure used in subsection 3.3.1. The key feature of the proposed approach is to upper bound the angular rate when the system is in reaching phase, constraining the system's trajectories so that saturation of angular momentum does not occur. The results showed the effectiveness of the proposed approach to avoid actuator saturation whilst completing the manoeuvre. However, the analysis of the results revealed the following issues:

- The stability of the closed-loop system was proven under the condition that the inertia matrix of the satellite is known. In fact, J_{ii} appears in the equivalent control (Eq. 3.50) in order to compensate the same term in the σ_i-dynamics (Eq. 3.40), with the latter coming from the dynamics. Therefore, if the true inertia is different from the supposed one, this term can not be fully compensated, and the mismatch must be taken into account when studying the stability of the closed-loop system.
- The inertia matrix enters into the procedure to derive the control gains k and λ. In this study, we assumed the inertia matrix to be known and that the satellite is a rigid body, but the parametric uncertainties and the flexibility of the structures need to be considered for a more realistic study.

Therefore, the design of a BLFOSM algorithm for an inertial pointing manoeuvre is studied in the next subsection, using a mathematical model that includes parametric uncertainties and flexibility of structures in the satellite attitude dynamics.

3.3.3 BLFOSM design including parametric uncertainties

This work describes the derivation of a BLFOSM algorithm to manipulate the attitude dynamics of the flexible spacecraft with uncertain parameters. The objective is to perform an inertial pointing maneuver without saturating the actuators as in Subsection 3.3.2. However, in this case the design of the controller includes the uncertainties of inertia and coupling between attitude dynamics and flexible dynamics.

Tuning with parametric uncertainties

The same assumptions listed in subsection 3.3.1 are considered, except that the satellite is no longer considered as a rigid body. Nevertheless, the satellite is still assumed with three principal axes of inertia, but the true inertia J is unknown. However, we considered that J consists of J_0, i.e. the known nominal inertia, and ΔJ, which includes uncertainties and possible parametric variations. Therefore, we have $J = J_0 + \Delta J$, and the mathematical model used for control design consists of three SISO systems plus the dynamics equation of the amplitude η as follows (details in Chapter 2):

$$\begin{cases} \dot{q}_{v,i} = \dfrac{1}{2}\omega_i \\ \dot{\omega}_i = \left(\dfrac{1}{J_{0_{ii}}} + \hat{\Delta J}_{ii}\right)\left(\tau_i + d_i - (\delta^T \ddot{\eta})_i\right) \\ \ddot{\eta} = -C\dot{\eta} - K\eta - \delta\dot{\omega} \end{cases} \qquad i = x,y,z \tag{3.79}$$

For this work, we assumed $\Delta J > 0$ unknown, but with a known upper bound $\overline{J}$, which allows to define a parameter ξ such that

$$J_{ii} \leq \overline{J}_{ii} = \xi_i J_{0_{ii}}. \tag{3.80}$$

Furthermore, this assumption also allows an upper limit to be defined for $\hat{\Delta J}$, that is

$$\left|\hat{\Delta J}_{ii}\right| \leq \overline{\hat{\Delta J}}_{ii}, \tag{3.81}$$

with $\overline{\hat{\Delta J}}_{ii}$ obtained by injecting $\overline{\Delta J}_{ii} = \overline{J}_{ii} - J_{0_{ii}}$ into the Matrix Inversion Lemma (2.50). As discussed in Chapter 2, the flexibility of the appendages adds a further

input to the total angular momentum of the system, so we have

$$H_i = J_{ii}\omega_i + h_{\mathrm{rw}_i} + (\delta^T \dot{\eta})_i, \tag{3.82}$$

and bearing in mind the conservation of angular momentum and the null initial angular velocity of both the satellite and the wheels, the angular momentum stored into the actuators is

$$h_{\mathrm{rw}_i} = -J_{ii}\omega_i - (\delta^T \dot{\eta})_i, \tag{3.83}$$

to which the triangle inequality is applied and the condition for not saturating the wheels is imposed, obtaining

$$|h_{\mathrm{rw}_i}| \leq J_{ii}\,|\omega_i| + \left|\delta^T \dot{\eta}\right|_i \leq \overline{h_{\mathrm{rw}}} \tag{3.84}$$

Since the deformations due to the flexibility of the appendages are typically small, it is reasonable to consider the contribution of the flexibility to the angular momentum neglactable during a maneuver, i.e. $J_{ii}\,|\omega_i| >> \left|\delta^T \dot{\eta}\right|_i$. Furthermore, for the assumptions it is $J_{ii} \leq \overline{J}_{ii}$, therefore the condition to prevent saturation of the angular momentum in the wheels can be written as

$$\overline{J}_{ii}\,|\omega_i| < \overline{h_{\mathrm{rw}}} \quad \rightarrow \quad \max|\omega_i| = \overline{\omega}_i = \frac{\overline{h_{\mathrm{rw}}}}{\xi_i J_{0_{ii}}} \tag{3.85}$$

with $\overline{\omega}_i$ the maximum angular rate for which the wheels do not saturate. Similar to Subsection 3.3.2, we need to find an upper bound for the angular rate of the spacecraft during reaching phase, therefore we derive a mathematical relation between the time-evolution of the sliding variable and the angular rate over this stage. First, both the sliding variable and the control law are defined using the nominal value of the inertia as follows

$$\sigma_i = J_{0_{ii}}\,(\omega_i + \lambda_i q_{v,i}) = \left(\frac{d}{dt} + \frac{\lambda_i}{2}\right) 2J_{0_{ii}} q_{v,i}, \quad \lambda_i \in \mathbb{R}^+, \tag{3.86}$$

$$\tau_i = -k_i\,\mathrm{sat}(\sigma_i) - \frac{1}{2} J_{0_{ii}} \lambda_i \omega_i. \tag{3.87}$$

Eq. (3.86) allows to define an upper bound for $J_{0_{ii}}|\omega|$ as in (3.68), (3.69). Indeed, we have

$$\dot{\sigma}_i = \left(\frac{d}{dt} + \frac{\lambda_i}{2}\right) J_{0_{ii}}\omega_i \quad \rightarrow \quad J_{0_{ii}}|\omega_i| < \frac{|\dot{\sigma}_i|}{\lambda_i/2}. \tag{3.88}$$

Multiplying both sides of inequality (3.88) by ξ_i defined as in (3.80) we obtain as follows:

$$\xi_i J_{0_{ii}} |\omega_i| = \overline{J}_{ii} |\omega_i| < \xi_i \frac{|\dot{\sigma}_i|}{\lambda_i / 2}, \tag{3.89}$$

and combining (3.85) with (3.89), the condition to prevent angular momentum of the wheels from saturation results in:

$$\xi_i \frac{|\dot{\sigma}_i|}{\lambda_i / 2} \leq \overline{h}_{\text{rw}}, \tag{3.90}$$

which is similar to Eqs. (3.69), (3.70). Now, an upper bound for $|\dot{\sigma}|$ is derived by introducing the closed-loop dynamics equations into the derivative of the sliding variable (3.86), which is:

$$\dot{\sigma} = J_{0_{ii}} \left(\dot{\omega}_i + \lambda_i \dot{q}_{v,i} \right). \tag{3.91}$$

Eq. (3.79) is inserted into equation above to obtain:

$$\dot{\sigma} = J_{0_{ii}} \left[\left(\frac{1}{J_{0_{ii}}} + \hat{\Delta} J_{ii} \right) \left(\tau_i + d_i - (\delta^T \ddot{\eta})_i \right) + \frac{1}{2} \lambda_i \omega_i \right] = \tag{3.92}$$

$$= \left(1 + J_{0_{ii}} \hat{\Delta} J_{ii} \right) \left(\tau_i + d_i - (\delta^T \ddot{\eta})_i \right) + \frac{1}{2} J_{0_{ii}} \lambda_i \omega_i, \tag{3.93}$$

and introducing the control law (3.87), the latter becomes:

$$\dot{\sigma} = \left(1 + J_{0_{ii}} \hat{\Delta} J_{ii} \right) \left(-k_i \, \text{sat}(\sigma_i) - \frac{1}{2} J_{0_{ii}} \lambda_i \omega_i + d_i - (\delta^T \ddot{\eta})_i \right) + \frac{1}{2} J_{0_{ii}} \lambda_i \omega_i = \tag{3.94}$$

$$= \left(1 + J_{0_{ii}} \hat{\Delta} J_{ii} \right) \left(-k_i \, \text{sat}(\sigma_i) + d_i - (\delta^T \ddot{\eta})_i \right) - \left(1 + J_{0_{ii}} \hat{\Delta} J_{ii} - 1 \right) \frac{1}{2} J_{0_{ii}} \lambda_i \omega_i = \tag{3.95}$$

$$= \left(1 + J_{0_{ii}} \hat{\Delta} J_{ii} \right) \left(-k_i \, \text{sat}(\sigma_i) + d_i - (\delta^T \ddot{\eta})_i \right) - J_{0_{ii}}^2 \hat{\Delta} J_{ii} \lambda_i \omega_i \tag{3.96}$$

The disturbance torque due to flexibility has an upper bound which can be estimated through structural analysis and simulations. Having already defined the upper bound of the external torque $|d_i| < \overline{d}$ (3.44), we can establish the upper bound μ of the total disturbance as:

$$\overline{d} + \|\delta^T \ddot{\eta}\|_\infty < \mu. \tag{3.97}$$

Therefore, bearing in mind Eqs. (3.81) and (3.85), the upper bound of (3.96) is as follows:

$$|\dot{\sigma}_i| \leq \left(1 + J_{0_{ii}}\overline{\hat{\Delta}J}_{ii}\right)(k_i + \mu) + J_{0_{ii}}^2 \overline{\hat{\Delta}J}_{ii}\lambda_i\overline{\omega}_i \tag{3.98}$$

Now, Eqs. (3.85) and (3.98) are inserted into Eq. (3.90) to obtain the λ_i value guaranteeing the avoidance of angular momentum saturation:

$$\begin{aligned} &\overline{h_{\text{rw}}} \geq \xi_i \frac{|\dot{\sigma}_i|}{\lambda_i} \geq \frac{\xi_i}{\lambda_i}\left(1 + J_{0_{ii}}\overline{\hat{\Delta}J}_{ii}\right)(k_i + \mu) + \xi_i J_{0_{ii}}^2 \overline{\hat{\Delta}J}_{ii}\overline{\omega} \\ &\Downarrow \\ &\lambda_i \geq \frac{\xi_i\left(1 + J_{0_{ii}}\overline{\hat{\Delta}J}_{ii}\right)(k_i + \mu)}{\overline{h_{\text{rw}}} - \xi_i J_{0_{ii}}^2 \overline{\hat{\Delta}J}_{ii}\frac{\overline{h_{\text{rw}}}}{\xi_i J_{0_{ii}}}} = \frac{\xi_i\left(1 + J_{0_{ii}}\overline{\hat{\Delta}J}_{ii}\right)(k_i + \mu)}{\overline{h_{\text{rw}}}\left(1 - J_{0_{ii}}\overline{\hat{\Delta}J}_{ii}\right)}. \end{aligned} \tag{3.99}$$

Similar to Subsection 3.3.2, the gain k_i is defined without torque saturation. Therefore, the triangle inequality is applied to the control law (3.87) as follows:

$$|\tau_i| \leq k_i + J_{0_{ii}}\lambda_i\overline{\omega}_i \leq \overline{\tau} \quad \Rightarrow \quad k_i \leq \overline{\tau} - J_{0_{ii}}\lambda_i\overline{\omega}_i \tag{3.100}$$

and inserting λ_i (3.85) and $\overline{\omega}_i$ (3.99) into equation above we obtain:

$$k_i \leq \overline{\tau} - J_{0_{ii}}\frac{\xi_i\left(1 + J_{0_{ii}}\overline{\hat{\Delta}J}_{ii}\right)(k_i + \mu)}{\overline{h_{\text{rw}}}\left(1 - J_{0_{ii}}\overline{\hat{\Delta}J}_{ii}\right)}\frac{\overline{h_{\text{rw}}}}{\xi_i J_{0_{ii}}} = \overline{\tau} - \frac{1 + J_{0_{ii}}\overline{\hat{\Delta}J}_{ii}}{1 - J_{0_{ii}}\overline{\hat{\Delta}J}_{ii}}(k_i + \mu). \tag{3.101}$$

By manipulating equation above, the k_i value avoiding torque saturation is found as follows:

$$k_i\left(1+\frac{1+J_{0_{ii}}\overline{\hat{\Delta J}}_{ii}}{1-J_{0_{ii}}\overline{\hat{\Delta J}}_{ii}}\right)\leq\overline{\tau}-\mu\frac{1+J_{0_{ii}}\overline{\hat{\Delta J}}_{ii}}{1-J_{0_{ii}}\overline{\hat{\Delta J}}_{ii}}\quad\Rightarrow\quad k_i\leq\frac{\overline{\tau}-\mu\frac{1+J_{0_{ii}}\overline{\hat{\Delta J}}_{ii}}{1-J_{0_{ii}}\overline{\hat{\Delta J}}_{ii}}}{1+\frac{1+J_{0_{ii}}\overline{\hat{\Delta J}}_{ii}}{1-J_{0_{ii}}\overline{\hat{\Delta J}}_{ii}}}\tag{3.102}$$

Therefore, λ_i and k_i are obtained with the last of (3.99) and (3.102), respectively.

Closed-loop stability

In this work, the discontinuity of the signum function in the control law is smoothed out with the saturation function, which directly gives the dimension of the boundary layer through the parameter $\overline{\sigma}$ as discussed in Subsection 3.2.2. Contrary to what has been seen so far in this chapter, the mathematical model contains parametric uncertainties that require proving again the finite-time stability of the boundary layer. The latter is discussed below.

Proposition 3.2. *The system (3.79), (3.86), (3.87) is proved to converge in finite time to the following set*

$$\mathfrak{B}_{\overline{\sigma}}=\left\{(q_{v,i},\omega_i)\in\mathbb{R}^2,\ |\sigma_i|\leq\overline{\sigma}\right\}\tag{3.103}$$

if $k_i>\mu$ *for* $i=x,y,z$.

Proof. of Proposition 3.2
The Proof is based on Lemma 3.1. Therefore, consider the quadratic Lyapunov function $V=\sigma^2$ as in (3.45), whose time derivative is $\dot{V}=2\sigma\dot{\sigma}$. Introducing $\dot{\sigma}$ as in (3.96) in the time derivative of the candidate Lyapunov function we obtain:

$$\dot{V}=2\sigma_i\left(1+J_{0_{ii}}\hat{\Delta J}_{ii}\right)\left(-k_i\ \mathrm{sat}(\sigma_i)+d_i-(\delta^T\ddot{\eta})_i\right)-2\sigma_i J_{0_{ii}}^2\hat{\Delta J}_{ii}\lambda_i\omega_i.\tag{3.104}$$

Now, observe that $\sigma_i\cdot\mathrm{sat}(\sigma_i)=|\sigma_i|\ \forall|\sigma_i|>\overline{\sigma}$. Furthermore, using μ defined as in (3.97) and $\overline{\hat{\Delta J}}$ as in (3.81) gives:

$$2\sigma_i\left(1+J_{0_{ii}}\hat{\Delta J}_{ii}\right)\left(-k_i\ \mathrm{sat}(\sigma_i)+d_i-(\delta^T\ddot{\eta})_i\right)\leq 2\left(1+J_{0_{ii}}\overline{\hat{\Delta J}}_{ii}\right)\left(-k_i|\sigma_i|+\mu|\sigma_i|\right),\tag{3.105}$$

and since the control gains (3.99), (3.102) ensure the fulfillment of condition (3.85), we also have:

$$2\sigma_i J_{0_{ii}}^2 \hat{\Delta J}_{ii} \lambda_i \omega_i \leq 2|\sigma_i| J_{0_{ii}}^2 \overline{\hat{\Delta J}}_{ii} \lambda_i \overline{\omega}_i. \tag{3.106}$$

Therefore, inserting (3.105) and (3.106) into (3.104) gives:

$$\dot{V} \leq 2\left(1 + J_{0_{ii}} \overline{\hat{\Delta J}}_{ii}\right)\left(-k_i|\sigma_i| + \mu|\sigma_i|\right) + 2|\sigma_i| J_{0_{ii}}^2 \overline{\hat{\Delta J}}_{ii} \lambda_i \overline{\omega}_i \tag{3.107}$$

Substituting $\overline{\omega}_i$ from (3.85) and λ_i from (3.99) we get:

$$2|\sigma_i| J_{0_{ii}}^2 \overline{\hat{\Delta J}}_{ii} \lambda_i \overline{\omega}_i = 2|\sigma_i| J_{0_{ii}}^2 \overline{\hat{\Delta J}}_{ii} \frac{\xi_i \left(1 + J_{0_{ii}} \overline{\hat{\Delta J}}_{ii}\right)(k_i + \mu)}{\overline{h_{\text{rw}}}\left(1 - J_{0_{ii}} \overline{\hat{\Delta J}}_{ii}\right)} \frac{\overline{h_{\text{rw}}}}{\xi_i J_{0_{ii}}} = \tag{3.108}$$

$$= 2|\sigma_i| J_{0_{ii}} \overline{\hat{\Delta J}}_{ii} (k_i + \mu) \frac{1 + J_{0_{ii}} \overline{\hat{\Delta J}}_{ii}}{1 - J_{0_{ii}} \overline{\hat{\Delta J}}_{ii}}, \tag{3.109}$$

and inserting (3.109) into (3.107) we obtain:

$$\begin{aligned} \dot{V} \leq & -2k_i|\sigma_i| \left[1 + J_{0_{ii}} \overline{\hat{\Delta J}}_{ii} - J_{0_{ii}} \overline{\hat{\Delta J}}_{ii} \frac{1 + J_{0_{ii}} \overline{\hat{\Delta J}}_{ii}}{1 - J_{0_{ii}} \overline{\hat{\Delta J}}_{ii}}\right] + \\ & + 2\mu|\sigma_i| \left[1 + J_{0_{ii}} \overline{\hat{\Delta J}}_{ii} + J_{0_{ii}} \overline{\hat{\Delta J}}_{ii} \frac{1 + J_{0_{ii}} \overline{\hat{\Delta J}}_{ii}}{1 - J_{0_{ii}} \overline{\hat{\Delta J}}_{ii}}\right]. \end{aligned} \tag{3.110}$$

Factoring out the denominator in the equation above, we obtain:

$$\dot{V} \leq -\frac{2}{1 - J_{0_{ii}} \overline{\hat{\Delta J}}_{ii}} \left[k_i \left(1 - J_{0_{ii}} \overline{\hat{\Delta J}}_{ii} - 2\left(J_{0_{ii}} \overline{\hat{\Delta J}}_{ii}\right)^2\right) - \mu\left(1 + J_{0_{ii}} \overline{\hat{\Delta J}}_{ii}\right)\right] |\sigma_i|, \tag{3.111}$$

in which the terms in brackets is:

$$k_i \left(1 - J_{0_{ii}} \overline{\hat{\Delta J}}_{ii} - 2\left(J_{0_{ii}} \overline{\hat{\Delta J}}_{ii}\right)^2\right) - \mu\left(1 + J_{0_{ii}} \overline{\hat{\Delta J}}_{ii}\right) > 0 \quad \forall\, k_i > \mu,\ \Delta J \geq 0 \tag{3.112}$$

because $J_{0_{ii}}\overline{\hat{\Delta J}}_{ii} \in (-1,0]$ since $J_{0_{ii}}\overline{\hat{\Delta J}}_{ii} = 0$ for $\Delta J = 0$ and $J_{0_{ii}}\overline{\hat{\Delta J}}_{ii} \to -1$ for $\Delta J \to \infty$). Therefore, condition (3.7) is verified for each $V > \overline{\sigma}^2$. Therefore, Lemma 3.1 applies for $z = (q_{v,i}, \omega_i) \in \mathbb{R}^2$, $y = \sigma_i$, α in Eq. (3.112), $\beta = 1/2$, and $\bar{y} = \overline{\sigma}$ and the proof is complete. □

Case of study

The control law (3.87) with the control gains (3.99), (3.102) is applied to the dynamic system (2.26), (2.68), (2.64) and (2.38) to simulate an inertial pointing maneuver. The flexible satellite used for numerical simulations is modeled according to Subsection 2.2.3, and is described in Appendix A. The flexibility of the panels is accounted as described in Subsection 2.2.3, obtaining K, C, and δ in (3.79) from the FEM analysis. For numerical simulations purposes, the nominal inertia J_0 is taken with folded panels, while the upper bound $\overline{J}$ is computed with deployed panels. The maneuver and the parameters of the both the spacecraft and the controller are listed in Section 5.2, where the most relevant results are also shown.

Discussion of the results

In this work, the results obtained in Section 3.3.2 for the rigid satellite with known parameters were extended to the flexible satellite with uncertain parameters. The controller design is similar to that seen in Section 3.3.2, but in this case uncertainties about inertia enter into the definition of control gains λ_i and k_i. In particular, in the case where $\Delta J = 0$ is considered, (3.99) and (3.102) reduce to (3.74) and (3.76), respectively. The gain k_i is affected by two constraints, that are (3.102) and $k > \mu$ from (3.112). Then, the right side of (3.102) has its minimum for $J_{0_{ii}}\overline{\hat{\Delta J}}_{ii} = 0$, which gives

$$k_i \leq \frac{\overline{\tau} - \mu}{2}. \tag{3.113}$$

This inequality, together with $k_i > \mu$ leads to a constraint on the choice of the actuators, which must provide a maximum torque which is at least

$$\overline{\tau} > 3\mu. \tag{3.114}$$

The results of the numerical simulations showed the effectiveness of the proposed approach to avoid actuator saturation whilst completing the manoeuvre for the

flexible spacecraft with uncertain parameters. However, the analysis of the results revealed the following issue

- The proposed approach requires the angular velocity of the spacecraft to be zero at the starting time, otherwise the Eq. (3.69) is not valid, negating the rest of the approach.
- The fulfillment of the reachability condition requires the nominal inertia J_0 to be the minimum inertia assumed by the satellite. Indeed, the inequality (3.112) is proven to be true for each $k_i > \mu$ only where $\Delta J \geq 0$ is considered. If the true inertia of the satellite can be $J < J_0$, i.e. $\Delta J < 0$, the fulfilment of the reachability condition can still be guaranteed provided that k_i is large enough so that the inequality (3.112) is satisfied even for $\Delta J < 0$.
- The reaching phase may be very prolonged, taking the majority of the manoeuvring time depending on the initial conditions. Although the proposed approach solves the issue due to unconstrained states when the system moves outside the sliding surface, the reaching phase shows other criticalities that make it undesirable to be protracted within the control process. In fact, the critical aspect of this phase is due to the risk for trajectories to be sensitive to disturbances and parametric uncertainties, so that during reaching phase SMC loses the robustness it displays during the sliding phase [97].

Building on these considerations, a BLFOSM algorithm with an adaptive sliding surface was developed in this thesis. This algorithm is the major result of the PhD project, and will be presented in the next Chapter. Here, it will be shown how it succeeds in reducing the reaching time, while alleviating the other two issues above.

Chapter 4

Sliding mode control with adaptive sliding surface

This chapter details the adaptive mechanism developed in this PhD project to adapt in real time the sliding surface during the control process. The innovative algorithm synthesised in this thesis is based on the conventional BLFOSM, but the adaptive mechanism allows the slope of the sliding surface to be adapted, giving the new control algorithm a great ability to adapt to a wide range of initial conditions, ensuring robustness, tracking accuracy and smooth response. In Section 3.1, references were made to adaptive mechanisms used in SMC algorithms and aimed at mitigating chattering through real-time adjustment of the control gains. In contrast, in this work the adaptive mechanisms are not used for this purpose. In fact, in the new algorithm the mitigation of chattering is performed using the BLSMC approach, as detailed in Chapter 3. Therefore, in the algorithm presented in this chapter the gain k of the switching control is constant, while the parameter λ of the sliding variable is adapted in real time. The main key of this proposal is the reduction of the reaching time, so that the reaching phase is proven to be shorter than in conventional BLFOSM with fixed sliding surface. Another approach widely used in the literature to eliminate the reaching phase is the Integral SMC (ISMC), so it is worth to be mentioned here as it is relevant to the scope of this thesis, even though it is not dealt within this project. The ISMC was first proposed in [98], and it ensures the existence of the sliding motion since the beginning of the control process by introducing integrative terms in the definition of the sliding surface. In addition to eliminating the reaching phase, the ISMC approach can reduce the steady-state error and mitigate the chattering

problem; however, in the presence of a high initial error, this method could lead to large overshoot and a long settling time, thus degrading transient performance. This phenomenon becomes more severe when the control input is limited, [99].
To the best of our knowledge, there is no work in the literature regarding SMC for second-order systems in which the sliding surface is adjusted in real time using adaptive laws. However, several authors have proposed time-varying sliding surfaces according to other logics than adaptive laws, so a literature review on these works is in Section 4.1. Then, in Section 4.2 the innovative adaptive BLFOSM algorithm is introduced, presenting the adaptive law for λ and the control design for a second order system with a single input. Here, the advantages brought about by the adaptation of the sliding surface in the BLFOSM are detailed and certified through mathematical proofs. Finally, in Section 4.3 the innovative control algorithm is used to manipulate satellite attitude dynamics, taking into account the models developed in this PhD for academic research purposes and the implementation on a real satellite, i.e. the DEMETER.

4.1 Overview on sliding mode control with time-varying sliding surface

Conventional SMC with fixed sliding surface consists of reaching phase and sliding phase, and if the initial state is far from the sliding surface, the system may have an undesirable and unpredictable reaching mode. In fact, reaching phase has critical issues related to both lack of robustness and unconstrained trajectories of the system, as discussed in Chapter 3. For this reason, various techniques have been proposed to reduce the reaching time, and the first one was to increase the gain of the switching control input. However, this eventually aggravates the chattering problem and may lead to saturate the actuators [100]. Therefore, several techniques consider time-varying sliding surface through predefined mathematical rules or fuzzy logic. By reducing the distance between the sliding surface and the initial state, time-varying sliding surface ensures low reaching time while avoiding both a big control effort and fast system response for any initial conditions. Since the beginning of this new concept, time-varying sliding surfaces have been considered for a variety of dynamic systems. In the literature there can be found works concerning linear and nonlinear moving sliding surfaces for second-order systems up to systems of order n, both

continuous-time and discrete-time. A very detailed and comprehensive collection of the work developed in this field can be found in [101] and [102]. In view of the scope of application of this, only works concerning moving linear sliding surfaces for second-order continuous-time systems are reported below.
A SMC with discrete time-varying sliding surface for second order systems was first proposed in [103], where the sliding surface is first selected to pass through the initial state errors, and then it is rotated and/or shifted in a step-wise fashion until it reaches the predetermined desired position. In this work, the linear time-varying sliding surface for second order system is defined as:

$$s = \dot{e} + c \cdot e + \alpha \tag{4.1}$$

where α and c are responsible for shifting and rotating the sliding surface, respectively. These parameters are updated during the control process and kept fixed for a determined time period, i.e. the dwelling time, which is another control parameter that must be adjusted to preserve robustness. In fact, although this approach guarantees shorter reaching time, a reaching phase occurs after each dwelling period because the discontinuous movement of the sliding surface, ruining the robustness of the control system as revealed in [104]. In the same article, the author proposed a technique for continuously moving the sliding surface, defining the parameters $c(t)$ and $\alpha(t)$ in Eq. (4.1) as first degree polynomial of the time whose parameters give the rotation and shifting schemes. Subsequently, several authors have proposed practical applications for the time-varying sliding surface approach developed in [104]. Indeed, the latter is applied to position control of a DC motor in [105], and to position control of induction machines in [106], in both cases and analysis are supported by experimental results. Also paper [107] presents an application of the same scheme to move the sliding surface for the two degree of freedom robot arm position regulation. Furthermore, in this article velocity and acceleration constraints are explicitly taken into account. In all these works, experiments confirm that with the time-varying sliding surface proposed in [104] the SMC is insensitive with respect to external disturbance and modelling uncertainty from the very beginning of the control process. Nevertheless, in this approach c has a constant variation over time, which results in different amount of sliding surface's rotation for different values of c. Therefore, in [108] the angle information between the sliding surface and the error coordinate axis is directly used in the time variation of c. Since the amount of change in the angle is directly proportional to the amount of change in the

position of the sliding surface, this contributes to a more meaningful adjustment of the sliding surface. In this method, the initial position of the sliding surface passes for the initial state of the system, so that the reaching phase is eliminated, while the final position is a design parameter. Concerning the switching scheme, a further modification of the approach illustrated in [104] is proposed in [109]. Here, α is defined with a quadratic polynomial, allowing to obtain a constant velocity shifting or a constant acceleration shifting depending on the parameters setting. Further results of the application of time-varying switching lines to the sliding mode control of the continuous time, second order dynamic systems are presented in [110], where the authors introduce a new coordinate frame, namely $(s-p)$ plane. The coordinates of that plane are the original sliding surface $s = \dot{e} + c \cdot e$ and $p = \dot{e} + c^{-1}e$, with $p = 0$ perpendicular to $s = 0$. Then, a linear sliding surface in the $(s-p)$ plane is generated as

$$\hat{s} = s + k_s p$$

where k_s defines the position of the proposed sliding surface and it is continuously adjusted through a time dependent function, thus to obtain a rotating sliding surface. In all the algorithms above, c and α are first chosen so that the system lies on the sliding surface at the beginning of the control process. After that, the sliding surface is moved according to predefined time polynomials so that it approaches a final position during the control process. Thus, in this scheme the movement of the sliding surface is not adjusted based on the states assumed by the dynamic system during the control process, rather it is merely a function of time. As a consequence, this scheme for moving the sliding surface requires an additional design parameter to be specified, i.e. the time interval taken by the sliding surface to reach the desired end position. In addition, should the system lose the sliding mode as a result of either a reference change or a perturbation, the mechanism for moving the sliding surface cannot detect this automatically, and its rotation towards the desired end position would continue even if the system is no longer on the sliding surface. In such a situation, in order to guarantee the robustness of the system, it is necessary to reset the time counted in the polynomials governing the movement of the sliding surface to zero and recalculate the initial position of the sliding surface in accordance with the states of the system.

In order to avoid these drawbacks, the control structure must be supplemented with an adaptive mechanism that can adjust the movement of the sliding surface according to the states of the system. With this goal in mind, some researchers have proposed

to combine fuzzy logic with SMC. A fuzzy adaptation for sliding mode controller is proposed in [111] with an application for a second order SISO system. Here, a first fuzzy approximator is used to update the slope of the linear sliding surface according to the position error, with the aim of improving the dynamics of the tracking error in the sliding regime. Furthermore, a second fuzzy approximator regulates the behaviour of the states in reaching phase. Instead, a Takagi-Sugeno fuzzy algorithm is proposed in [112] to realize a SMC with a linear time varying sliding surface. The latter is selected to pass for the initial conditions of the system at the beginning of the control process, and a different sliding surface is defined according to the quadrant of the phase plane where the initial conditions are located. After, both c and α are updated in real time basing on the states of the system through a Takagi-Sugeno fuzzy algorithm. Also, in [113] a fuzzy logic tuning algorithm is proposed to generate the rotation and the shifting of the sliding surface. However, the rotation is only permitted in a slope-increasing direction. A fuzzy tuning mechanism capable of rotating the sliding surface in both directions is presented in [114]. The time varying sliding surface design is undertaken by using the new coordinate axes proposed in [110]. Then, two-dimensional fuzzy rule tables are generated for the two stable regions of the state space to rotate the sliding surface in the new coordinate axes. Since two-dimensional fuzzy rule base increases the computation time of the control input significantly, an attempt to rotate the sliding surface by fuzzy logic rules using one dimensional rule base is presented in [115], with an application for control of single phase UPS inverter in [116]. A slightly different usage of the fuzzy logic in SMC is presented in [117], where a Takagi-Sugeno fuzzy system is used for directly obtaining the sliding surface with rule consequents. In particular, each rule of this system represents the maximum slope sliding surface for a certain set of parameters given in the premise part.

Fuzzy logic allows the sliding surface to be moved by taking into account the states of the system, but to achieve this requires the definition of fuzzy sets, input-output decision rules and defuzzification methods. As all this generates a non-negligible computational cost, in this work we want to use a novel adaptive law to rotate the sliding surface in a meaningful way, thus based on the states of the system. The new algorithm is based on the BLFOSM already seen in Section 3.1, and in view of the ability to adapt the slope of the sliding surface, we refer to it as adaptive BLFOSM. The main advantage of using the adaptive law is that it only requires a numerical integration to update the position of the sliding surface in real time. In

addition, the novelty brought by the adaptive law allows us to prove the reduction of the reaching time compared to the classic SMC with constant sliding surface. In fact, the adaptation causes the sliding surface to rotate towards the initial conditions of the system at the beginning of the control process. Consequently, the new control law improves the robustness of the controller for a wide range of initial conditions, eliminating the risk of long reaching phases with unconstrained trajectories. Then, once the system is in sliding mode, the adaptive law rotates the sliding surface so that it approaches the predetermined end position guaranteeing the desired tracking accuracy. In fact, the latter is closely related to the inclination of the sliding surface, and improves as λ increases, as revealed by Theorem 3.2. However, selecting a large λ in the conventional SMC can cause a very long reaching mode with non-predictable trajectories if the initial conditions are far from the sliding surface. On the other hand, small values of λ result in low tracking accuracy (Theorem 3.2) and long tracking times with the system in sliding mode (Eq. 3.18). In this perspective, a major contribution of the controller proposed in this work is to alleviate the compromises usually required when choosing the parameter λ in conventional SMC with constant sliding surface. Thanks to the new adaptive mechanism, it is only necessary to define the adaptation interval within which λ will automatically assume the appropriate value, depending on the stage of the control process. In particular, the aim of the adaptive law is to rotate the sliding surface towards the initial conditions of the system. In this way, the reaching phase is shortened, improving the robustness of the controller. Then, as the errors converge to zero with the system in sliding mode, the adaptive law allows λ to approach the predefined final value. The latter, is selected to guarantee the behaviour of the system near the equilibrium point is is as desired. Therefore, the adaptive law developed in this work guarantees small reaching times without compromising tracking accuracy, as is proven in the rest of the chapter.

4.2 Sliding mode control with adaptive sliding surface for second order scalar system

This section presents the development of the new sliding mode algorithm with adaptive sliding surface. In order to simplify the discussion, the design is carried out here for the second-order system with only one input (3.1) already employed to present the design of the algorithms in Section 3.2. Thus, the control objective

is to make the system follow a reference trajectory, ensuring that the error is kept within a given tolerance range. First, the BLFOSM algorithm of Subsection 3.2.2 is recalled, highlighting how it must be designed to meet the control objective. The new BLFOSM with adaptive sliding surface is then presented, detailing the equations and mathematical proofs of stability and reduction of the reaching time.

4.2.1 Preliminaries

$$\begin{aligned} \dot{x}_1 &= x_2 \\ \dot{x}_2 &= f(x) + u + d \end{aligned} \tag{4.2}$$

where $x = [x_1, x_2] \in \mathbb{R}^2$ is the state vector, f is a known function describing the features of the system, u is the control input, and d is an unknown, bounded disturbance such that $|d| < \overline{d}$. The control problem is to make the dynamics in (3.1) follow a feasible reference trajectory $x^* = [x_1^*, x_2^*] \in \mathbb{R}^2$, with $\dot{x}_1^* = x_2^*$. So, the error $e = [e_1, e_2] \in \mathbb{R}^2$ is defined as follows

$$e_1 = x_1^* - x_1 \tag{4.3a}$$

$$e_2 = x_2^* - x_2 \tag{4.3b}$$

and the control objective is to drive the tracking error e_1 within the set

$$\mathfrak{B}_E = \left\{ e_1 : \; e_1^2 \leq E^2 \right\} \tag{4.4}$$

whose bound E is the largest admissible deviation.
The control objective can be achieved asymptotically with the BLFOSM control algorithm already seen in Subsection 3.2.2, as the following proposition states.

Proposition 4.1. *the control law given by (3.3), (3.4a), (3.4b), (3.21), and (3.22), hence resulting in*

$$\sigma = e_2 + \lambda e_1, \tag{4.5}$$

$$u = \dot{x}_2^* - f(x) + \lambda e_2 + k \, \mathrm{sat}(\sigma), \tag{4.6}$$

is such that solutions of (4.2) asymptotically converge to the set $\mathfrak{B}_E$ in (4.4) if $k > \overline{d}$ and $\lambda \geq \frac{\overline{\sigma}}{E}$.

Proof. of Proposition 4.1
According to Theorem 3.1, Corollary 3.1, and the proof thereof, the system (4.2), (4.5) with the control input (4.6) converge in finite-time to the set $\mathfrak{B}_{\overline{\sigma}}$ in (3.23), i.e. $\{x \in \mathbb{R}^2,\ |\sigma| \leq \overline{\sigma}\}$ if $k > \overline{d}$.
After that, the dynamics is reduced to the sliding equation (3.25). i.e. $\dot{e}_1 + \lambda e_1 = \sigma \in [-\overline{\sigma},\ \overline{\sigma}]$, and Theorem 3.2 proved that e_1 asymptotically converge to the set $\mathfrak{B}_e$ in (3.30), i.e. $\{e_1 :\ e_1^2 \leq (\overline{\sigma}/\lambda)^2\}$. Therefore, using $\lambda \geq (\overline{\sigma}/E)$, we obtain:

$$\frac{\overline{\sigma}}{\lambda} \leq E \ \Rightarrow\ \left(\frac{\overline{\sigma}}{\lambda}\right)^2 \leq E^2, \tag{4.7}$$

which means the set $\mathfrak{B}_e$ of Theorem 3.2 is such that

$$\mathfrak{B}_e = \left\{e_1 :\ e_1^2 \leq E^2\right\} \tag{4.8}$$

and the control objective (4.4) is achieved, thus completing the proof. □

Proposition 4.1 reveals the existence of a lower limit on the range of λ values guaranteeing the fulfilment of the control objective. This minimum λ is given by

$$\lambda_{\min} = \frac{\overline{\sigma}}{E}, \tag{4.9}$$

which depends on $\overline{\sigma}$ and E as described below:

- For a given $\overline{\sigma}$ a larger $\lambda_{\min}$ is obtained with a smaller E, i.e. with an increased tracking accuracy.
- For a required tracking accuracy E, a larger $\lambda_{\min}$ is obtained with a larger $\overline{\sigma}$, namely, with a larger thickness of the boundary layer neighbouring the sliding surface where the trajectories of the closed-loop system evolve during the sliding phase.

The only parameter that the control designer can select is $\overline{\sigma}$, which is discussed below.

- With $\overline{\sigma} = 0$ the tracking error asymptotically converge to zero or any positive value of λ. Indeed, in this case the behaviour of the ideal FOSM control is recovered: the sliding equation is as in (3.18) and the magnitude of λ only

affects the convergence rate during sliding phase.
In order to relax the constraint and allow any $\lambda \in \mathbb{R}^+$ for the choice, it would be convenient to select $\overline{\sigma} = 0$, but in this case the controller presents the problem of chattering, i.e. high-frequency closed-loop oscillations caused by the discontinuity of the signum function in the control law.

- With $\overline{\sigma} > 0$, we have a constraint on the choice of $\lambda_{\min}$ as per (4.9). Nevertheless, $\overline{\sigma} > 0$ is a convenient choice to avoid chattering. In this way, a thicker boundary layer $\mathfrak{B}_{\overline{\sigma}}$ (3.23) exists where the discontinuity of the signum function is smoothened by the saturation function. Of course, the thicker the boundary layer, the higher $\overline{\sigma}$, thus reducing the chattering and requiring a larger $\lambda_{\min}$ to guarantee the specified tracking accuracy $|e_1| \leq E$.

To conclude, large values of λ increase both the tracking accuracy and the tracking speed during sliding phase. Nevertheless, large values of λ can adversely affect the control system when it is not in the sliding phase, possibly leading to a longer reaching phase if the initial conditions are far from the sliding surface. The solution proposed in the next generation to solve the shortcomings of FOSM with constant λ is to provide a real time adaptation of λ as follows: first the adaptive law rotates the sliding surface so that it moves towards the initial conditions of the system, so as to reduce the reaching time. Then, the adaptive law increases λ once the system has already reached the sliding surface. The real time adaptation of λ thus leads to both a reduction of the reaching time and an improvement of the tracking accuracy.

4.2.2 The novel BLFOSM algorithm with adaptive sliding surface

Here, the BLFOSM algorithm with a novel adaptive law for the time-varying sliding surface is defined to manage the same control problem described in previous subsection. This innovative SMC algorithm guarantees to reduce the reaching time while improving closed-loop tracking performance. As compared to the classical BLFOSM algorithm of Subsection 3.2.2, in this formulation the parameter λ is not constant and is regarded as an additional controller state with its own dynamics. With the errors (4.3), the sliding variable is defined as

$$\sigma(e, \lambda) = e_2 + \lambda e_1, \tag{4.10}$$

where we see that the sliding surface $\sigma(e,\lambda)=0$ can rotate in the phase plane (e_1,e_2), by adapting the slope λ. To this end, we propose

$$\dot{\lambda} = \text{proj}_{[\underline{\lambda},\overline{\lambda}]}(\lambda,h), \quad \lambda \in \left[\underline{\lambda},\overline{\lambda}\right], \tag{4.11a}$$

$$h = G\zeta_{\overline{\sigma}}(\sigma)\text{sign}(e_1) - c\left(\lambda - \overline{\lambda}\right), \quad G = \frac{c\left(\underline{\lambda} - \overline{\lambda}\right)}{\overline{\sigma}} < 0 \tag{4.11b}$$

where $c>0$ is chosen to be any positive scalar as will be justified in Theorem 4.2, $\overline{\sigma}>0$ is the thickness of the boundary layer $\mathfrak{B}_{\overline{\sigma}}$ neighbourhood of the sliding surface, already defined in Eq. (3.23), $\zeta_{\overline{\sigma}}$ is a piecewise constant function parameterized by $\overline{\sigma}$ as follows:

$$\zeta_{\overline{\sigma}}(\sigma) = \begin{cases} \sigma & \text{if} \quad |\sigma| \geq \overline{\sigma} \\ 0 & \text{if} \quad |\sigma| < \overline{\sigma}, \end{cases} \tag{4.11c}$$

and the projection function $proj_{[\underline{\lambda},\overline{\lambda}]}$ in Eq. (4.11a) is built as in [118] in such a way that the parameter λ is constrained in the interval $\left[\underline{\lambda},\overline{\lambda}\right]$. More specifically, the projection function works as a saturated integrator with saturation levels $\underline{\lambda}$ and $\overline{\lambda}$ as follows (see also [119]):

$$\text{proj}_{[\underline{\lambda},\overline{\lambda}]}(\lambda,h) = \begin{cases} \max\{0,h\} & \text{if } \lambda = \underline{\lambda} \\ h & \text{if } \underline{\lambda} < \lambda < \overline{\lambda} \\ \min\{0,h\} & \text{if } \lambda = \overline{\lambda} \end{cases} \tag{4.11d}$$

where $\underline{\lambda}>0$ and $\overline{\lambda}>0$ are the lower bounds and the upper bound of λ, respectively. For our adaptive law, $\overline{\lambda}$ should satisfy the constraint

$$\overline{\lambda} \geq \frac{\overline{\sigma}}{E} \tag{4.12}$$

as in (4.9), however the next theorem applies for any value $\overline{\lambda} > \underline{\lambda}$. Specifically, it establishes that the adaptive law (4.6), (4.11) provides both shorter reaching time and improved tracking accuracy compared to the classic BLFOSM (3.4a) with constant λ discussed above.

Theorem 4.1. *Under (4.12), for any value of $c > 0$, $\overline{\lambda} > \underline{\lambda}$, $\overline{\sigma} \geq 0$ and $k > \overline{d}$ the error (4.3) with the control law (4.6), (4.10), (4.11) is such that*

i. It converges in finite-time to the set $\mathfrak{B}_{\overline{\sigma}}$ (3.23).

ii. For each initial condition, $(e(0), \lambda(0)) = (e_0, \lambda_0)$, it converges to $\mathfrak{B}_{\overline{\sigma}}$ faster (or at worst as fast) than the BLFOSM with a constant $\lambda = \lambda_0$ if $d = 0$.

Proof. of Theorem 4.1
Similar to Eq. (3.14), the time derivative of the sliding variable σ in (4.10) can be computed as,

$$\dot{\sigma} = \dot{x}_2^* - f(x) - u - d + \lambda e_2 + \dot{\lambda} e_1 \tag{4.13}$$

where we see a new term involving $\dot{\lambda}$. Consider, as in Lemma 3.1, the quadratic Lyapunov function $V(e, \lambda) = \sigma^2$, whose derivative along (4.2), (4.6), (4.10), (4.11) yields

$$\dot{V} = 2\sigma\dot{\sigma} = 2\sigma \left(\dot{x}_2^* - f(x) - u - d + \lambda e_2 + \dot{\lambda} e_1 \right), \tag{4.14}$$

where we used u as in (4.6). For $|\sigma| \geq \overline{\sigma}$ we have:

$$\dot{V} = 2\sigma \left(-k \operatorname{sat}(\sigma) - d \right) + 2\sigma \left(\dot{\lambda} e_1 \right) = -2k\sigma \operatorname{sat}(\sigma) - 2\sigma d + 2\sigma \left(\dot{\lambda} e_1 \right) \tag{4.15}$$

Recalling that $|\sigma| > \overline{\sigma}$, we have $\sigma \cdot \operatorname{sat}(\sigma) = |\sigma|$. Furthermore, $-\sigma d < |\sigma| \overline{d}$. Therefore:

$$\dot{V} \leq -2k|\sigma| + 2\overline{d}|\sigma| + 2\sigma \left(\dot{\lambda} e_1 \right) = 2\left(-k + \overline{d} \right)|\sigma| + 2\sigma \left(\dot{\lambda} e_1 \right) \tag{4.16}$$

It must be noted that, along the trajectories of the closed-loop system, it can be $\dot{\lambda} = 0$ in a nonempty interval of time. Specifically, this situation occurs if at the same time λ is at the boundary of the interval $[\underline{\lambda}, \overline{\lambda}]$ and the adaptive law (4.11b) pushes λ outwards from the interval. In this case, (4.16) is the same as with the classical SMC, and its properties are thus recovered. Except for this situation, the adaptive law yields a non-zero $\dot{\lambda}$ and we obtain the following using (4.11), the fact that $|\sigma| > \overline{\sigma}$ implies $\zeta_{\overline{\sigma}}(\sigma) = \sigma$, and the expression of G in (4.11b):

$$\dot{V} \leq 2\left(-k+\overline{d}\right)|\sigma| + 2\sigma\left(G\sigma e_1 \operatorname{sign}(e_1) - c\left(\lambda - \overline{\lambda}\right)e_1\right) \tag{4.17}$$

$$\dot{V} \leq 2\left(-k+\overline{d}\right)|\sigma| + 2\left(G|e_1|\sigma^2 + c\left(\overline{\lambda} - \lambda\right)e_1\sigma\right) \tag{4.18}$$

$$\dot{V} \leq 2\left(-k+\overline{d}\right)|\sigma| + 2\left(\frac{\sigma^2}{\overline{\sigma}}c\left(\underline{\lambda} - \overline{\lambda}\right)|e_1| + c\left(\overline{\lambda} - \lambda\right)|e_1||\sigma|\right) \tag{4.19}$$

Now, exploiting the inequality $\left(\overline{\lambda} - \lambda\right) \leq \left(\overline{\lambda} - \underline{\lambda}\right)$ we obtain:

$$\begin{aligned}\dot{V} \leq & 2\left(-k+\overline{d}\right)|\sigma| - 2\frac{|\sigma|^2}{\overline{\sigma}}c\left(\overline{\lambda} - \underline{\lambda}\right)|e_1| + 2c\left(\overline{\lambda} - \underline{\lambda}\right)|e_1||\sigma| \\ \leq & 2|\sigma|\left(-k+\overline{d} - c|e_1|\left(\overline{\lambda} - \underline{\lambda}\right)\left(\frac{|\sigma|}{\overline{\sigma}} - 1\right)\right),\end{aligned} \tag{4.20}$$

where, using again the fact that $|\sigma| > \overline{\sigma}$, we have

$$c|e_1|\left(\overline{\lambda} - \underline{\lambda}\right)\left(\frac{|\sigma|}{\overline{\sigma}} - 1\right) = k_\varepsilon \geq 0 \tag{4.21}$$

Therefore we have

$$|\sigma| > \overline{\sigma} \;\Rightarrow\; \dot{V} \leq -2\left(k-\overline{d}\right)|\sigma| = -2\left(k-\overline{d}\right)V^{\frac{1}{2}}, \tag{4.22}$$

Due to Eq. (3.7), Lemma 3.1 applies for $z = x$, $y = \sigma$, $\alpha = 2\left(k - \overline{d}\right) > 0$, $\beta = 1/2 \in (0,1)$, and $\bar{y} = \overline{\sigma}$. Therefore, the statement (i) of Theorem 4.1 is proven to be true. Next, given the validity assumptions of the statement (ii) of Theorem 4.1, for any e_0 we have that the value of $\sigma(0) = \sigma_0$ resulting from (4.5) and (4.10) is the same. That is, the initial value of the sliding variable for the system controlled by the BLFOSM with a constant λ and for the system controlled by the BLFOSM with adaptive λ is the same. Setting apart the two cases with subscript 'c' (constant λ) and 'a' (adaptive λ), we have

$$V_c(0) = V_a(0) \tag{4.23}$$

Then, for $d = 0$ the time derivative of V_c along (4.2), (4.5), (4.6) yields:

$$\dot{V}_c = -2k\sigma \text{ sat}(\sigma), \tag{4.24}$$

as was found in Eq. (3.16) in the proof of Theorem 3.1. Note that the validity of this equation for the BLFOSM with constant λ is confirmed by Corollary 3.1 where $|\sigma| > \overline{\sigma}$. On the other side, under the same conditions $d = 0$ the time derivative of V_a along (4.2), (4.6), (4.10), (4.11) is obtained from (4.15) by eliminating the term in d:

$$\dot{V}_a = -2k\sigma \text{ sat}(\sigma) + 2\sigma\left(\dot{\lambda}e_1\right). \tag{4.25}$$

Making explicit the second term in equation above, according to (4.11) we obtain that:

$$\sigma\left(\dot{\lambda}e_1\right) = c\left(\frac{\sigma^2}{\overline{\sigma}}(\underline{\lambda} - \overline{\lambda})|e_1| - \sigma(\lambda - \overline{\lambda})e_1\right). \tag{4.26}$$

Now, due to $\underline{\lambda} < \overline{\lambda}$, we have:

$$\frac{\sigma^2}{\overline{\sigma}}(\underline{\lambda} - \overline{\lambda})|e_1| < 0 \quad \forall\, e_1 \neq 0. \tag{4.27}$$

Besides, due to $|\sigma| > \overline{\sigma}$ and $(\overline{\lambda} - \underline{\lambda}) \geq (\overline{\lambda} - \lambda)$, in the equation (4.26) we have:

$$\frac{\sigma^2}{\overline{\sigma}}\left|(\underline{\lambda} - \overline{\lambda})e_1\right| > \left|\sigma(\lambda - \overline{\lambda})e_1\right| \quad \forall\, e_1 \neq 0. \tag{4.28}$$

Therefore, putting (4.27), (4.28) into (4.26) we obtain:

$$\sigma\left(\dot{\lambda}e_1\right) \leq 0 \quad \forall\, |\sigma| > \overline{\sigma},\ e_1 \neq 0 \tag{4.29}$$

Thus, from the comparison between (4.24) and (4.25) we have $\dot{V}_a \leq \dot{V}_c\ \forall\ |\sigma| > \overline{\sigma}$, where the inequality rules everywhere except for $\dot{\lambda} = 0$. Together with (4.23), this proves the truth of statement (ii) of Theorem 4.1, thus completing the proof. □

Now, we address the sliding phase evolution in $\mathfrak{B}_{\overline{\sigma}}$. The compensated dynamics (3.25), i.e. $\dot{e}_1 + \lambda e_1 = \sigma \in [-\overline{\sigma},\ \overline{\sigma}]$, together with (4.11), describes the closed-loop behaviour inside $\mathfrak{B}_{\overline{\sigma}}$. Before stating the theorem for the stability properties of (3.25), (4.11), the following properties coming from [85, Theorem 4.1] is recalled. We can use Lemma 3.2 above and than proceed similarly to Proposition 4.1 to prove the following result.

Theorem 4.2. *The trajectories of the system (3.25), (4.11) asymptotically converge to the set* $\mathfrak{B}_\lambda = \left\{(e,\lambda):\ e_1 \in \mathfrak{B}_E,\ \lambda = \overline{\lambda}\right\}$.

Proof. of Theorem 4.2
Consider the candidate Lyapunov function $V(\lambda) = (\overline{\lambda} - \lambda)^2$ and note that in $\mathfrak{B}_{\overline{\sigma}}$, where (3.25) is constrained to evolve, we have $|\sigma| \leq \overline{\sigma}$ and $\zeta_{\overline{\sigma}} = 0$ according to Eq. (4.11c). Then, the time derivative of V along (4.11b) reads

$$\dot{V} = -2\left(\overline{\lambda} - \lambda\right)\dot{\lambda} = -2c\left(\overline{\lambda} - \lambda\right)^2 \tag{4.30}$$

Now, take $\varepsilon = 0$ as in Lemma 3.2. For any $\underline{V} > \varepsilon$ we obtain from (4.30),

$$V > \underline{V} \implies (\overline{\lambda} - \lambda)^2 > \underline{V} \implies \dot{V} \leq -2c\underline{V}^2 = \upsilon < 0, \tag{4.31}$$

which shows (3.28) of Lemma 3.2, thus, with to choice $c > 0$, λ asymptotically converge to $\overline{\lambda}$ for $\sigma \in \mathfrak{B}_{\overline{\sigma}}$. After that, by following the same steps as those of the proof of Proposition 4.1, it can be proven that the tracking error e_1 asymptotically converge to $\mathfrak{B}_E$ under condition (4.12), thus completing the proof. □

As far as c is concerned, the only condition necessary to guarantee the truthfulness of Theorems 4.1 and 4.2 is $c \in \mathbb{R}^+$. Therefore, in order to select a value for this parameter, it is useful to remember that during this phase the adaptive law (4.11)

gives $\dot{e}_1 \simeq -\overline{\lambda} e_1$. Thus, it is reasonable to choose c in the same range of values as $\lambda \in [\underline{\lambda}, \overline{\lambda}]$ since both of them drive the evolution of the states during sliding phase.

4.3 Sliding mode control with adaptive sliding surface for spacecraft applications

In this section, the new BLFOSM control algorithm with adaptive sliding surface is applied to stabilise the attitude dynamics of spacecraft. Firstly, in subsection 4.3.1 the novel control algorithm will be brought to bear on the mathematical models of spacecraft attitude dynamics presented in Chapter 2. In this way, we intend to extend the results obtained in Chapter 3, where chattering elimination, non-saturation of actuators, and control of flexible satellite with uncertain parameters were addressed, while the open goal was to reduce the reaching time. Next, in subsection 4.3.2 the novel BLFOSM control algorithm is designed to be implemented in the attitude dynamics simulator of DEMETER satellite from CNES.

4.3.1 The novel adaptive BLFOSM algorithm for spacecraft attitude control

This subsection describes the derivation of the innovative BLFOSM algorithm with adaptive sliding surface to manipulate the spacecraft attitude dynamics. The objective is to apply the control algorithm to the mathematical model used in Subsection 3.3.3, i.e. to steer the attitude dynamics of the flexible spacecraft with uncertain parameters. However, the effectiveness of the BLFOSM with adaptive sliding surface in controlling this complicated system is proven through numerical simulations in Chapter 5, while mathematical proof of stability is only given for the simplified case of the rigid satellite with known inertia. In fact, the controller is designed based on a simplified model in which we consider the satellite to be rigid and with true inertia equal to the nominal one, i.e. we consider J_0 to be the true inertia, whereas it is actually $J < \overline{J}$ as in Subsection 3.3.3. The other assumptions for the construction of the simplified mathematical model are listed below:

- the spacecraft is supposed to be rigid and with three known principal central axes of inertia, i.e. we consider the nominal value of the inertia $J_{0_{ii}}$ as the actual inertia of the spacecraft;
- the actuation systems consists of three RWs arranged in a cluster whose center of mass coincides with the one of the spacecraft;
- the rotation axis of each wheel is aligned with a principal central axis of the spacecraft;
- the body frame (see Chapter 2) is attached to the principal central axis of the spacecraft;
- the reaction wheels are started with zero-angular speed, while the set of allowable initial angular rate of the satellite is

$$\omega(0) = \omega_0 \in (-\overline{\omega}, \overline{\omega}), \quad \text{where} \quad \overline{\omega} = \overline{J}^{-1}\overline{h_{\text{rw}}}, \tag{4.32}$$

  with $\overline{J}$ the upper bound of J and $\overline{h_{\text{rw}}}$ the maximum angular momentum storable by the wheels, as in (3.85);
- the angular momentum absorbed by the wheels to counteract the external disturbances is neglectable;
- the gyroscopic terms are neglectable;
- small orientation angles are considered between body frame and objective frame.

Although these assumptions are similar to those used to carry out the controller design in Chapter 3, it should be noted that here the manoeuvre considered is generic (and not specifically inertial pointing) and that the satellite's initial velocity is not required to be zero. The decision to require ω_0 to be within the set in (4.32) is related to the controllability of the satellite using only the wheels. In fact, if the initial angular momentum of the satellite exceeds the maximum momentum that can be accumulated by the wheels, reaction-type actuators must be considered to discharge the excess angular momentum, so that controllability can be guaranteed. According to these assumptions, it follows that:

- each wheel provides active control around one axis of the spacecraft, so that each DOF has a dedicated control channel and a control law can be derived separately for each axis;
- the kimenatics and dynamics errors equations are given by Eqs. (2.27) and (2.70), as explained in Chapter 2.

Therefore, the complete mathematical model used for control design consists of three SISO systems as follows:

$$\begin{cases} \dot{q}_{e_{v,i}} &= \frac{1}{2}\omega_{e_i} \\ \dot{\omega}_{e_i} &= \frac{1}{J_{0_{ii}}}\left(\tau_i + d_i\right) \end{cases} \qquad i = x, y, z \tag{4.33}$$

where the subscript i will be used in the rest of the subsection to indicate a generic satellite axis, i.e. x, y, and z of the body frame.

Tuning of the adaptive BLFOSM

As in Chapter 3, for each system describing the rotational dynamics about one axis we define a linear sliding variable as follows:

$$\sigma_i = J_{0_{ii}}\left(\omega_{e_i} + \lambda_i q_{e_{v,i}}\right), \tag{4.34}$$

where the sliding surface $\sigma_i = 0$ can rotate in the phase plane through the real time adaptation of λ_i according to the following adaptation law, based on (4.11).

$$\dot{\lambda}_i = \text{proj}_{[\underline{\lambda},\overline{\lambda}]}\left(\lambda_i, h_i\right), \quad \lambda_i \in \left[\underline{\lambda}, \overline{\lambda}\right], \tag{4.35a}$$

$$h_i = G_i \zeta_{\overline{\sigma}}(\sigma_i)\text{sign}(q_{e_{v,i}}) - c\left(\lambda_i - \overline{\lambda}\right), \quad G_i = \frac{c\left(\underline{\lambda} - \overline{\lambda}\right)}{\overline{\sigma}} < 0 \tag{4.35b}$$

$$\zeta_{\overline{\sigma}}(\sigma_i) = \begin{cases} \sigma_i & \text{if} \quad |\sigma_i| \geq \overline{\sigma} \\ 0 & \text{if} \quad |\sigma_i| < \overline{\sigma}, \end{cases} \tag{4.35c}$$

$$\text{proj}_{[\underline{\lambda},\overline{\lambda}]}\left(\lambda_i, h_i\right) = \begin{cases} \max\{0, h_i\} & \text{if } \lambda_i = \underline{\lambda} \\ h_i & \text{if } \underline{\lambda} < \lambda_i < \overline{\lambda} \\ \min\{0, h_i\} & \text{if } \lambda_i = \overline{\lambda} \end{cases} \tag{4.35d}$$

where all the parameters are as discussed in previous Section. In particular, $\overline{\lambda}$ should be selected according to the pointing accuracy requirement $\overline{q_{e_v}}$. That is, for the controller to asymptotically satisfy

$$q_{e_{v,i}} \in [-\overline{q_{e_v}},\ \overline{q_{e_v}}], \tag{4.36}$$

$\overline{\lambda}$ must be selected such that

$$\overline{\lambda} \geq \frac{\overline{\sigma}}{\overline{q_{e_v}}} \tag{4.37}$$

according to (4.12), where $E = \overline{q_{e_v}}$. Instead, the control law we use to steer the attitude dynamics is

$$\tau_i = -k\ \mathrm{sat}\,(\sigma_i) - \frac{1}{2} J_{0_{ii}} \omega_{e_i}, \tag{4.38}$$

with

$$k > \overline{d}, \quad \overline{d} = \left\| (d_x,\ d_y,\ d_z) \right\|_\infty. \tag{4.39}$$

Closed-loop stability

The reachability of the system (4.33), (4.34), (4.35), (4.38), (4.39) at $\mathfrak{B}_{\overline{\sigma}}$ can be proved using a square Lyapunov function $V = \sigma^2$ as in Subsection 3.3.1. Following the same procedure as in (3.46) - (3.49), it is obtained that

$$\dot{V} = 2\sigma_i\,(-k\ \mathrm{sat}(\sigma_i) + d_i) + 2\sigma_i \left(\dot{\lambda}_i q_{e_{v,i}}\right), \tag{4.40}$$

in which, with respect to (3.49), we have an additional term

$$2\sigma_i \left(\dot{\lambda}_i q_{e_{v,i}}\right) < 0 \quad \forall |\sigma_i| > \overline{\sigma},\ q_{e_{v,i}} \neq 0, \tag{4.41}$$

as was proven in (4.29). The term $2\sigma_i \dot{\lambda}_i q_{e_{v,i}} < 0$, on the one hand increases the convergence speed towards $\sigma_i = 0$, decreasing the reaching time as seen in the previous section. On the other hand, by pushing the sliding surface towards the states of the system, this term supports switching control in overcoming disturbances by guaranteeing the reachability condition. In fact, in the simplified model (4.33) only orbital disturbances are considered (which are dominated by the switching control due to condition 4.39), but in the real problem we also have parametric uncertainties, unmodelled dynamics and gyroscopic terms when the total angular momentum is $H \neq 0$. In the classical FOSM with constant sliding surface, in order to ensure that

these effects do not impede the reachability of $\sigma_i = 0$, it would be necessary to characterise them so that they are included and cancelled with the equivalent control or to increase the gain k. Both options have disadvantages, as the former burdens the controller design, while the latter increases the risk of chattering. On the other hand, the term $2\sigma_i \left(\dot{\lambda}_i q_{e_{v,i}}\right) < 0$ in the adaptive FOSM allows unmodelled disturbances to be counteracted more effectively, without increasing the gain k or burdening the equivalent control. Therefore, although the design of the new controller is based on the simplified model (4.33), the numerical simulations in the next chapter show that it works well even with the flexible and uncertain satellite model. As far as actuator saturations are concerned, note that they were not explicitly taken into account in the formalisation of the controller. However, again the term $\dot{\lambda}_i q_{e_{v,i}}$ introduced by the adaptive law provides some help here. In fact, (4.41) allows to select a lower value of the gain k while still guaranteeing that σ_i reaches the set $\mathfrak{B}_{\overline{\sigma}}$ in finite time. In turn, smaller values of k decrease the risk of saturating either torque or angular momentum. Indeed, it is clear from the control law that k is directly related to the torque τ, which, in turn, directly impacts the satellite's acceleration as the equation of dynamics indicates. In conclusion, small values of k result in smaller torques and lower angular accelerations, especially during the reaching phase since $\tau_i \approx k$, thus alleviating the risk of actuator saturation (it should be recalled that angular momentum saturation is related to the angular velocity of the satellite).
Therefore, due to (4.40) the system (4.33), (4.34), (4.35), (4.38), (4.39) converge in finite time at $\mathfrak{B}_{\overline{\sigma}}$ during reaching phase. After, the compensated dynamics is obtained from (4.34) and the kinematics equation as

$$J_{0_{ii}} \left(2\dot{q}_{e_{v,i}} + \lambda_i q_{e_{v,i}}\right) = \sigma_i \in [-\overline{\sigma}, \overline{\sigma}], \tag{4.42}$$

where λ_i evolves according to (4.35), thus asymptotically converging to the $\overline{\lambda}$-value as stated by Theorem 4.2. Therefore, under the condition (4.37) and due to Proposition 4.1 (where $E = \overline{q_{e_v}}$), the tracking error asymptotically satisfies (4.36). Indeed, considering the square Lyapunov function

$$V = q_{e_{v,i}}^2, \tag{4.43}$$

whose derivatives along (4.42) for $\lambda_i = \overline{\lambda}$ yield

$$\dot{V} = 2q_{e_{v,i}}\dot{q}_{e_{v,i}} = \frac{q_{e_{v,i}}}{J_{0_{ii}}}\left(\sigma_i - \overline{\lambda}q_{e_{v,i}}\right) \leq 2\frac{\left|q_{e_{v,i}}\right|}{J_{0_{ii}}}\left(\overline{\sigma} - \overline{\lambda}\left|q_{e_{v,i}}\right|\right), \tag{4.44}$$

Now, we apply Lemma 3.2 with $\varepsilon = \left(\frac{\overline{\sigma}}{\overline{\lambda}}\right)^2$. For each $\underline{V} > \varepsilon$, we obtain from (4.44),

$$V > \underline{V} \implies |q_{e_{v,i}}|^2 > \underline{V} \implies \dot{V} \leq -\frac{2}{J_{0_{ii}}}\overline{\lambda}V(\underline{V} - \varepsilon) \leq -\frac{2}{J_{0_{ii}}}\overline{\lambda}\underline{V}(\underline{V} - \varepsilon) = -\upsilon, \tag{4.45}$$

which shows (3.28) of Lemma 3.2, thus system (4.42) asymptotically converge to (4.36).

Case of study

The novel adaptive BLFOSM control algorithm (4.34), (4.35), (4.37)-(4.39) is applied to the dynamic system (2.26), (2.38), (2.64) and (2.68) to simulate an inertial pointing maneuver. The maneuver and the satellite analyzed are the same that were used for the numerical simulations of Subsection 3.3.3. Therefore, the satellite is described in in Appendix A, and the parameters of the dynamics system are in Table 5.4. Instead, the parameters of the adaptive controller are listed in Section 5.4, where the most relevant results are also shown.

Discussion of the results

The objective of this work was to certify through numerical simulations the benefit of the BLFOSM with adaptive sliding surface over the classical BLFOSM with constant sliding surface in spacecraft attitude control applications. In particular, while analyzing the results in Subsection 3.3.3, we identified some issues with the controller designed in that work. These were mainly related to the duration of the reaching phase, the validity of the approach related to the assumption of zero initial angular momentum of the system, and the lengthy procedure for tuning the control gains to avoid actuators saturation and to prove the closed-loop stability. The results obtained with the adaptive BLFOSM seem to be promising for alleviating these problems. In fact, the adaptation of the sliding surface ensures the almost-

elimination of the reaching phase irrespective of the initial conditions of the system. Furthermore, the proposed adaptive law seems to minimise the risk of saturations, decreasing both the control effort for large initial state errors and the reaching time when the system trajectories are unconstrained. In addition, the adaptive algorithm allows the BLFOSM to work with a high λ when the satellite is close to the null attitude error, thus guaranteeing high pointing accuracy while avoiding the problems encountered with a highly inclined sliding surface during the reaching phase. Also, the rotation of the gliding surface towards the initial states of the system improves the stability of the closed-loop system, as it helps the dynamic system to reach the sliding surface. Finally, numerical simulations showed that the adaptive BLFOSM energises the flexible dynamics less than the classical BLFOSM, alleviating the problems of coupling with the attitude dynamics.

4.3.2 The novel adaptive BLFOSM algorithm for attitude control of DEMETER

In this subsection, the novel BLFOSM with adaptive sliding surface is used to provide attitude control of the DEMETER, a French microsatellite of the program Myriade from CNES. The benchmark of this satellite was provided by CNES in [2] and [120], including the simulation of the attitude dynamic and kinematic, the reaction wheels, and the controller. For the latter, it is specified that for attitude control design purposes the three satellite axes may be considered to be decoupled, thus allowing independent synthesis for each axis, as in [120]. Furthermore, we can write the linear model of the attitude dynamics and kinematics as in (4.33), but since the CNES control law uses Cardan angles, it is more convenient to substitute the kinematics equation as follows:

$$\begin{cases} \dot{\theta}_{e_i} & = \omega_{e_i} \\ \dot{\omega}_{e_i} & = \frac{1}{J_{ii}}(\tau_i + d_i) \end{cases} \qquad i = x, y, z \tag{4.46}$$

where θ are the Cardan angles, which can be obtained from the quaternions according to the transformations seen in Chapter 2. The Attitude and Orbit Control System (AOCS) of Demeter includes four different modes, but this work will only consider the normal mode where we use reaction wheels (one per axis). The control law

developed by CNES and implemented on the spacecraft's onboard computer [120] is composed of two blocks in series, as follows:

(i) The first block is a switching control law, where the switch takes place according to the pointing error θ_{e_i} and a threshold value θ_{t_i} as follows:

$$|\theta_{e_i}| \geq \theta_{t_i} \Rightarrow \tau_i = -b_i \operatorname{sign}(\theta_{e_i}) - \omega_{e_i} \tag{4.47}$$

$$|\theta_{e_i}| < \theta_{t_i} \Rightarrow \tau_i = -K_{p_i}\theta_{e_i} - K_{d_i}\omega_{e_i} \tag{4.48}$$

where K_{p_i} and K_{d_i} are the PD gains chosen for the linearized model (4.46). The switching value θ_{t_i} is given from engineering considerations and the speed bias b_i is selected imposing $\theta_{t_i}/b_i = K_{d_i}/K_{p_i}$ in order to minimize discontinuities in the control. The numerical values of the parameters can be found in [2].

(ii) The second block is a high order LTI controller designed with H_2/H_∞ optimization assuming the PD controller is given and including in the model many complications such as the flexible modes and the reaction wheels. This design is described in [120] and allows very accurate tracking performance for small pointing errors.

The objective is to replace the switching control law (4.47), (4.48) with the adaptive BLFOSM while keeping the stabilising filters in the loop, i.e. the block *Filter* in the scheme in Fig. 4.1, whose details are in [2, 120]. To this end, the new controller must fulfil the control objective, which is to satisfy

$$\theta_{e_i} \in \mathfrak{B}_{\overline{\theta}}, \quad \mathfrak{B}_{\overline{\theta}} = \{\theta_{e_i} : \ |\theta_{e_i}| \leq \overline{\theta}\} \tag{4.49}$$

while minimizing reaction wheels saturation during the maneuver.

Tuning of the adaptive BLFOSM

The fulfillment of (4.49) requires the control law mimics the PD controller (4.48) at small pointing errors, whereas to avoid saturation, control efforts must be appropriately decreased when the pointing error is large. For this reason, the BLFOSM with adaptive sliding surface appears to be a good choice to replicate the switching control law (4.47), (4.48). Below are the details of the new controller design for this

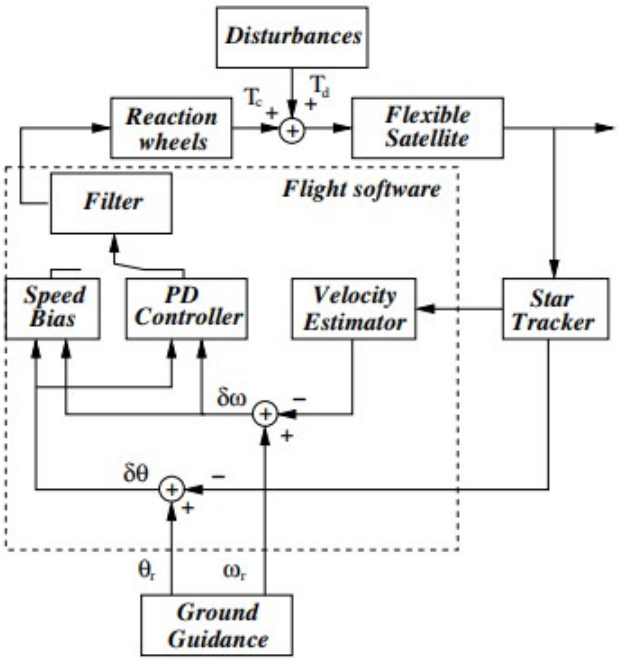

Fig. 4.1 DEMETER control loop [2]

application. The sliding surface is selected as

$$\sigma_i = \omega_{e_i} + \lambda_i \theta_{e_i}, \tag{4.50}$$

with λ_i that is time varying in the set $[\underline{\lambda}_i, \overline{\lambda}_i]$ according to the adaptive law (4.35) (note that here we have θ_{e_i} in place of $q_{e_{v,i}}$. Instead, as usual $\overline{\sigma}$ is the size of the boundary layer within which the closed-loop system converges during the reaching phase, thanks to the following control law

$$\tau_i = k_i \, \mathrm{sat}(\sigma_i). \tag{4.51}$$

As mentioned above, the control law should mimic the PD controller (4.48) at small pointing errors. For the fulfillment of this task, we consider the closed-loop system given by (4.46), (4.48), and $d_i = 0$. The latter is described by the following:

$$\begin{bmatrix} \dot{\theta}_{e_i} \\ \dot{\omega}_{e_i} \end{bmatrix} = A_{eq_i} \begin{bmatrix} \theta_{e_i} \\ \omega_{e_i} \end{bmatrix}, \quad A_{eq_i} = \begin{bmatrix} 0 & 1 \\ -\frac{K_{p_i}}{J_{ii}} & -\frac{K_{d_i}}{J_{ii}} \end{bmatrix} \tag{4.52}$$

Instead, by virtue of (4.51) and (3.21), for $|\sigma_i| \leq \overline{\sigma}$ and $\lambda_i = \overline{\lambda}_i$ the closed-loop system with adaptive BLFOSM is described by the following:

$$\begin{bmatrix} \dot{\theta}_{e_i} \\ \dot{\omega}_{e_i} \end{bmatrix} = A_{eq_i} \begin{bmatrix} \theta_{e_i} \\ \omega_{e_i} \end{bmatrix}, \quad A_{eq_i} = \begin{bmatrix} 0 & 1 \\ -\frac{k_i \overline{\lambda}_i}{\overline{\sigma} J_{ii}} & -\frac{k_i}{\overline{\sigma} J_{ii}} \end{bmatrix} \tag{4.53}$$

Therefore, we set

$$\frac{k_i \overline{\lambda}_i}{\overline{\sigma}} = K_{p_i}, \quad \frac{k_i}{\overline{\sigma}} = K_{d_i} \tag{4.54}$$

to make the behaviour of the closed-loop system with adaptive BLFOSM match that of the closed-loop system with PD from CNES near the zero-errors equilibrium point. Indeed, once the sliding phase reached ($|\sigma_i| \leq \overline{\sigma}$), the slope of the sliding surface asymptotically converge to $\overline{\lambda}_i$ thus providing that the controller behaves the same as the PD controller at low pointing error if the second of (4.54) is also complied with. From the latter, it is clear that k_i must be fixed in order to derive $\overline{\sigma} i$ (or vice versa). A range of values between a lower and an upper limit is available for the choice of k_i. In fact, on one side the parameter k_i has to meet the reachability condition and, on the other side, k_i should be chosen without torque saturation of the wheels. Therefore, the range of allowable values for K_j is

$$\overline{d} < K < \overline{\tau} \tag{4.55}$$

where $\overline{d}$ is the upper bound of the external disturbances and $\overline{\tau}$ is the maximum torque developed by the reaction wheels. To choose k_i within this range, it is useful to consider that k_i is related to the speed at which the system converges on the boundary layer neighbouring the sliding surface. Therefore, as k_i increases, the angular acceleration of the satellite increases with the risk of actuator saturation. For this reason, k_i is selected to be slightly higher than $\overline{d}$. Finally, $\overline{\sigma}$ results from the second of (4.54), while $\overline{\lambda}_i$ comes from the first of (4.54). Thanks to this design, the adaptive BLFOSM succeeds to mimic the PD controller (4.48) at small pointing errors. Instead, during reaching phase ($|\sigma_i| \leq \overline{\sigma}$) the objective is to decrease the control effort, so as to avoid saturation. Over this stage, the adaptive law rotates the sliding surface towards the states of the system, reducing the reaching phase convergence time. For large initial values of the attitude error and small values of the angular rate, λ_i shall be decreasing and the sliding phase shall thus start with a low equivalent proportional gain $k_i \lambda_i / \overline{\sigma}$. Therefore, the adaptive BLFOSM succeeds

in decreasing the control effort for large pointing error, thus to minimize the risk of saturation.

Case of study

The adaptive BLFOSM control algorithm (4.50), (4.51), (4.35 with θ_{e_i} in place of $q_{e_{v_i}}$), satisfying (4.54) is applied to a high fidelity simulator of the DEMETER satellite provided by CNES to perform inertial pointing maneuvers. The adaptive BLFOSM is brought into comparison with the switching control law from CNES (4.47), (4.48) and with a classical BLFOSM with constant sliding surface, in which $\lambda_i = \overline{\lambda_i}$, while k_i and $\overline{\sigma}$ are the same as in the adaptive BLFOSM. In this way, the BLFOSM with constant sliding surface also satisfies (4.54). Montecarlo simulations are performed with a wide range of initial conditions, such that

$$\theta_i(0) \in [-\pi,\ \pi], \quad \omega_i(0) \in \frac{1}{2}\left[-\frac{\overline{h_{\mathrm{rw}}}}{J_{ii}},\ \frac{\overline{h_{\mathrm{rw}}}}{J_{ii}}\right], \tag{4.56}$$

where the set of initial angular rates is chosen in order to guarantee the controllability of the satellite using only the wheels, as in (4.32). The maneuvers and the parameters of controller are listed in Section 5.5, where the most relevant results are also shown.

Discussion of the results

The numerical simulations confirmed the effectiveness of the adaptive BLFOSM in stabilising DEMETER's attitude dynamics near zero error, whereas the classical BLFOSM failed this task. Indeed, for large initial pointing errors the classical BLFOSM incurs actuator saturations that cause the system to lose stability. Thanks to the time-varying sliding surface, the adaptive BLFOSM avoids saturations for large pointing errors such as the CNES control law (4.47), preserving system stability and ensuring pointing as accurate as with the CNES PD (4.48). Therefore, the control law devised in this PhD appears suitable to replicate the switching control law (4.47), (4.48).

Chapter 5

Simulation results

Each section in this chapter provides the results of numerical simulations for the scenarios set out in Chapters 3 and 4. For each of the items addressed in this thesis, the results obtained are briefly commented on, highlighting the focal aspects that emerged from the numerical simulations. Afterwards, general conclusions are drawn in the "discussion of results", i.e. in the sections in Chapters 3 and 4 corresponding to the numerical results in this chapter.

5.1 Results of chattering attenuation in SMC

This section details the simulation scenario introduced in Subsection 3.3.1 and provides the results of the numerical simulations performed in *Matlab* environment. As discussed in Subsection 3.3.1, the objective is to apply the BLFOSM (3.50) and the STW (3.65) control laws to the dynamics system (2.26), (2.37), and (2.38) to simulate an inertial pointing maneuver in which the objective is to align the body frame with the inertial frame, which is thus the objective frame. Thus, at the beginning of the control process there exists an attitude error Θ_0, given by the orientation of the body frame relative to the inertial (objective) frame, and the controllers are supposed to steer the error to zero. The objective of the comparison is to evaluate the performance developed by the two controllers from the point of view of chattering elimination and pointing accuracy. In addition, the performance developed by the same control law will be compared for two values of the update frequency, one being low ($f_l = 10$ Hz) and one being high ($f_h = 10^3$ Hz). The

parameters of both the maneuvers and the dynamics system are listed in Table 5.1, whilst the control parameters are in Table 5.2.

Table 5.1 Parameters of the maneuver and of the dynamics system

Initial orientation:	$\Theta_0 = (\phi_0,\ \theta_0,\ \psi_0) = (40,\ -30, 20)$ deg
Desired orientation:	$\Theta^* = (\phi^*,\ \theta^*,\ \psi^*) = (0,\ 0,\ 0)$ deg
Initial angular rate:	$\omega_0 = (0,\ 0,\ 0)\ \frac{\text{rad}}{\text{s}}$
Desired angular rate:	$\omega^* = (0,\ 0,\ 0)\ \frac{\text{rad}}{\text{s}}$
Inertia tensor:	$J = \begin{bmatrix} 6 & 0 & 0 \\ 0 & 2 & 0 \\ 0 & 0 & 4 \end{bmatrix}$ kg m^2
Orbital disturbances:	$d = 10^{-5} \cdot \begin{bmatrix} 1+\sin(\frac{\pi}{150}t + \frac{\pi}{4}) \\ 1+\sin(\frac{\pi}{200}t + \frac{3\pi}{4}) \\ 1+\sin(\frac{\pi}{300}t + \frac{\pi}{2}) \end{bmatrix}$ N m
Torque max RWs:	$\overline{\tau} = 2 \cdot 10^{-3}$ N m
Initial angular momentum RWs:	$h_{\text{rw}_0} = (0,\ 0,\ 0)\ \text{kg}\frac{\text{m}^2}{\text{s}}$

Table 5.2 Parameters of the controllers

BLFOSM (3.50)	$\lambda = 0.04$
	$k = 2 \cdot 10^{-3}$
	$k_\sigma = 10^3$
STW (3.65)	$\lambda = 0.04$
	$\gamma = 1.9 \cdot 10^{-2}$
	$\eta = 8.4 \cdot 10^{-5}$
	$U_M = 1.2 \cdot 10^{-3}$

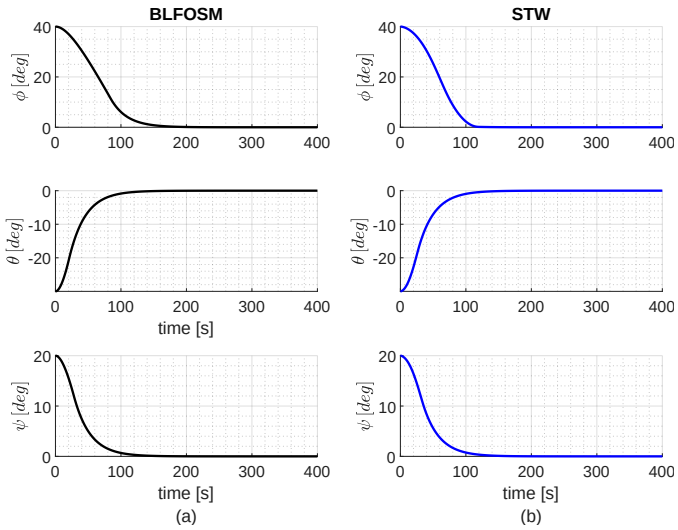

Fig. 5.1 Euler angles during the attitude maneuver with BLFOSM (a) and STW (b) for $f_l = 10$ Hz

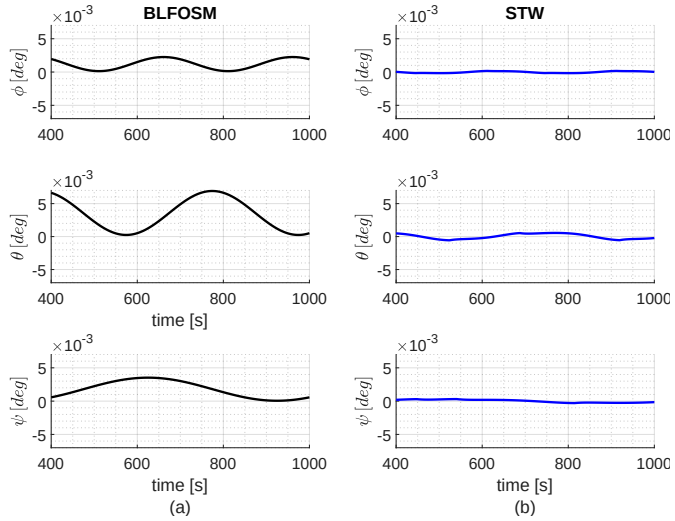

Fig. 5.2 Residual pointing error in Euler angles with BLFOSM (a) and STW (b) for $f_l = 10$ Hz

Figure 5.1 shows that both BLFOSM and STW succeed in steering the dynamic system to zero pointing error, while Figure 5.2 reveals that STW provides higher pointing accuracy. This is reasonable since, from the theoretical view, the STW guarantees σ converges to zero, whereas the BLFOSM only guarantees that σ converges to the set $|\sigma| \leq \overline{\sigma}$.

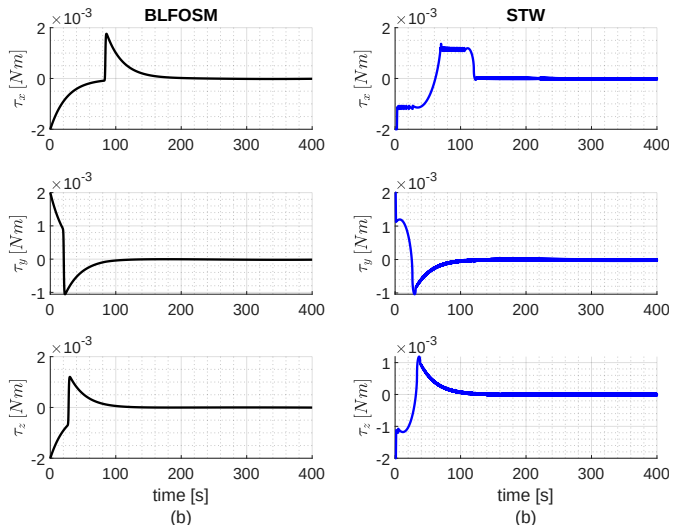

Fig. 5.3 Control torque during the first 400 seconds with BLFOSM (a) and STW (b) for $f_l = 10$ Hz

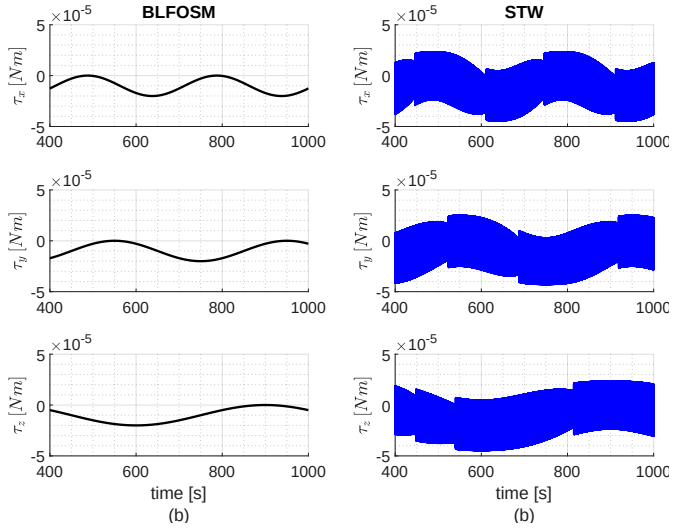

Fig. 5.4 Control torque during the last 600 seconds with BLFOSM (a) and STW (b) for $f_l = 10$ Hz

Figure 5.3 shows the control torque computed by the two control laws, revealing that during manoeuvring the output of the STW is smoother than the output of the BLFOSM. However, the latter manages to completely eliminate chattering, which is present in the STW, albeit to a small extent how it can be seen in Figure 5.4.

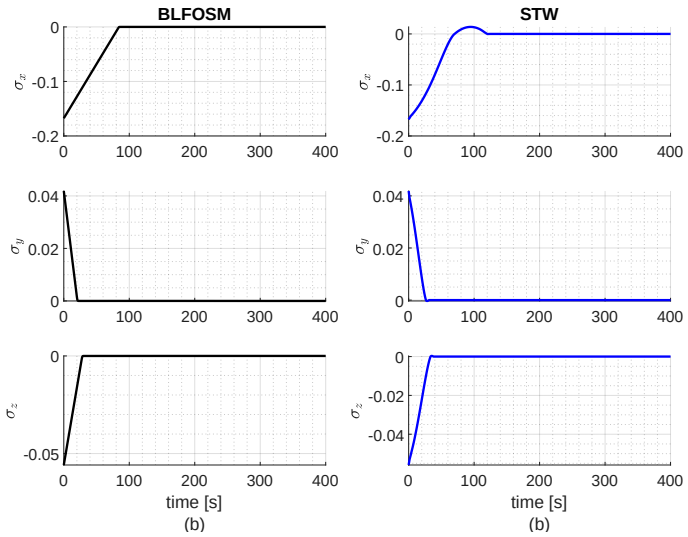

Fig. 5.5 Sliding variable during reaching phase with BLFOSM (a) and STW (b) for $f_l = 10$ Hz

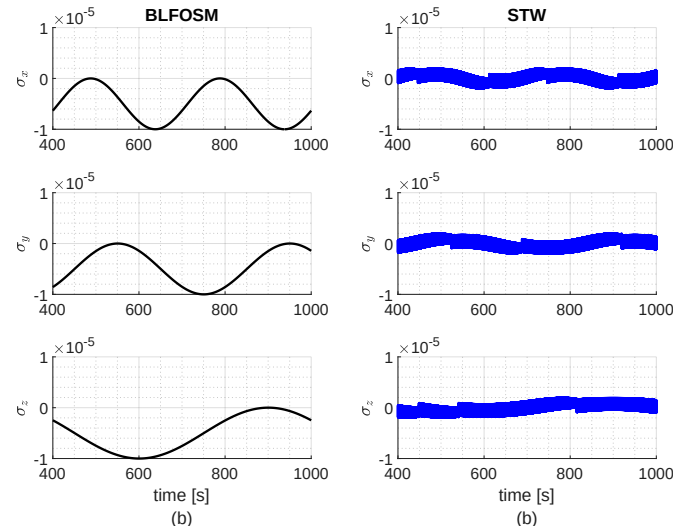

Fig. 5.6 Sliding variable during sliding phase with BLFOSM (a) and STW (b) for $f_l = 10$ Hz

Figure 5.5 shows that the reaching phase of the BLFOSM is shorter than that of the STW, confirming the results in Figure 5.1 where it appeared that the BLFOSM produces a faster manoeuvre. On the other side, Figure 5.6 shows some residual high-frequency oscillations in σ with STW, which do not occour with BLFOSM. This confirms the results in Figure 5.4 regarding the chattering of the control signal. Also, Figure 5.6 justifies the results of Figure 5.2, whose shows a better tracking accuracy with STW, where the mean value of the oscillations is approximately zero,

compared to the BLFOSM, where the mean value of the oscillation trend (due to disturbances) is non-zero.

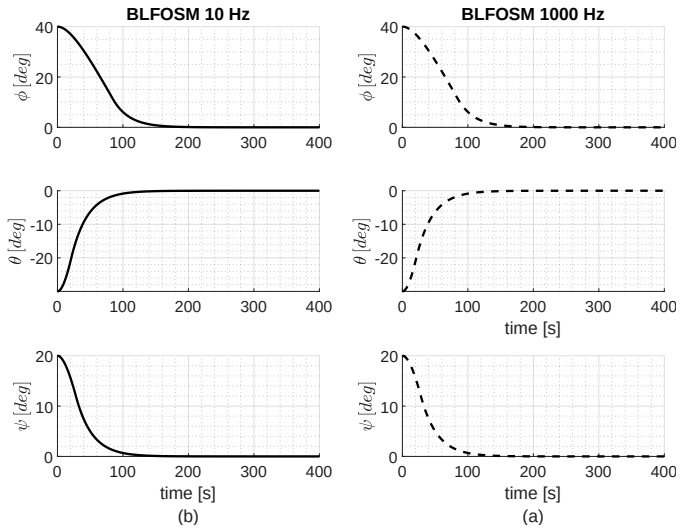

Fig. 5.7 Euler angles during the attitude maneuver with BLFOSM for $f_l = 10$ Hz (a) and $f_h = 10^3$ Hz (b)

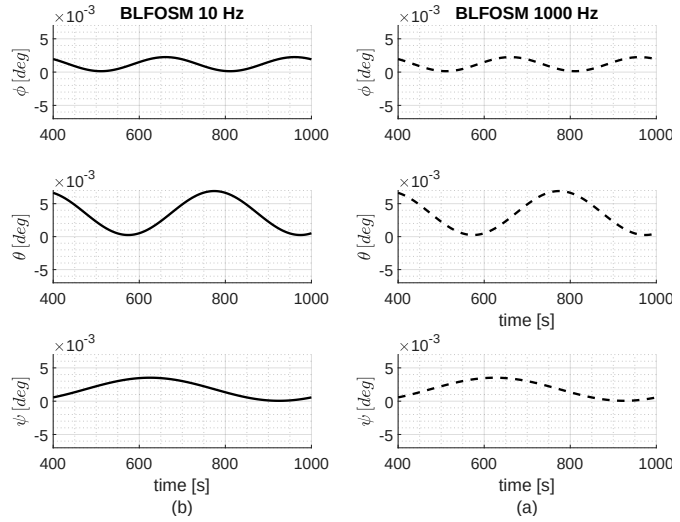

Fig. 5.8 Residual pointing error in Euler angles with BLFOSM for $f_l = 10$ Hz (a) and $f_h = 10^3$ Hz (b)

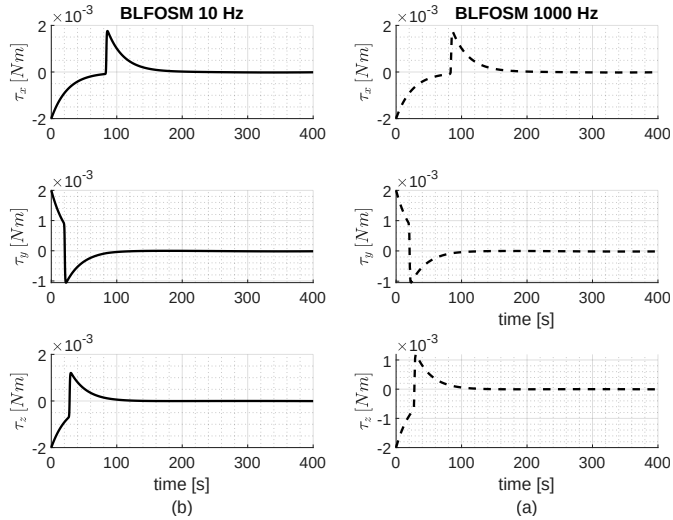

Fig. 5.9 Control torque during the first 400 seconds with BLFOSM for $f_l = 10$ Hz (a) and $f_h = 10^3$ Hz (b)

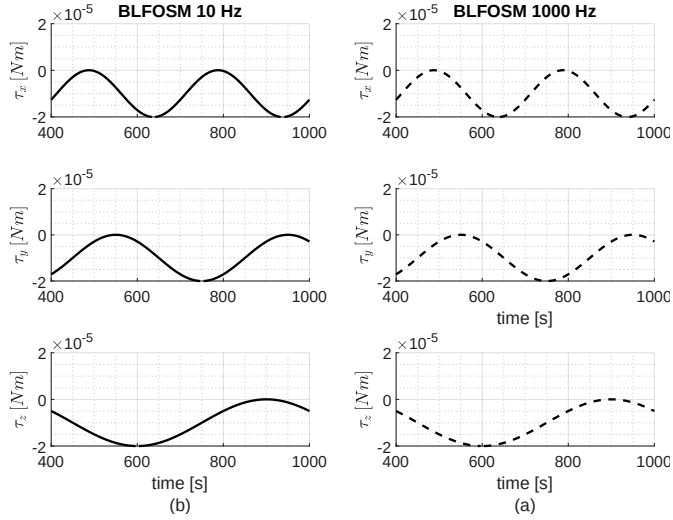

Fig. 5.10 Control torque during the last 600 seconds with BLFOSM for $f_l = 10$ Hz (a) and $f_h = 10^3$ Hz (b)

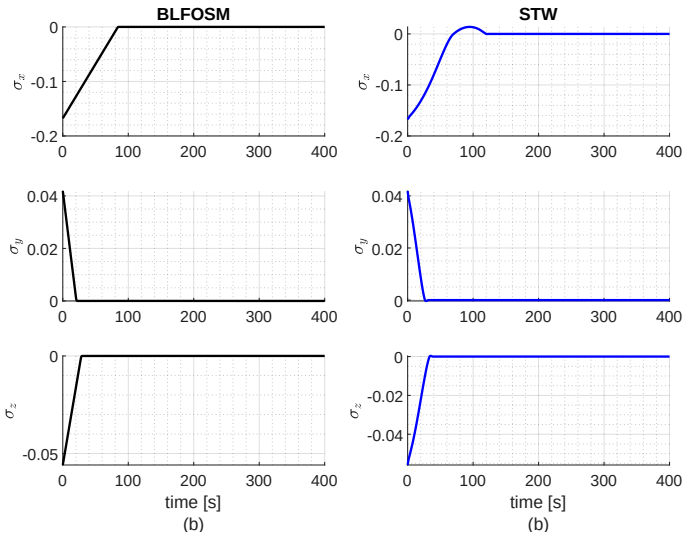

Fig. 5.11 Sliding variable during reaching phase with BLFOSM for $f_l = 10$ Hz (a) and $f_h = 10^3$ Hz (b)

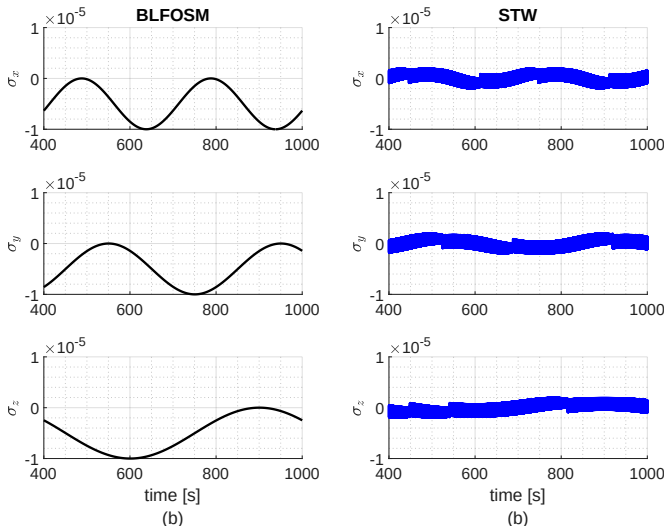

Fig. 5.12 Sliding variable during sliding phase with BLFOSM for $f_l = 10$ Hz (a) and $f_h = 10^3$ Hz (b)

The results of the comparison between the BLFOSM with $f_l = 10$ Hz and with $f_h = 10^3$ Hz are shown in Figures 5.7 to 5.12. They reveal that the frequency at which the controller operates does not affect the performance offered by the BLFOSM, making it a suitable controller to work under conditions of low available computing power.

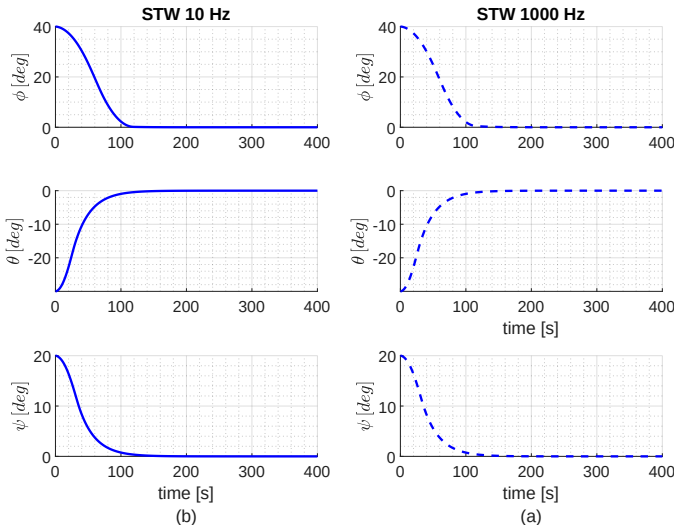

Fig. 5.13 Euler angles during the attitude maneuver with STW for $f_l = 10$ Hz (a) and $f_h = 10^3$ Hz (b)

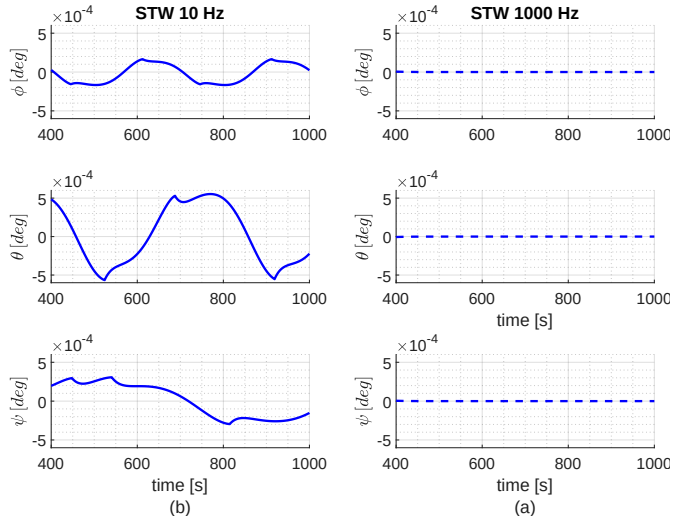

Fig. 5.14 Residual pointing error in Euler angles with STW for $f_l = 10$ Hz (a) and $f_h = 10^3$ Hz (b)

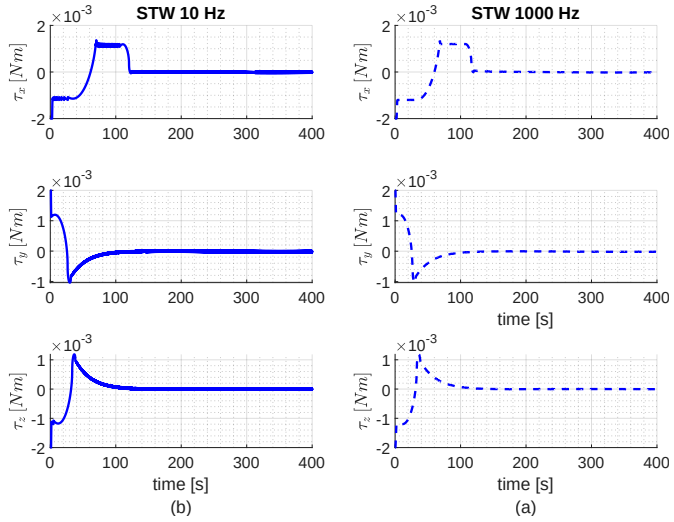

Fig. 5.15 Control torque during the first 400 seconds with STW for $f_l = 10$ Hz (a) and $f_h = 10^3$ Hz (b)

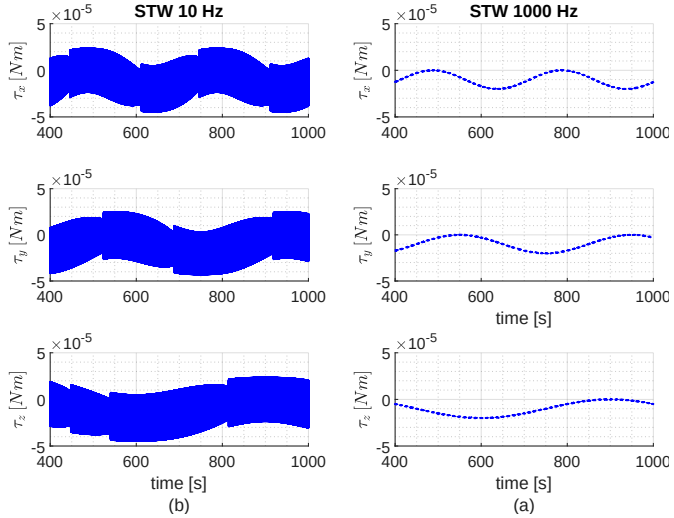

Fig. 5.16 Control torque during the last 600 seconds with STW for $f_l = 10$ Hz (a) and $f_h = 10^3$ Hz (b)

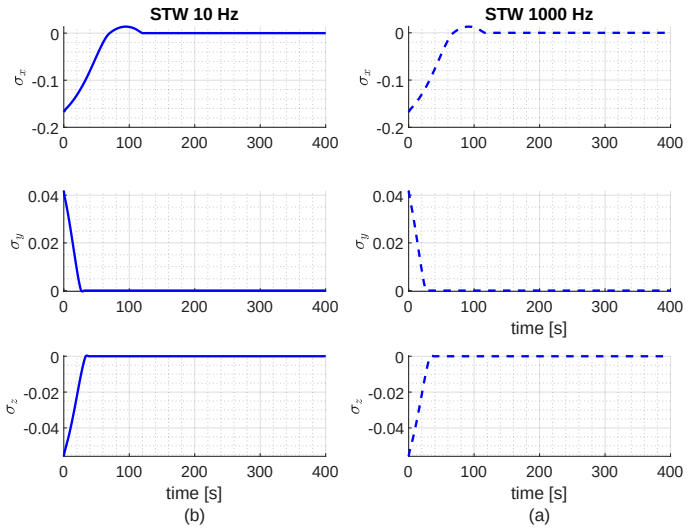

Fig. 5.17 Sliding variable during reaching phase with STW for $f_l = 10$ Hz (a) and $f_h = 10^3$ Hz (b)

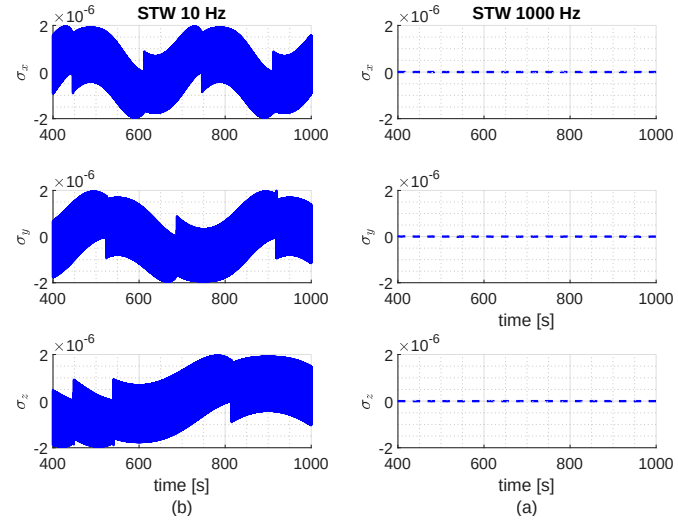

Fig. 5.18 Sliding variable during sliding phase with STW for $f_l = 10$ Hz (a) and $f_h = 10^3$ Hz (b)

The results of the comparison between the STW with $f_l = 10$ Hz and with $f_h = 10^3$ Hz are shown in Figures 5.13 to 5.18. Thus, the refresh rate definitely affects the performance offered by the STW, which appears to offer better performance than the BLFOSM when operating at $f_h = 10^3$ Hz. However, this requires high computational power, which makes it unattractive for spacecraft applications.

5.2 Results of BLFOSM design inclusing actuator constraints

This section details the simulation scenario introduced in Subsection 3.3.2 and provides the results of the numerical simulations performed in *Matlab* environment. The simulations are carried out with a sampling step of 0.01 s and the solver is *ode4*. The simulation scenario is the same as in the Section 5.1, so we want to study an inertial pointing manoeuvre with a rigid satellite, and the parameters for both are the same as in Table 5.1. The mathematical model for attitude dynamics of the spacecraft actuated by RWs is built with eqs. (2.26), (2.37), and (2.38) and the objective is to perform the attitude manoeuvre ensuring that the torque and angular momentum of the RWs do not exceed the actuator constraints. Indeed, only the torque saturation was considered in Section 5.1, whilst here the angular momentum saturation is also included. In order to achieve the objective, a new BLFOSM control structure is designed with the control law (3.50), in which the control parameters are tuned according to Eqs. (3.74) and (3.76). The control gains resulting from these equations are in Table 5.3 together with the features of the actuation system. Numerical simulations are performed to confirm that this tuning avoids actuator saturation. Moreover, the results are compared with the BLFOSM control law used in previous section, given by eq. (3.50) and with control parameters as in Table 5.2, to show the effectiveness of the tuning strategy in Subsection 3.3.2.

Table 5.3 Parameters of the new BLFOSM and of the actuation system

BLFOSM (new)	$\lambda = 0.405$
	$k = 0.99 \cdot 10^{-3}$
	$k_\sigma = 10^3$
Actuation system	$\overline{\tau} = 2 \cdot 10^{-3}$ N m
	$\overline{h_{\text{rw}}} = 3 \cdot 10^{-2}$ kg$\frac{\text{m}^2}{\text{s}}$

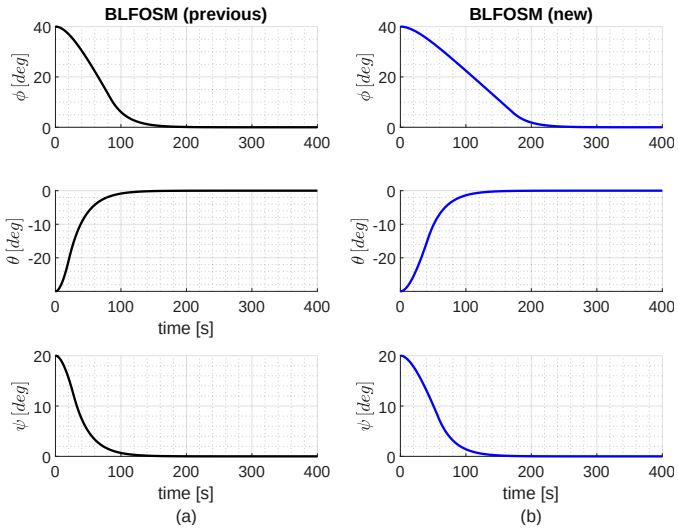

Fig. 5.19 Euler angles during the attitude maneuver of BLFOSM with actuators constraints

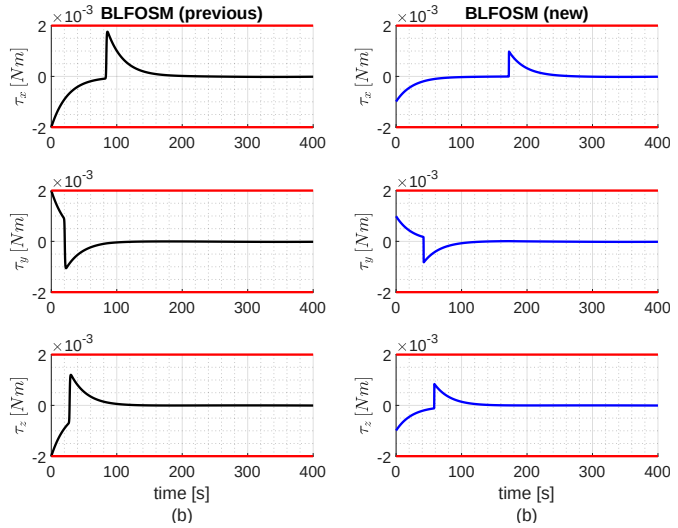

Fig. 5.20 Control torque of BLFOSM with actuators constraints

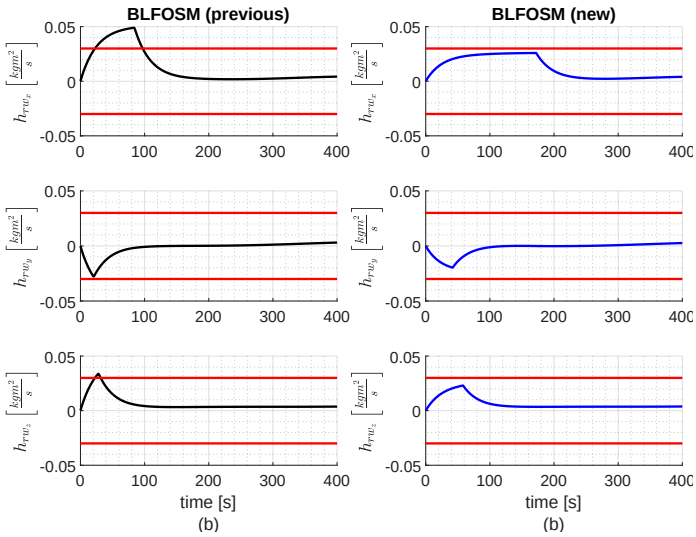

Fig. 5.21 Angular momentum of RWs of BLFOSM with actuators constraints

Figures 5.19 to 5.21 provide the results of the numerical simulations for this simulation scenario. The results with *BLFOSM (previous)* are associated to the control law (3.50) with control gains in Table 5.2, whilst the results with *BLFOSM (new)* are associated to the control law (3.50) with control gains in Table 5.3. Figure 5.19 shows that both the control laws succeed in steering to zero the pointing error, but the maneuver simulated with the previous BLFOSM algorithm can not be realized by the physical actuators because angular momentum saturations occur in the wheels controlling the x and z axis. The angular momentum saturation is avoided with the new BLFOSM control law, thanks to a well tuned gain λ. Also, Figure 5.19 shows that the new BLFOSM control law requires a minor control effort with respect to the previous one, thanks to a better tuned control gain k. When comparing the two manoeuvres in Figures 5.19 to 5.21, the differences are not so marked, but despite this, the design strategy studied in Subsection 3.3.2 for the gains of the control law (3.50) proved effective, setting precise rules to avoid wheel saturation. In fact, the latter may be more pronounced in other situations, depending on the inertia of the satellite and the features of the wheels.

5.3 Results of BLFOSM design including parametric uncertainties

This section details the simulation scenario introduced in Subsection 3.3.3 and provides the results of the numerical simulations performed in *Matlab* environment. The simulations are carried out with a sampling step of 0.01 s and the solver is *ode4*. The objective is to perform the same inertial pointing maneuver studied in the previous two sections, so the initial conditions (Θ_0, ω_0, and h_{rw_0}), the desired final conditions (Θ^* and ω^*) and the orbital disturbances d are as in Table 5.1. As discussed in Subsection 3.3.3, here we include the flexibility of the spacecraft structures in the attitude dynamics, therefore the mathematical model is given by (2.26), (2.38), (2.68), and (2.64). The spacecraft is modeled as a central rigid body with known inertia J_0 to which four flexible solar panels are attached. The upper bound of the satellite's inertia tensor $\overline{J}$ is given by the configuration in which the panels are fully deployed. Therefore, the upper bound $\overline{J}$ is actually the true inertia implemented in numerical simulations. In addition, the flexibility of the solar panels is modeled as described in Subsection 2.2.3, and the results of the FEM analysis are in Appendix A. Instead, the control algorithm is given by (3.86) and (3.87), and the control gains are tuned according to (3.99) and (3.102), which ensure to maneuver the spacecraft with uncertain J without saturating the RWs according to the discussion in Subsection 3.3.3. Numerical simulations are performed to confirm that this tuning avoids actuator saturation whilst dampening the oscillations due to the coupling between the flexible dynamics and attitude dynamics. The parameters of the dynamics system are listed in Table 5.4, whilst the control parameters and the actuation systems are in Table 5.5.

Table 5.4 Parameters of the maneuver and of the dynamics system

Nominal inertia:	$J_0 = \begin{bmatrix} 22 & 0 & 0 \\ 0 & 17 & 0 \\ 0 & 0 & 24 \end{bmatrix}$ kg m^2
Upper bound inertia:	$\overline{J} = \begin{bmatrix} 24 & 0 & 0 \\ 0 & 23.5 & 0 \\ 0 & 0 & 26 \end{bmatrix}$ kg m^2
Stiffness matrix:	$K = \begin{bmatrix} 0.79 & 0 & 0 \\ 0 & 11.93 & 0 \\ 0 & 0 & 30.36 \end{bmatrix}$
Scaling parameter for damping matrix ($C = \gamma K$)	$\gamma = 1.5 \cdot 10^{-3}$
Coupling matrix (panels 1 and 3)	$\delta_{13}^T = \begin{bmatrix} 0 & -0.26 & 0 \\ 0 & 0 & 0 \\ 1.77 & 0 & 0.97 \end{bmatrix}$
Coupling matrix (panels 2 and 4)	$\delta_{24}^T = \begin{bmatrix} 0.48 & 0 & -0.04 \\ 0 & 0 & 0 \\ 0 & 0.19 & 0 \end{bmatrix}$

Table 5.5 Parameters of the controller and of the actuation system

Controller	$\lambda = [1.83,\ 2.13,\ 1.84] \cdot 10^{-2}$
	$k = 2 \cdot 10^{-3}$
	$\overline{\sigma} = 10^{-4}$
Actuation system	$\overline{\tau} = 5 \cdot 10^{-3}$ N m
	$\overline{h_{\text{rw}}} = 0.12$ kg$\frac{\text{m}^2}{\text{s}}$

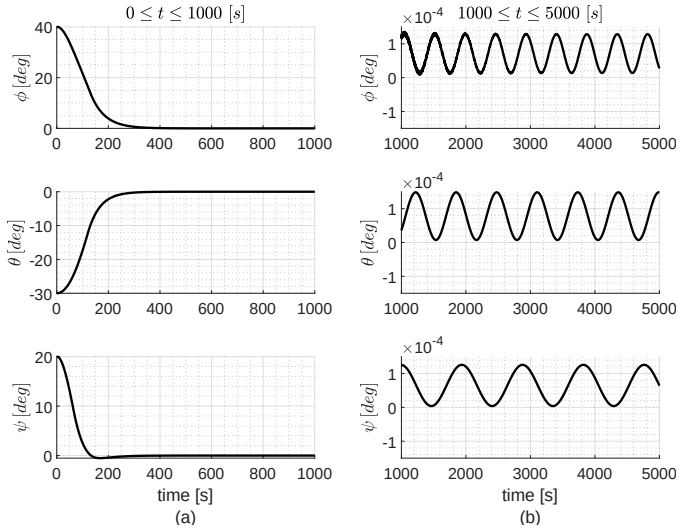

Fig. 5.22 Euler angles: attitude maneuver (a) and residual pointing error (b) in BLFOSM with parametric uncertainties

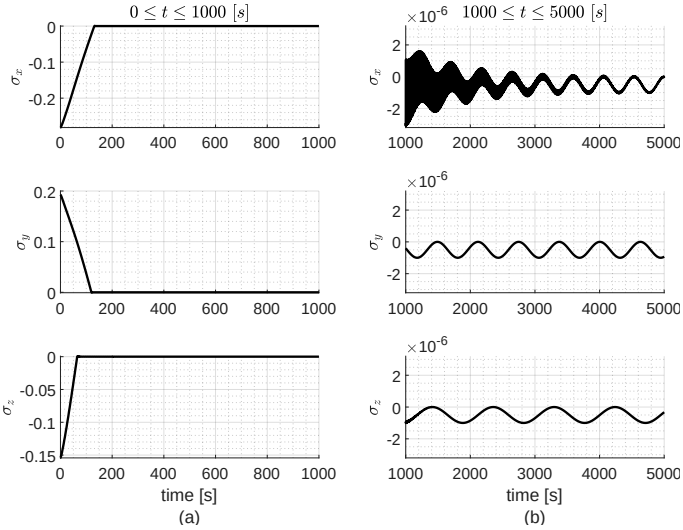

Fig. 5.23 Sliding variable in reaching phase (a) and in sliding phase (b) in BLFOSM with parametric uncertainties

Figure 5.23 shows that the controller succeed in driving the dynamic system to the set $|\sigma| \leq \overline{\sigma}$, despite the control law (3.86), (3.87) is built using the inertia J_0, which is different from the true inertia of the satellite J. As a result, the orientation of the satellite is steered around the zero pointing error as shown in Figure 5.22. Coupling with flexible dynamics induces oscillations on ϕ and, more evident in the respective Figure 5.23b, on σ_x. However, these are damped until they cancel out.

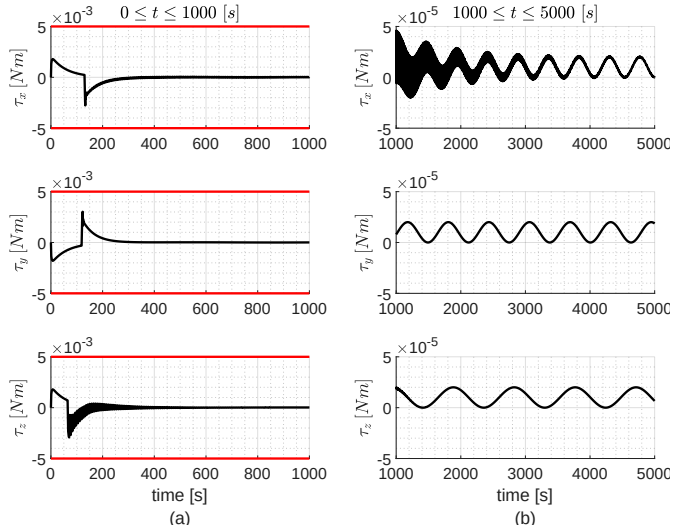

Fig. 5.24 Control torque during first 1000 seconds (a) and last 4000 seconds (b) in BLFOSM with parametric uncertainties

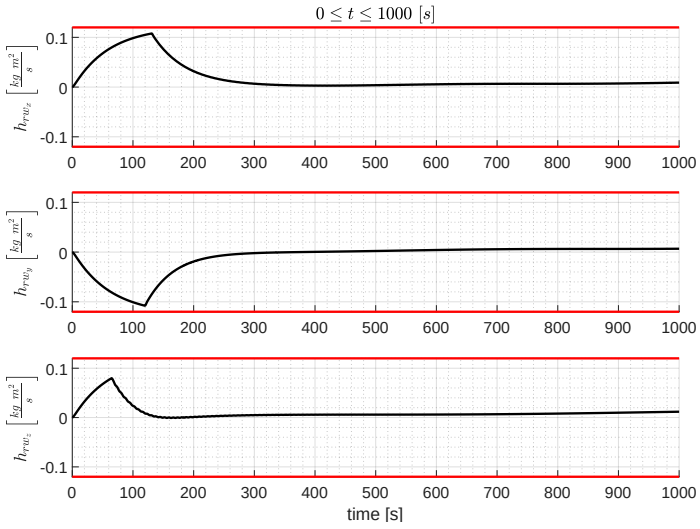

Fig. 5.25 Angular momentum of RWs in BLFOSM with parametric uncertainties

Figures 5.24 and 5.25 show that the controller avoids actuators saturation whilst completing the attitude maneuver. Some oscillations can be observed in the control input due to the coupling with flexible dynamics, however these are damped until they cancel out.

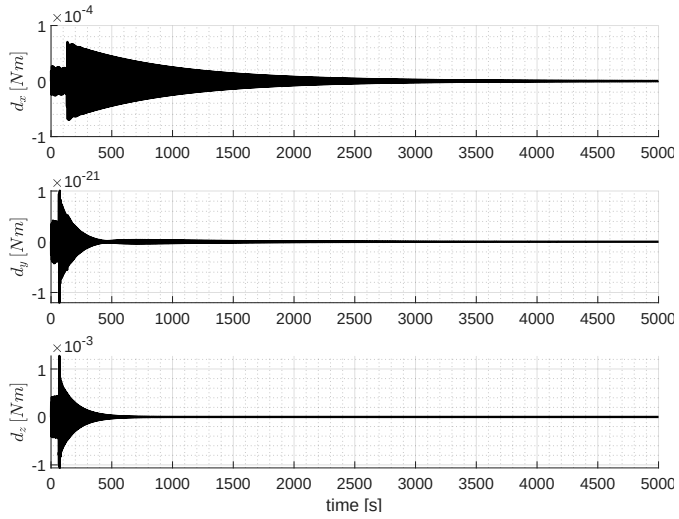

Fig. 5.26 Disturbance torque due to flexibility in BLFOSM with parametric uncertainties

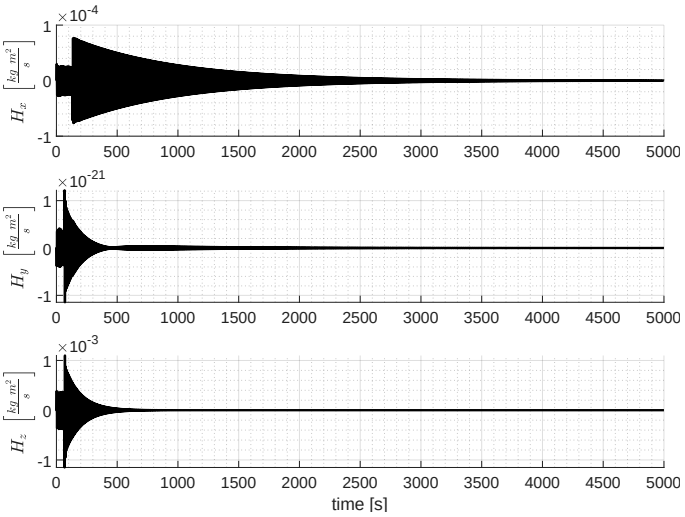

Fig. 5.27 Angular momentum due to flexibility in BLFOSM with parametric uncertainties

Figure 5.26 shows the disturbance torque due to the flexibility of the solar panels. It can be observed that this disturbance acts mainly on the x, z-axes of the satellite, while the y-axis is basically free of disturbance. This result is congruent with the configuration of the panels and the flexible modes included in the model. In fact, the latter relate to flexible rotations of the solar panels around the axes x and z of the spacecraft as shown in Appendix A. The magnitude of this disturbance torque is especially relevant during the attitude manoeuvre, congruent with the coupling whereby the flexible dynamics has as a forcing term proportional to the derivative of the angular velocity $\dot{\omega}$ (Eq. 2.64). After that, the disturbance cancels along with

the flexible oscillations, which are damped. In addition, the angular momentum introduced into the system by the flexible dynamics (Figure 5.27) has the same trend as the torque in Figure 5.26. This is congruent with the mathematical model used, where the flexible disturbance torque is $\dot{d}_{\text{flex}} = H_{\text{flex}}$.

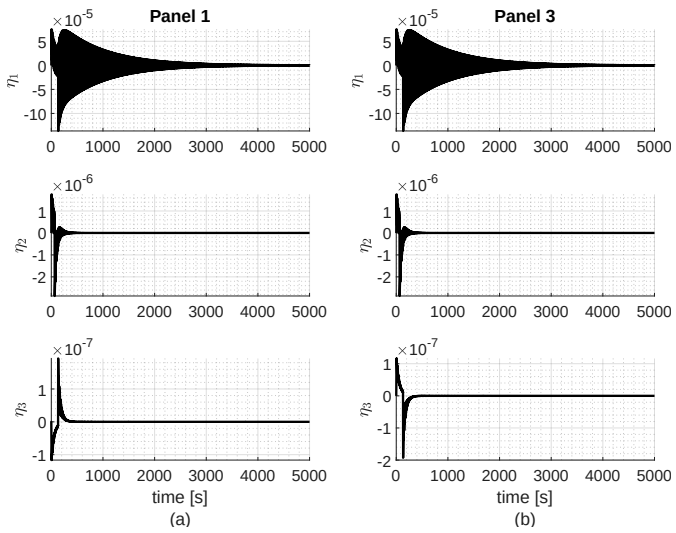

Fig. 5.28 Amplitude of the flexible modes of panels 1 (a) and 3 (b) in BLFOSM with parametric uncertainties

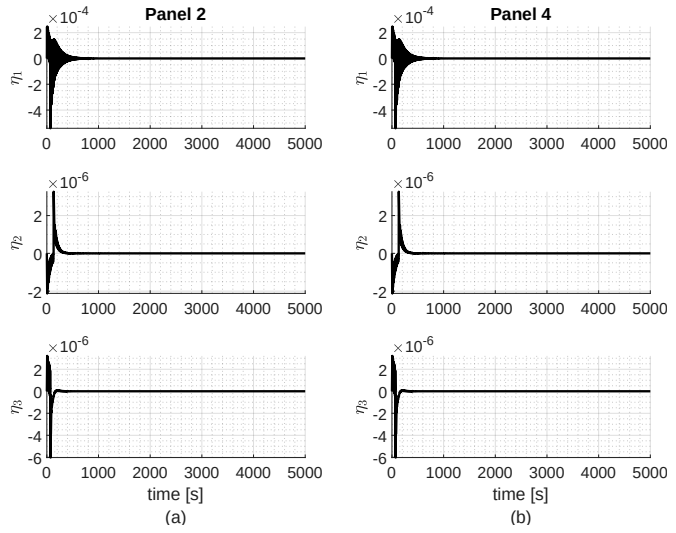

Fig. 5.29 Amplitude of the flexible modes of panels 2 (a) and 4 (b) in BLFOSM with parametric uncertainties

Figures 5.28 and 5.29 shows the trend of the amplitudes of the solar panels flexible modes, in particular η_1 and η_3 are related to the first and second bending modes respectively, while η_2 describes the first torsional mode. It can be seen that both the amplitude and duration of the oscillations decrease from η_1 to η_3, which is congruent with the energy associated with each mode (Table A.2 in Appendix A). Furthermore, the second bending mode of the structure causes panels 1 and 3 to flex asymmetrically, while panels 2 and 4 flex symmetrically (Figure A.5 in Appendix A). The asymmetrical bending of panels 1 and 3, given the chosen configuration, balances the disturbance torques caused by the two panels. This is confirmed by the fact that η_3 in Figure 5.28(a) is mirrored with respect to η_3 in Figure 5.28(b). In fact, given $\delta_{13}^T(:,3)$ the third column of δ_{13}^T, $\eta_{3_{p1}}$ and $\eta_{3_{p3}}$ the amplitude of the second bending mode for panels 1 and 3, respectively, the global disturbance torque resulting from the second bending mode of panels 1 and 3 is given by $\delta_{13}^T(:,3)\cdot(\ddot{\eta}_{3_{p1}}+\ddot{\eta}_{3_{p3}})$, which is null for $\ddot{\eta}_{3_{p1}}=-\ddot{\eta}_{3_{p3}}$.

5.4 The novel adaptive BLFOSM algorithm for spacecraft attitude control - results

This section details the simulation scenario introduced in Subsection 4.3.1 and provides the results of the numerical simulations performed in *Matlab* environment. The simulations are carried out with a sampling step of 0.01 s and the solver is *ode4*. The simulation scenario is the same as in the Section 5.3, so we want to study an inertial pointing manoeuvre with a flexible satellite, and the parameters for both are the same as in Table 5.4. Here, we apply the adaptive BLFOSM control algorithm (4.34), (4.35), (4.37)-(4.39), whose parameters are in Table 5.6. According to the theoretical, this adaptive controller should decrease the reaching time and, possibly, increase the tracking accuracy with respect to the classical BLFOSM used in the previous section, that was given by (3.86), (3.87), and with the control gains as in Table 5.5. In order to certify the theoretical, numerical simulations are performed and the results are compared with those obtained in previous section. As it is shown in Table 5.6, the initial λ_0 value for the adaptive BLFOSM is set equal to the constant λ value of the classical BLFOSM. This choice is not the best one from an application point of view, as to reduce the reaching time as much as possible it would be necessary to take an initial value of λ_0 so that the sliding surface is as

close as possible to the initial conditions of the system. So, in this case the optimal choice would be $\lambda_0 = \underline{\lambda}$ since the initial angular velocity is $\omega_0 = 0$. However, the choice we made on λ_0 allows us to prove by numerical simulations what has already been proved mathematically by Theorem 4.1, i.e. the reduction of the reaching time guaranteed by the adaptive BLFOSM compared to the classical BLFOSM under the same initial conditions. Furthermore, we chose $\overline{\lambda}$ of the adaptive BLFOSM to be greater that the fixed λ of the classical BLFOSM to prove that this provides greater pointing precision.

Table 5.6 Parameters of the adaptive BLFOSM control algorithm

Control parameters	$\underline{\lambda} = 10^{-5}$
	$\overline{\lambda} = 10^{-1}$
	$\lambda_0 = [1.83,\ 2.13,\ 1.84] \cdot 10^{-2}$
	$c = 5 \cdot 10^{-3}$
	$G = -5$
	$\overline{\sigma} = 10^{-4}$
	$k = 10^{-3}$

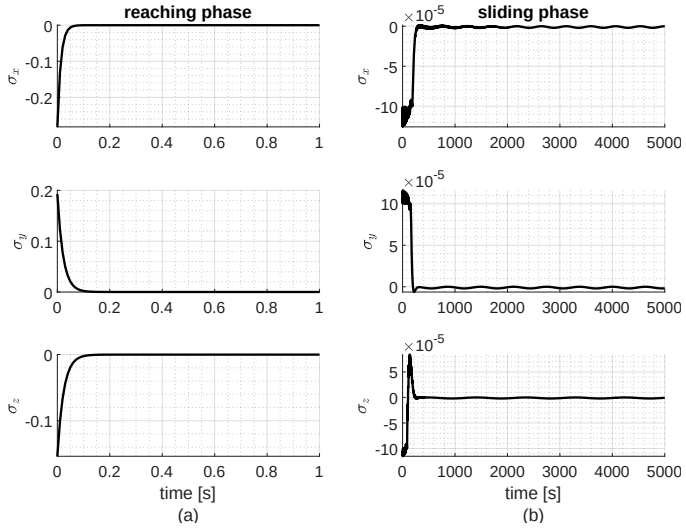

Fig. 5.30 Sliding variable evolution during reaching phase (a) and sliding phase (b) with the adaptive BLFOSM

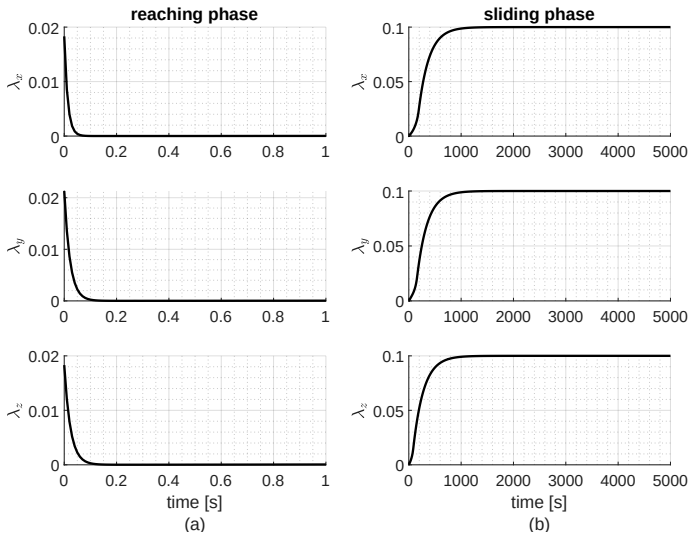

Fig. 5.31 Slope of the sliding surface evolution during reaching phase (a) and sliding phase (b) with the adaptive BLFOSM

Figure 5.30a shows that the adaptive BLFOSM guarantees the almost-elimination of the reaching phase, since σ converge to $[-\overline{\sigma},\ \overline{\sigma}]$ in about one second. This is achieved through the adaptation of λ, which is decreased by the adaptive mechanism over this stage (Figure 5.31a) to let the sliding surface rotates towards the initial states of the dynamic system. After, the adaptive mechanism adjust λ so that it converges to the desired value $\overline{\lambda}$ during the sliding phase (Figure 5.31b). Figure 5.30b shows that during this process σ remains within the set $[-\overline{\sigma},\ \overline{\sigma}]$, proving that the system does not lose the sliding mode during the rotation of the sliding surface. Below, the comparison between the results obtained with the adaptive BLFOSM and the results in previous section, obtained with the classical BLFOSM.

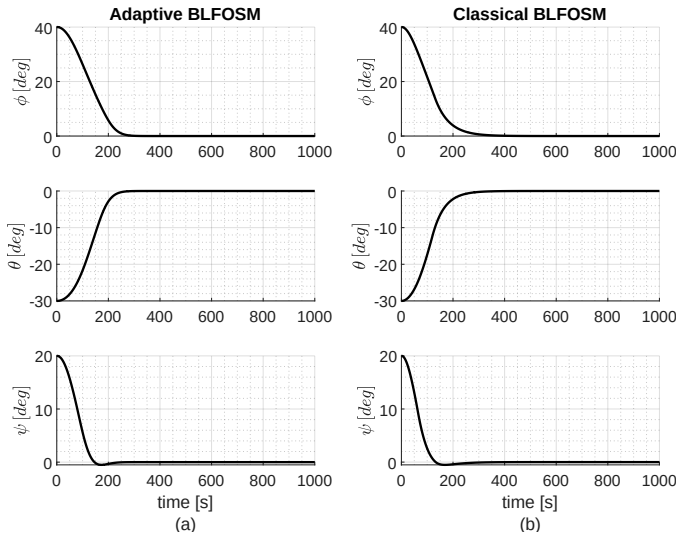

Fig. 5.32 Euler angles during the attitude maneuver with adaptive BLFOSM (a) and classical BLFOSM (b)

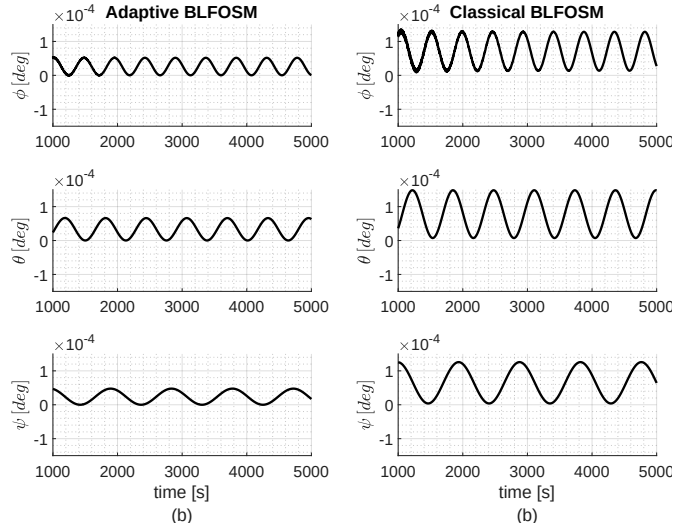

Fig. 5.33 Residual pointing error in Euler angles with adaptive BLFOSM (a) and classical BLFOSM (b)

The attitude manoeuvre is carried out without substantial differences between the two control algorithms as shown in Figure 5.32, where it can be seen that the adaptive BLFOSM is only slightly faster in reaching the vicinity of the null error. Instead, Figure 5.33 shows the better behaviour of the adaptive BLFOSM in terms of pointing accuracy, due to having selected $\overline{\lambda} > \lambda$ of the classical BLFOSM.

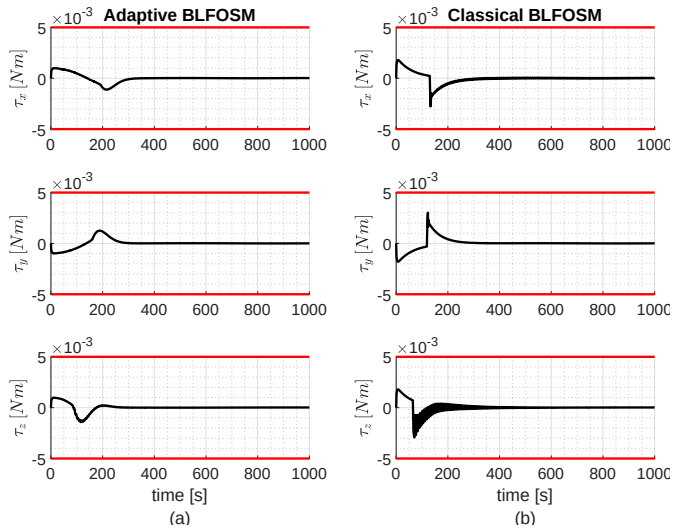

Fig. 5.34 Control torque during the first 1000 seconds with adaptive BLFOSM (a) and classical BLFOSM (b)

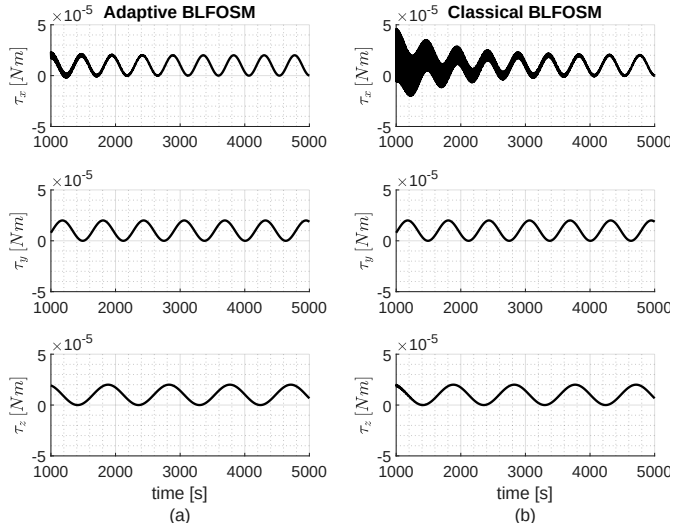

Fig. 5.35 Control torque during the last 4000 seconds with adaptive BLFOSM (a) and classical BLFOSM (b)

Both control algorithms succeed in avoiding torque saturation, but the adaptive BLFOSM algorithm seems to produce a smoother control signal relative to classical BLFOSM according to Figure 5.34, thus suitable to be implemented by actuators with slow dynamics. Also, the adaptive BLFOSM reduces the oscillations due to the coupling with flexible dynamics, how it can be seen in both Figures 5.34 and 5.35.

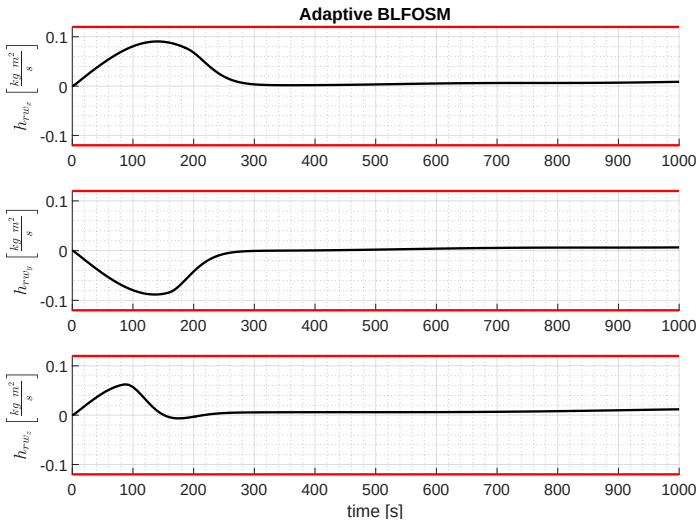

Fig. 5.36 Angular momentum of RWs with adaptive BLFOSM

Figure 5.36 shows that the adaptive BLFOSM succeed in avoiding angular momentum saturation of the wheels whilst completing the maneuver. With regard to the trend of the angular momentum stored in the wheels, there are no substantial differences between the two control algorithms. Therefore, a comparison with Figure 5.25 was not proposed as was done for the other quantities.

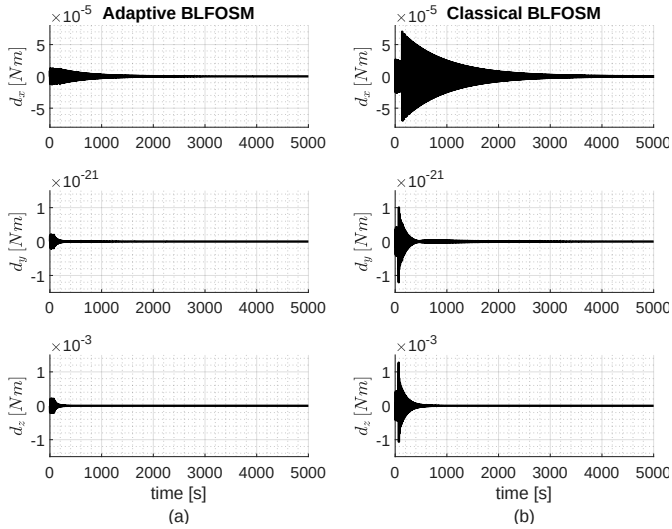

Fig. 5.37 Disturbance torque due to flexibility with adaptive BLFOSM (a) and classical BLFOSM (b)

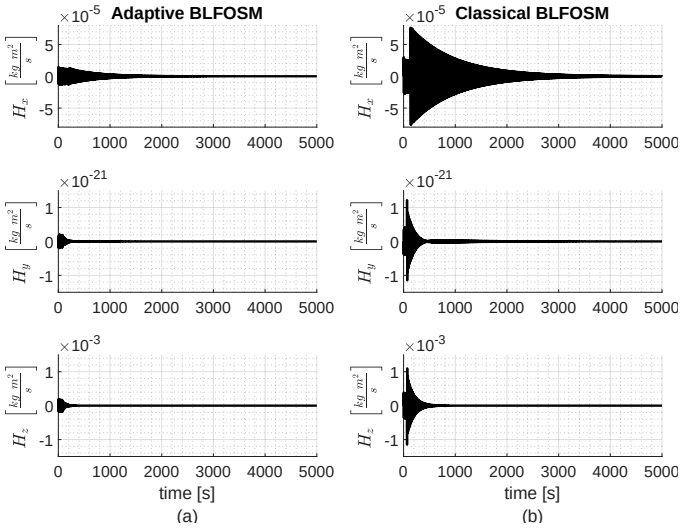

Fig. 5.38 Angular momentum due to flexibility with adaptive BLFOSM (a) and classical BLFOSM (b)

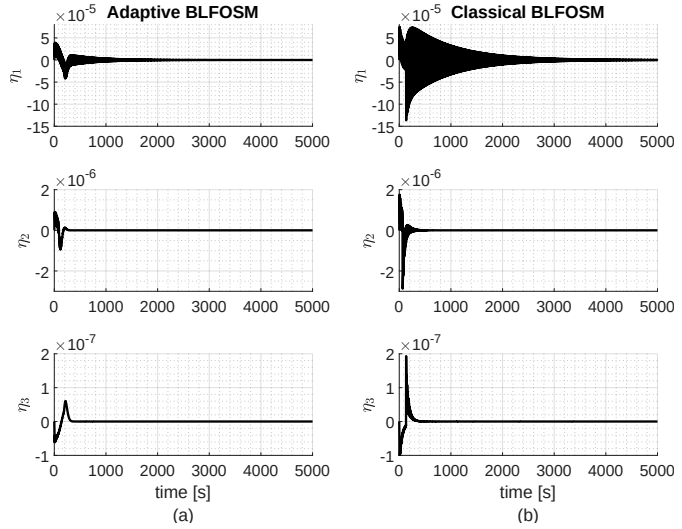

Fig. 5.39 Amplitude of the flexible modes of panel 1 with adaptive BLFOSM (a) and classical BLFOSM (b)

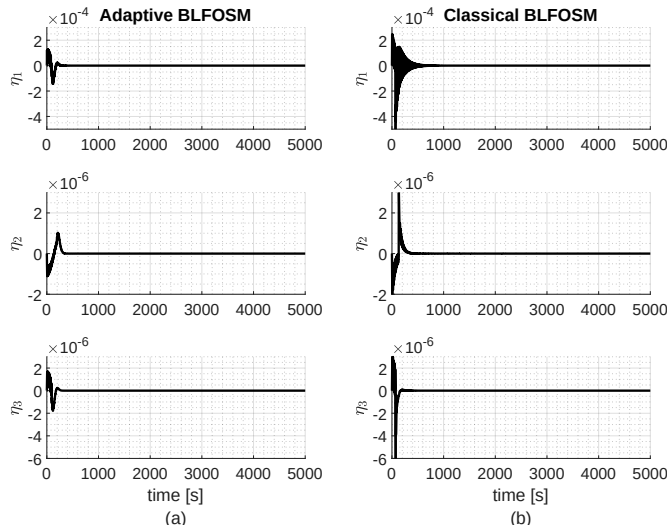

Fig. 5.40 Amplitude of the flexible modes of panel 2 with adaptive BLFOSM (a) and classical BLFOSM (b)

Figures 5.37 to 5.40 shows that the adaptive BLFOSM energizes the flexible dynamics less strongly than the classical BLFOSM. In fact, the amplitudes and durations of the oscillations are reduced concerning the disturbance torque (Figure 5.37), the extra angular momentum (Figure 5.38), and the amplitude of the flexible modes (Figures 5.39 and 5.40). Here, the amplitudes of the flexible modes for solar panels 3 and 4 are not shown in the figures, as it was seen in the previous section that they are equivalent to those for panels 1 and 2 respectively (see Figures 5.28 and 5.29).

5.5 Results for the novel adaptive BLFOSM algorithm for attitude control of DEMETER

This section details the simulation scenario introduced in Subsection 4.3.2 and provides the results of the numerical simulations performed in *Matlab/Simulink* environment. The simulations are carried out with a sampling step of 0.01 s and the solver is *ode4*. As discussed in Subsection 4.3.2, the objective is to realize an inertial pointing maneuver, stabilizing the DEMETER satellite for a wide range of initial conditions. The details of the DEMETER attitude dynamics can be found in [2], but differently from the model published here, the simulator provided to us by CNES and used in this thesis does not include the flexible modes of the satellite. The range

of initial conditions and desired orientation for the attitude maneuver are in Table 5.7. In this work, the attitude manoeuvre is attempted with three different control algorithms: the CNES control law (4.47)-(4.48) whose details are in [2], the classical BLFOSM (4.50)-(4.51), and the adaptive BLFOSM (4.50), (4.51), (4.35 with θ_{e_i} in place of $q_{e_{v_i}}$). The SMC algorithms are tuned as shown in Subsection 4.3.2, deriving the control parameters in Table 5.8. Montecarlo simulations are performed with 100 different values of the initial conditions, and the results are provided below.

Table 5.7 Parameters of the maneuver and of the DEMETER

Initial orientation:	$\Theta_0 = (\phi_0,\ \theta_0,\ \psi_0) \in [-\pi,\ \pi]$ deg
Desired orientation:	$\Theta^* = (\phi^*,\ \theta^*,\ \psi^*) = (0,\ 0,\ 0)$ deg
Initial angular rate:	$\omega_{0_x} \in [-1.6,\ 1.6] \cdot 10^{-3}\ \frac{\text{rad}}{\text{s}}$
	$\omega_{0_y} \in [-1.6,\ 1.6] \cdot 10^{-3}\ \frac{\text{rad}}{\text{s}}$
	$\omega_{0_z} \in [-1.1,\ 1.1] \cdot 10^{-3}\ \frac{\text{rad}}{\text{s}}$
Desired angular rate:	$\omega^* = (0,\ 0,\ 0)\ \frac{\text{rad}}{\text{s}}$
Initial angular momentum RWs:	$h_{\text{rw}_0} = (0,\ 0,\ 0)\ \text{kg}\frac{\text{m}^2}{\text{s}}$
Orbital disturbances:	$d = 10^{-6} + 3.1\ 10^{-5} \cdot \sin(10^{-4}t) + 1.5\ 10^{-5} \cdot \sin(2\ 10^{-4}t)$ N m
Inertia tensor:	$J = \begin{bmatrix} 30 & -3 & 0 \\ -3 & 30 & -2 \\ 0 & -2 & 40 \end{bmatrix}$ kg m^2
Torque max RWs:	$\overline{\tau} = 2 \cdot 10^{-3}$ N m
Angular momentum max RWs:	$\overline{h_{\text{rw}}} = 0.12\ \text{kg}\frac{\text{m}^2}{\text{s}}$

First, Table 5.9 indicates for each controller the number of simulations (out of the total of 100) in which the final pointing error is less than 0.04, which is the required accuracy according to [2]. The same table also provide the mean time response, i.e. the average of the times taken by each controller for the error to converge within the required range.

Table 5.8 Parameters of both the classical BLFOSM and the adaptive BLFOSM controllers

Classical BLFOSM	$\lambda = 0.05$
	$k = 10^{-4}$
	$\overline{\sigma} = 5 \cdot 10^{-5}$
Adaptive BLFOSM	$\underline{\lambda} = 10^{-5}$
	$\overline{\lambda} = 0.05$
	$\lambda_0 = \underline{\lambda}$
	$c = 3.5 \cdot 10^{-5}$
	$G = -3.5 \cdot 10^{-2}$
	$k = 10^{-4}$
	$\overline{\sigma} = 5 \cdot 10^{-5}$

Table 5.9 Results of Montecarlo simulations

	controller CNES	classical BLFOSM	adaptive BLFOSM
Successful simulations:	100	0	96
Mean time response [s]:	4151	-	2683

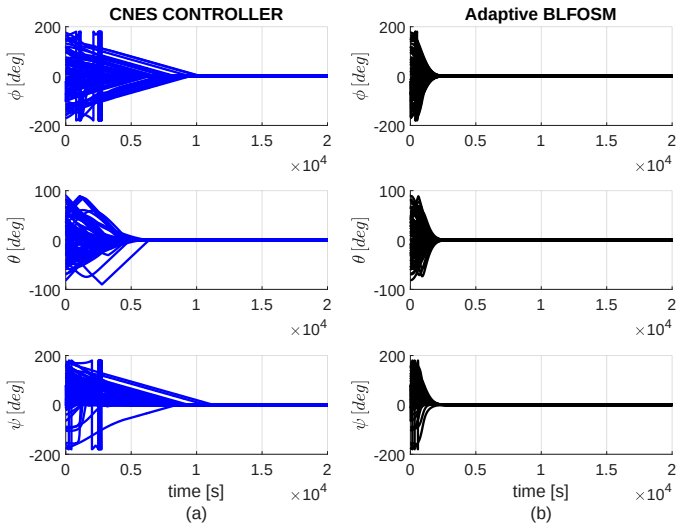

Fig. 5.41 Euler angles during the attitude maneuver with CNES controller (a) and adaptive BLFOSM (b) in DEMETER application

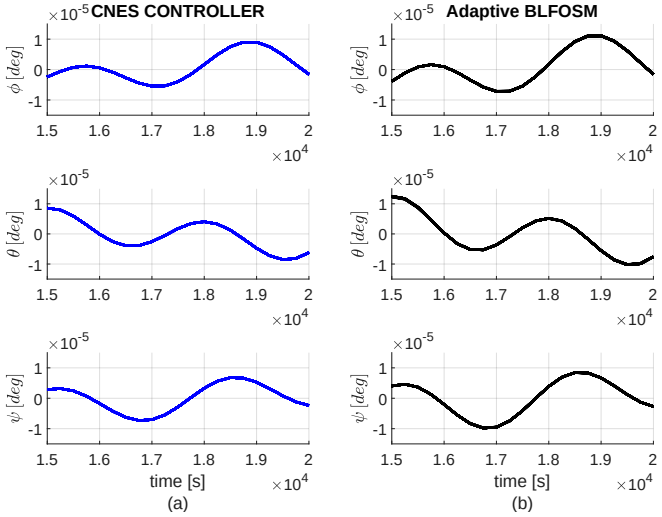

Fig. 5.42 Residual pointing error in Euler angles with CNES controller (a) and adaptive BLFOSM (b) in DEMETER application

Figure 5.41 confirms that the adaptive BLFOSM is faster than the CNES controller in completing the attitude manoeuvre, which is also evident from the mean time response in Table 5.9. In addition, Figure 5.42 shows that the two controllers give the same pointing accuracy, certifying the validity of the tuning strategy used for the adaptive BLFOSM. Evidently, Figures 5.9 and 5.42 have been cleaned of the four simulations in which the adaptive BLFOSM algorithm failed to converge DEMETER to the desired attitude, so as not to affect the readability of the figures.

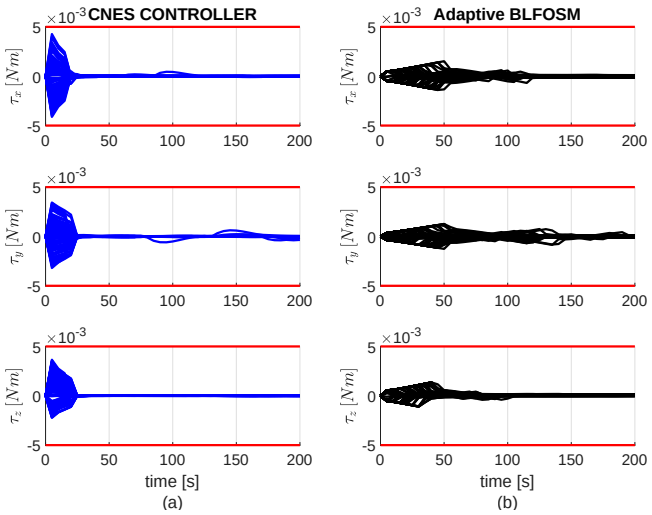

Fig. 5.43 Control torque during first 200 seconds with CNES controller (a) and adaptive BLFOSM (b) in DEMETER application

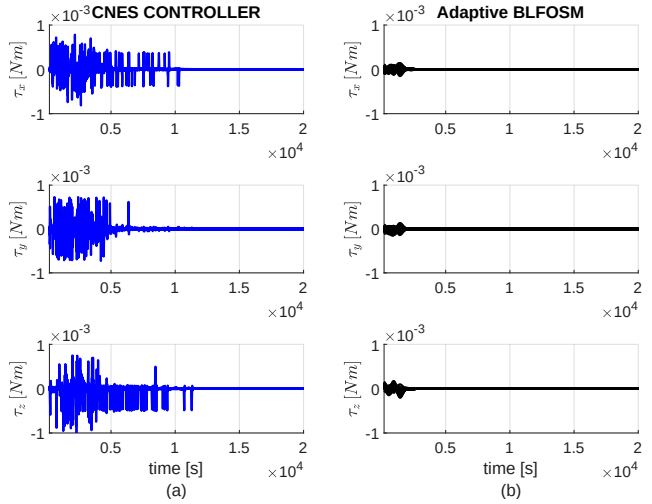

Fig. 5.44 Control torque during the rest of the maneuver with CNES controller (a) and adaptive BLFOSM (b) in DEMETER application

Figure 5.43 shows that both controllers avoid torque saturation of RWs during the first stage of the maneuver, where the control action is usually highest. Furthermore, the output of the adaptive BLFOSM controller has lower torque peaks than the CNES controller. This is also true during the rest of the maneuver, where the control signal of the adaptive BLFOSM is smoother that the one of the CNES controller according to Figure 5.44.

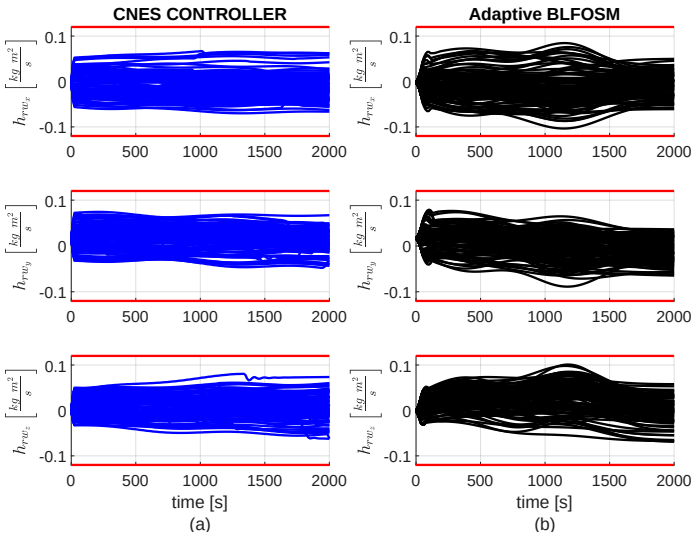

Fig. 5.45 Angular momentum of RWs during first 2000 seconds with CNES controller (a) and adaptive BLFOSM (b) in DEMETER application

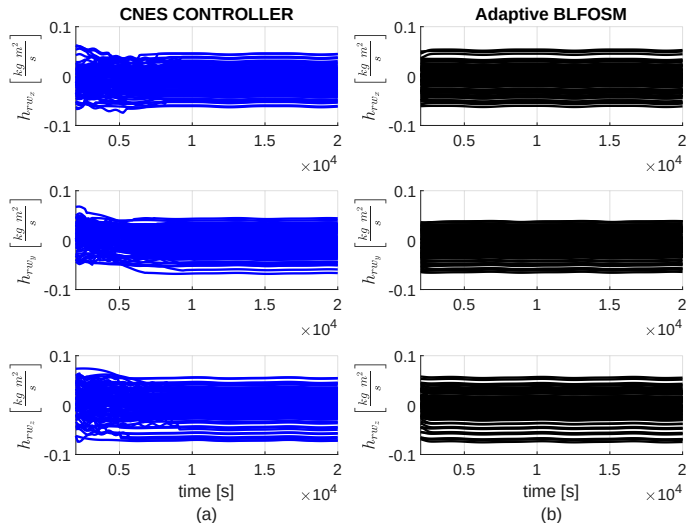

Fig. 5.46 Angular momentum of RWs during the rest of the maneuver with CNES controller (a) and adaptive BLFOSM (b) in DEMETER application

Figure 5.45 shows that both controllers avoid to saturate the angular momentum of RWs during the the first stage of the maneuver, which is the most critical as for the torque. The BLFOSM pushes more angular momentum into the wheels, which is normal since it is faster than the CNES controller in manoeuvring the satellite. Then, Figure 5.46 shows the development of angular momentum stored into the wheels for the rest of the maneuver. The trend is similar in both cases, which is normal since

this residual is due to the initial angular momentum (ω_0) and the action of orbital disturbances.

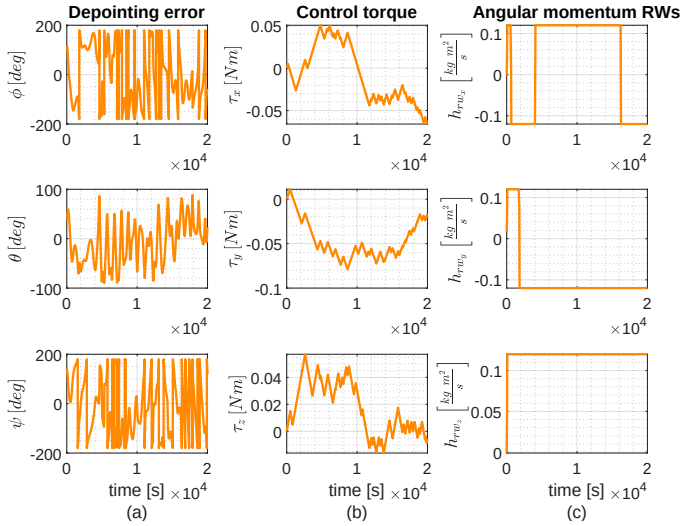

Fig. 5.47 The results of one simulation with classical BLFOSM: pointing error (a), control torque (b), and angular momentum of the RWs (c) in DEMETER application

Finally, regarding the classical BLFOSM, Table 5.9 shows that it is not able to steer the DEMETER attitude for any of the initial conditions considered. Indeed, for large initial pointing errors the classical BLFOSM incurs actuator saturations that cause the system to lose stability. This is depicted in Figure 5.47, which shows one of the failed numerical simulations with this controller. In fact, it can be seen that the angular momentum saturates (Figure 5.47c) as soon as soon as the manoeuvre starts, so that the actuators cannot follow the controller input (Figure 5.47b), which conversely demands an increasingly high torque causing the satellite to lose controllability. In order to show this effect, the controller output is shown in Figure 5.47b without including actuator saturations, which are instead applied in the simulator.

Chapter 6

Conclusions

A key aspect of a successful space mission is the proper orientation of the spacecraft during each phase of the mission itself. All the satellite's on-board systems contribute directly or indirectly to this, but the management of the spacecraft attitude is mostly the responsibility of the Guidance,Navigation and Control (GNC), actuation, and attitude sensors systems. From a practical point of view, these above are closely related to each other, however, from the implementation point of view, the sensors are usually connected to the navigation algorithms (i.e. Kalman filters) and the actuators to the control algorithms. Indeed, the sensors and the navigation algorithms together estimate the satellite's true attitude, while the actuators and the control algorithms together orient the satellite according to the reference provided by the guidance function. The global attitude error is consequently a function of both the estimation and control errors, however, the two algorithms can be designed separately as done in most space missions.

This is also the approach in this thesis, in which the focus was placed on algorithms for the attitude control system, omitting the navigation function. Thus, neither sensor models nor navigation algorithms are included in the attitude dynamics simulator that was built during the doctoral project. Consequently, for the design of the control algorithms we assume that the input of the controller is the true (not estimated) orientation of the satellite, and this is then replicated in the numerical simulations where the plant output (quaternions and angular velocities) directly enters the controller.

After that, the controller's output torque must be exerted by the actuation system. However, attitude control actuators have limited actuation power and this has been taken into account in both control algorithms design and numerical simulations. In

particular, we considered carrying three Reaction Wheels (RWs), aligned with the satellite's three central axes of inertia. This allowed us to realise active three-axis attitude control and to formulate it as three second-order systems with a single input. RWs suffer from torque and angular momentum saturation, and this is just one of the critical issues in attitude control algorithms design, beyond the non-linearity of the system, the orbital disturbances, the parametric uncertainties, and the flexibility of structures.

Given the harsh conditions the ACS works with, robust Variable Structure Control (VSC) algorithms with sliding mode were chosen as the basis for it. In this field, the first problem addressed was the typical high-frequency oscillations in closed-loop dynamics caused by Sliding Mode Controller (SMC). Hence, two chattering elimination techniques, namely the Boundary-Layer First Order Sliding Mode (BLFOSM) and Super-Twisting (STW) algorithms, were compared for attitude control applications. The results showed that BLFOSM is more effective than STW at completely eliminating chattering, especially at low refresh rates. Moreover, the BLFOSM proved to be less computationally expensive and tuning BLFOSM control gains is more intuitive compared to regulating the STW. In addition, the BLFOSM showed a more uniform response than the STW to changing initial conditions and system parameters. Hence, it was decided to study BLFOSM more extensively in the course of the PhD.

The next step was to design the BLFOSM controller so that the torque generated therein would not saturate the RWs in manoeuvring the satellite. For this purpose, it was developed a tuning strategy that determines the values of the control gains based on the characteristics of both the actuation system and the inertia of the satellite. Moreover, this tuning strategy was first proposed assuming that the satellite's inertia was known, after it was modified to allow for uncertainties in the inertia as well. Numerical simulations showed the validity of the tuning strategy, as the control laws successfully manoeuvre the satellite without saturating the RWs and damping oscillations due to coupling with flexible dynamics.

The next challenge regarding the BLFOSM algorithm was to find a way to shorten the duration of the reaching phase, considering a wide range of initial angular velocities, and shortening the procedure of adjusting the control gains, while avoiding actuators saturation. For this purpose, we developed a rotating sliding surface with a new approach based on an adaptive law. The innovative adaptive law rotates the sliding surfaces towards the states of the system as long as they are outside the boundary

layer. After that, with the system converging towards zero error in the sliding phase, the adaptive law rotates the sliding surface towards a predetermined final position that guarantees high pointing accuracy. The results obtained with the new adaptive BLFOSM have shown the combination of adaptive control and SMC to be very promising, alleviating the issues mentioned above and, in addition, reducing the excitation of the flexible dynamics with respect to the classical BLFOSM.

Finally, the adaptive BLFOSM controller developed was tested in the DEMETER orbital simulator, showing by Monte Carlo simulations that this controller is able to replicate the switching control law from the CNES and actually implemented on the on-board algorithms. In fact, the adaptive BLFOSM is able to converge the DEMETER attitude with high accuracy and for a wide range of initial conditions, without saturating the actuators. In contrast, the classical BLFOSM failed this task.

The design of the sliding mode control algorithms was conducted based on the simplified mathematical model of attitude dynamics. Stability proofs for the developed control algorithms are provided under the same assumptions used to derive the simplified mathematical models of attitude dynamics, while numerical simulations validated the controllers under more general simulation scenarios. Apart from the DEMETER simulations, the control laws for the other case studies were tested on a 3-degree-of-freedom attitude dynamics simulator built during the doctoral project in *Matlab/Simulink* environment. The simulator includes the rigorous equations of dynamics and attitude kinematics, the control laws, the RWs model, and the external disturbances. In addition, the attitude dynamics equations were implemented both considering a completely rigid satellite and with flexible appendages as in Appendix A. In the latter case, the simulator also includes the equations of flexible dynamics for the appendages.

Finally, some insights for future developments of this project are provided below. Given the promising results obtained with adaptive SMC, the combination of adaptive control and SMC may be worthy of further study. In this project, it was observed that it is quite easy to set the gains of the adaptive SMC through trial and error while managing to avoid actuator saturations, however, it would be of great interest to find mathematical correlations to guide tuning in this regard. Another interesting proposal is to develop adaptive sliding surfaces other than linear and also for other types of SMC algorithms.Finally, although perhaps not applicable to satellite attitude control, it would be worth investigating adaptive laws for sliding surfaces in higher order systems.

References

[1] Y. Shtessel, C. Edwards, L. Fridman, and A. Levant. Second-order sliding mode controllers and differentiators. In *Sliding Mode Control and Observation*, pages 143–182. Springer New York, New York, NY, 2014.

[2] C. Pittet. Demeter: A benchmark for robust analysis and control of the attitude of flexible micro satellites. *IFAC Proceedings Volumes*, 39:661–666, 07 2006.

[3] P. Crouch. Spacecraft attitude control and stabilization: Applications of geometric control theory to rigid body models. *IEEE Transactions on Automatic Control*, 29(4):321–331, 1984.

[4] J. T. Y. Wen and K. Kreutz-Delgado. The attitude control problem. *IEEE Transactions on Automatic Control*, 36(10):1148–1162, 1991.

[5] C. I. Byrnes and A. Isidori. On the attitude stabilization of rigid spacecraft. *Automatica*, 27(1):87–95, 1991.

[6] P. Morin, C. Samson, J. B. Pomet, and Z. P. Jiang. Time-varying feedback stabilization of the attitude of a rigid spacecraft with two controls. *Systems & Control Letters*, 25(5):375–385, 1995.

[7] F. Lizarralde and J. T. Wen. Attitude control without angular velocity measurement: a passivity approach. *IEEE Transactions on Automatic Control*, 41(3):468–472, 1996.

[8] O. Egeland and J. M. Godhavn. Passivity-based adaptive attitude control of a rigid spacecraft. *IEEE Transactions on Automatic Control*, 39(4):842–846, 1994.

[9] B. Wie and P. M. Barba. Quaternion feedback for spacecraft large angle maneuvers. *Journal of Guidance, Control, and Dynamics*, 8(3):360–365, 1985.

[10] P. Tsiotras. Stabilization and optimality results for the attitude control problem. *Journal of Guidance, Control, and Dynamics*, 19(4):772–779, 1996.

[11] S.M. Joshi, A.G. Kelkar, and J.T.-Y. Wen. Robust attitude stabilization of spacecraft using nonlinear quaternion feedback. *IEEE Transactions on Automatic Control*, 40(10):1800–1803, 1995.

[12] E. Capello, E. Punta, F. Dabbene, G. Guglieri, and R. Tempo. Sliding-mode control strategies for rendezvous and docking maneuvers. *Journal of Guidance, Control, and Dynamics*, 40(6):1481–1487, 2017.

[13] D. T. Stansbery and J. R. Cloutier. Position and attitude control of a spacecraft using the state-dependent Riccati equation technique. In *Proceedings of the 2000 American Control Conference*, volume 3, pages 1867–1871. IEEE, 2000.

[14] S. W. Kim, S. Y. Park, and C. Park. Spacecraft attitude control using neuro-fuzzy approximation of the optimal controllers. *Advances in Space Research*, 57(1):137–152, 2016.

[15] M. Malekzadeh, A. Naghash, and H. A. Talebi. A robust nonlinear control approach for tip position tracking of flexible spacecraft. *IEEE Transactions on Aerospace and Electronic Systems*, 47(4):2423–2434, 2011.

[16] R. Chai, A. Tsourdos, A. Savvaris, S. Chai, Y. Xia, and C. L. P. Chen. Review of advanced guidance and control algorithms for space/aerospace vehicles. *Progress in Aerospace Sciences*, 122:100696, 2021.

[17] P. Acquatella, W. Falkena, E. J. Van Kampen, and Q. P. Chu. Robust nonlinear spacecraft attitude control using incremental nonlinear dynamic inversion. In *AIAA Guidance, Navigation, and Control Conference*, 2012-4623.

[18] E. Weerdt, E. J. Kampen, D. Gemert, Q. P. Chu, and J. A. Mulder. Adaptive nonlinear dynamic inversion for spacecraft attitude control with fuel sloshing. In *AIAA Guidance, Navigation and Control Conference and Exhibit*, 2008-7162.

[19] M. Nazari, E. A. Butcher, and A. K. Sanyal. Spacecraft attitude fractional feedback control using rotation matrices and exponential coordinates. *Journal of Guidance, Control, and Dynamics*, 41(10):2185–2198, 2018.

[20] Z. Ismail, R. Varatharajoo, and Y. C. Chak. A fractional-order sliding mode control for nominal and underactuated satellite attitude controls. *Advances in Space Research*, 66(2):321–334, 2020.

[21] Z. Ma, Z. H. Zhu, and G. Sun. Fractional-order sliding mode control for deployment of tethered spacecraft system. *Proceedings of the Institution of Mechanical Engineers, Part G: Journal of Aerospace Engineering*, 233(13):4721–4734, 2019.

[22] R. Kristiansen, P. J. Nicklasson, and J. T. Gravdahl. Satellite attitude control by quaternion-based backstepping. *IEEE Transactions on Control Systems Technology*, 17(1):227–232, 2009.

[23] I. Ali, G. Radice, and J. Kim. Backstepping control design with actuator torque bound for spacecraft attitude maneuver. *Journal of Guidance, Control, and Dynamics*, 33(1):254–259, 2010.

[24] F. Pozo, F. Ikhouane, and J. Rodellar. Numerical issues in backstepping control: Sensitivity and parameter tuning. *Journal of the Franklin Institute*, 345(8):891–905, 2008.

[25] W. Luo, Y. C. Chu, and K. V. Ling. H-infinity inverse optimal attitude-tracking control of rigid spacecraft. *Journal of Guidance, Control, and Dynamics*, 28(3):481–494, 2005.

[26] M. Xin, S. N. Balakrishnan, and D. Stansbery. Spacecraft position and attitude control with Theta-D technique. In *42nd AIAA Aerospace Sciences Meeting and Exhibit*, 2004-540.

[27] L. Guarnaccia, R. Bevilacqua, and S. P. Pastorelli. Suboptimal LQR-based spacecraft full motion control: Theory and experimentation. *Acta Astronautica*, 122:114–136, 2016.

[28] F. L. Markley and J. L. Crassidis. Matrices, vectors, frames, transforms. In *Fundamentals of Spacecraft Attitude Determination and Control*, chapter 3. Springer New York, New York, NY, 2014.

[29] E. Canuto, C. Novara, D. Carlucci, C. P. Montenegro, and L. Massotti. Attitude kinematics: Modeling and feedback. In *Spacecraft Dynamics and Control: The Embedded Model Control Approach*, Aerospace Engineering, chapter 6. Butterworth-Heinemann, Oxford, UK, 2018.

[30] A. H. De Ruiter, C. Damaren, and J. R. Forbes. Kinematics. In *Spacecraft Dynamics and Control: an Introduction*, chapter 1. John Wiley & Sons, Chichester, UK, 2013.

[31] Y. Yang. Rotational sequences and quaternion. In *Spacecraft Modeling, Attitude Determination, and Control Quaternion-based Approach: Quaternion-Based Approach*, chapter 3. CRC Press, Boca Raton, FL, 2019.

[32] E. Canuto, C. Novara, D. Carlucci, C. P. Montenegro, and L. Massotti. Attitude dynamics: Modeling and control. In *Spacecraft Dynamics and Control: The Embedded Model Control Approach*, Aerospace Engineering, chapter 7. Butterworth-Heinemann, Oxford, UK, 2018.

[33] A. H. De Ruiter, C. Damaren, and J. R. Forbes. Rigid body dynamics. In *Spacecraft Dynamics and Control: an Introduction*, chapter 2. John Wiley & Sons, Chichester, UK, 2013.

[34] Y. Yang. Spacecraft dynamics and modeling. In *Spacecraft Modeling, Attitude Determination, and Control Quaternion-based Approach: Quaternion-Based Approach*, chapter 4. CRC Press, Boca Raton, FL, 2019.

[35] P. W. Fortescue and G. G. Swinerd. Dynamics of spacecraft. In *Spacecraft Systems Engineering*, chapter 3. John Wiley & Sons, Ltd, Chichester, UK, 4th edition, 2011.

[36] A. H. De Ruiter, C. Damaren, and J. R. Forbes. Disturbance torques on a spacecraft. In *Spacecraft Dynamics and Control: an Introduction*, chapter 12. John Wiley & Sons, Chichester, UK, 2013.

[37] E. Canuto, C. Novara, D. Carlucci, C. P. Montenegro, and L. Massotti. The environment: Perturbing forces and torques. In *Spacecraft Dynamics and Control: The Embedded Model Control Approach*, Aerospace Engineering, chapter 4. Butterworth-Heinemann, Oxford, UK, 2018.

[38] A. H. De Ruiter, C. Damaren, and J. R. Forbes. *Spacecraft Dynamics and Control: an Introduction*. John Wiley & Sons, Chichester, UK, 2013.

[39] C. Pukdeboon, A. S. I. Zinober, and M. W. L. Thein. Quasi-continuous higher order sliding-mode controllers for spacecraft-attitude-tracking maneuvers. *IEEE Transactions on Industrial Electronics*, 57(4):1436–1444, 2009.

[40] K. Ma. Comments on "quasi-continuous higher order sliding-mode controllers for spacecraft-attitude-tracking maneuvers". *IEEE Transactions on Industrial Electronics*, 60(7):2771–2773, 2012.

[41] P. W. Likins. Dynamics and control of flexible space vehicles. Technical Report JPL-TR-32-1329-REV-1, Jet Propulsion Laboratory, Pasadena, CA, January 1970.

[42] A. D'Ortona. Design of sliding mode techniques for a CMG-based testbed attitude control system. Master's thesis, Politecnico di Torino, April 2021.

[43] P. W. Likins and G. E. Fleischer. Results of flexible spacecraft attitude control studies utilizing hybrid coordinates. *Journal of Spacecraft and Rockets*, 8(3):264–273, 1971.

[44] S. Di Gennaro. Output stabilization of flexible spacecraft with active vibration suppression. *IEEE Transactions on Aerospace and Electronic Systems*, 39(3):747–759, 2003.

[45] S. Ding and W. X. Zheng. Nonsmooth attitude stabilization of a flexible spacecraft. *IEEE Transactions on Aerospace and Electronic Systems*, 50(2):1163–1181, 2014.

[46] V. Utkin. Variable structure systems with sliding modes. *IEEE Transactions on Automatic Control*, 22(2):212–222, 1977.

[47] Y. Shtessel, C. Edwards, L. Fridman, A. Levant, et al. *Sliding Mode Control and Observation*, volume 10. Springer New York, New York, NY, 2014.

[48] J. J. Slotine and S. S. Sastry. Tracking control of non-linear systems using sliding surfaces with application to robot manipulators. In *1983 American Control Conference*, pages 132–135, 1983.

[49] T. C. Manjunath. Design of moving sliding surfaces in a variable structure plant and chattering phenomena. *International Journal of Mechanical and Mechatronics Engineering*, 1(9):536 – 542, 2007.

[50] B. Draženović. The invariance conditions in variable structure systems. *Automatica*, 5(3):287–295, 1969.

[51] V. Utkin. *Sliding Modes in Control and Optimization*. Springer Berlin Heidelberg, Berlin, Heidelberg, DE, 1992.

[52] E. A. Barbashin. *Introduction to the theory of stability*. Wolters-Noordhoff Publishing, Groningen, NL, 1970.

[53] J. J. Slotine, W. Li, et al. *Applied Nonlinear Control*. Prentice Hall, Englewood Cliffs, NJ, 1991.

[54] V. Utkin and H. Lee. Chattering problem in sliding mode control systems. In *International Workshop on Variable Structure Systems, 2006. VSS'06.*, pages 346–350, 2006.

[55] A. Swikir and V. Utkin. Chattering analysis of conventional and super twisting sliding mode control algorithm. In *2016 14th International Workshop on Variable Structure Systems (VSS)*, pages 98–102, 2016.

[56] V. Utkin and H. Lee. The chattering analysis. In *2006 12th International Power Electronics and Motion Control Conference*, pages 2014–2019, 2006.

[57] K. D. Young, V. Utkin, and U. Ozguner. A control engineer's guide to sliding mode control. *IEEE Transactions on Control Systems Technology*, 7(3):328–342, 1999.

[58] A. Levant. Sliding order and sliding accuracy in sliding mode control. *International Journal of Control*, 58(6):1247–1263, 1993.

[59] L. Fridman and A. Levant. Higher order sliding modes as a natural phenomenon in control theory. In *Robust Control via Variable Structure and Lyapunov Techniques*, pages 107–133. Springer, 1996.

[60] A. Levant. Universal single-input-single-output (SISO) sliding-mode controllers with finite-time convergence. *IEEE Transactions on Automatic Control*, 46(9):1447–1451, 2001.

[61] F. Plestan, Y. Shtessel, V. Bregeault, and A. Poznyak. New methodologies for adaptive sliding mode control. *International journal of control*, 83(9):1907–1919, 2010.

[62] F. Plestan, Y. Shtessel, V. Brégeault, and A. Poznyak. Sliding mode control with gain adaptation—application to an electropneumatic actuator. *Control Engineering Practice*, 21(5):679–688, 2013.

[63] C. W. Tao, M. L. Chan, and T. T. Lee. Adaptive fuzzy sliding mode controller for linear systems with mismatched time-varying uncertainties. *IEEE Transactions on Systems, Man, and Cybernetics, Part B (Cybernetics)*, 33(2):283–294, 2003.

[64] D. Munoz and D. Sbarbaro. An adaptive sliding-mode controller for discrete nonlinear systems. *IEEE Transactions on Industrial Electronics*, 47(3):574–581, 2000.

[65] S. L. Shi, J. X. Li, and Y. M. Fang. Extended-state-observer-based chattering free sliding mode control for nonlinear systems with mismatched disturbance. *IEEE Access*, 6:22952–22957, 2018.

[66] Y. Tang, J. Li, S. Li, Q. Cao, and Y. Wu. Non-linear extended state observer-based sliding mode control for a direct-driven wind energy conversion system with permanent magnet synchronous generator. *The Journal of Engineering*, 2019(15):613–617, 2019.

[67] J. J. Slotine and S. S. Sastry. Tracking control of non-linear systems using sliding surfaces with application to robot manipulators. *International Journal of Control*, 38(2):465–492, 1983.

[68] J. J. Slotine. Sliding controller design for non-linear systems. *International Journal of Control*, 40(2):421–434, 1984.

[69] L. Fridman, J. A. Moreno, B. Bandyopadhyay, S. Kamal, and A. Chalanga. Continuous nested algorithms: The fifth generation of sliding mode controllers. In *Recent Advances in Sliding Modes: From Control to Intelligent Mechatronics*, pages 5–35. Springer International Publishing, Cham, CH, 2015.

[70] G. Bartolini, A. Ferrara, and E. Usai. Chattering avoidance by second-order sliding mode control. *IEEE Transactions on Automatic Control*, 43(2):241–246, 1998.

[71] A. Levant. Principles of 2-sliding mode design. *Automatica*, 43(4):576–586, 2007.

[72] L. Fridman, A. Levant, et al. Higher order sliding modes. In *Sliding Mode Control in Engineering*, chapter 3. CRC Press, Boca Raton, FL, 2002.

[73] A. Levant. Robust exact differentiation via sliding mode technique. *Automatica*, 34(3):379–384, 1998.

[74] A. Levant and L. Fridman. Robustness issues of 2-sliding mode control. In *Variable structure systems: from principles to implementation*, volume 66 of *Control Engineering*, chapter 6. Institution of Engineering and Technology, Stevenage, UK, 2004.

[75] Y. Shtessel, J. A. Moreno, F. Plestan, L. Fridman, and A. Poznyak. Super-twisting adaptive sliding mode control: A Lyapunov design. In *49th IEEE Conference on Decision and Control (CDC)*, pages 5109–5113. IEEE, 2010.

[76] I. Boiko and L. Fridman. Analysis of chattering in continuous sliding-mode controllers. *IEEE Transactions on Automatic Control*, 50(9):1442–1446, 2005.

[77] V. Utkin. Sliding mode control. In *Control Systems, Robotics and Automation–Volume XIII: Nonlinear, Distributed, and Time Delay Systems-II*, pages 130–152. EOLSS Publications, Oxford, UK, 2009.

[78] A. Dávila, J. A. Moreno, and L. Fridman. Variable gains super-twisting algorithm: A Lyapunov based design. In *Proceedings of the 2010 American Control Conference*, pages 968–973. IEEE, 2010.

[79] D. Munoz and D. Sbarbaro. An adaptive sliding-mode controller for discrete nonlinear systems. *IEEE Transactions on Industrial Electronics*, 47(3):574–581, 2000.

[80] C. W. Tao, M. L. Chan, and T. T. Lee. Adaptive fuzzy sliding mode controller for linear systems with mismatched time-varying uncertainties. *IEEE Transactions on Systems, Man, and Cybernetics, Part B (Cybernetics)*, 33(2):283–294, 2003.

[81] Y. J. Huang, T. C. Kuo, and S. H. Chang. Adaptive sliding-mode control for nonlinearsystems with uncertain parameters. *IEEE Transactions on Systems, Man, and Cybernetics, Part B (Cybernetics)*, 38(2):534–539, 2008.

[82] H. Lee and V. Utkin. Chattering suppression methods in sliding mode control systems. *Annual Reviews in Control*, 31(2):179–188, 2007.

[83] Y. Shtessel, C. Edwards, L. Fridman, and A. Levant. Introduction: Intuitive theory of sliding mode control. In *Sliding Mode Control and Observation*, volume 10, chapter 1. Springer New York, New York, NY, 2014.

[84] S. P. Bhat and D. S. Bernstein. Finite-time stability of continuous autonomous systems. *SIAM Journal on Control and Optimization*, 38(3):751–766, 2000.

[85] H. K. Khalil. *Nonlinear Systems*. Pearson Education. Prentice Hall, Upper Saddle River, NJ, 3rd edition, 2002.

[86] T. Sands. *Advances in Spacecraft Attitude Control*. IntechOpen, Rijeka, Jan 2020.

[87] S. R. Vadali. Variable-structure control of spacecraft large-angle maneuvers. *Journal of Guidance, Control, and Dynamics*, 9(2):235–239, 1986.

[88] K. Lu, Y. Xia, Z. Zhu, and M. V. Basin. Sliding mode attitude tracking of rigid spacecraft with disturbances. *Journal of the Franklin Institute*, 349(2):413–440, 2012. Advances in Guidance and Control of Aerospace Vehicles using Sliding Mode Control and Observation Techniques.

[89] C. Pukdeboon, A. S. I. Zinober, and M. W. L. Thein. Quasi-continuous higher order sliding-mode controllers for spacecraft-attitude-tracking maneuvers. *IEEE Transactions on Industrial Electronics*, 57(4):1436–1444, 2010.

[90] S. Shao, Q. Zong, B. Tian, and F. Wang. Finite-time sliding mode attitude control for rigid spacecraft without angular velocity measurement. *Journal of the Franklin Institute*, 354(12):4656–4674, 2017.

[91] H. Du and S. Li. Finite-time cooperative attitude control of multiple spacecraft using terminal sliding mode control technique. *International Journal of Modelling, Identification and Control*, 16(4):327–333, 2012.

[92] N. Zhou, Y. Xia, M. Wang, and M. Fu. Finite-time attitude control of multiple rigid spacecraft using terminal sliding mode. *International Journal of Robust and Nonlinear Control*, 25(12):1862–1876, 2015.

[93] S. Eshghi and R. Varatharajoo. Nonsingular terminal sliding mode control technique for attitude tracking problem of a small satellite with combined energy and attitude control system (ceacs). *Aerospace Science and Technology*, 76:14–26, 2018.

[94] J. Qiao, Z. Li, J. Xu, and X. Yu. Composite nonsingular terminal sliding mode attitude controller for spacecraft with actuator dynamics under matched and mismatched disturbances. *IEEE Transactions on Industrial Informatics*, 16(2):1153–1162, 2020.

[95] Y. Miao, I. Hwang, M. Liu, and F. Wang. Adaptive fast nonsingular terminal sliding mode control for attitude tracking of flexible spacecraft with rotating appendage. *Aerospace Science and Technology*, 93:105312, 2019.

[96] M. Jones, E. Gomez, A. Mantineo, and U. K. Mortensen. Introducing ecss software-engineering standards within esa. *EASA bulletin*, 2002.

[97] Y. Pan, C. Yang, L. Pan, and H. Yu. Integral sliding mode control: performance, modification, and improvement. *IEEE Transactions on Industrial Informatics*, 14(7):3087–3096, 2017.

[98] V. Utkin and J. Shi. Integral sliding mode in systems operating under uncertainty conditions. In *Proceedings of 35th IEEE Conference on Decision and Control*, volume 4, pages 4591–4596 vol.4, 1996.

[99] R. Chai, A. Tsourdos, A. Savvaris, S. Chai, Y. Xia, and C.L. Philip Chen. Review of advanced guidance and control algorithms for space/aerospace vehicles. *Progress in Aerospace Sciences*, 122:100696, 2021.

[100] O. Eray and S. Tokat. The design of a fractional-order sliding mode controller with a time-varying sliding surface. *Transactions of the Institute of Measurement and Control*, 42(16):3196–3215, 2020.

[101] A. Bartoszewicz and A. Nowacka-Leverton. Time-varying sliding modes for the second order systems. In *Time-Varying Sliding Modes for Second and Third Order Systems*, chapter 2. Springer Berlin Heidelberg, Berlin, Heidelberg, 2009.

[102] S. Tokat, M. S. Fadali, and O. Eray. A classification and overview of sliding mode controller sliding surface design methods. In X. Yu and M. Önder Efe, editors, *Recent Advances in Sliding Modes: From Control to Intelligent Mechatronics*, pages 417–439. Springer International Publishing, Cham, CH, 2015.

[103] S. B. Choi, D. W. Park, and S. Jayasuriya. A time-varying sliding surface for fast and robust tracking control of second-order uncertain systems. *Automatica*, 30(5):899–904, 1994.

[104] A. Bartoszewicz. A comment on 'a time-varying sliding surface for fast and robust tracking control of second-order uncertain systems'. *Automatica*, 31(12):1893–1895, 1995. Trends in System Identification.

[105] F. Betin, D. Pinchon, and G. A. Capolino. A time-varying sliding surface for robust position control of a DC motor drive. *IEEE Transactions on Industrial Electronics*, 49(2):462–473, 2002.

[106] A. Sivert, F. Betin, A. Faqir, and G. A. Capolino. Robust control of an induction machine drive using a time-varying sliding surface. In *2004 IEEE International Symposium on Industrial Electronics*, volume 2, pages 1369–1374, 2004.

[107] A. Bartoszewicz and J. Zuk. Time-varying switching lines for VSC of robot manipulators. *Sborník vědeckých prací Vysoké školy báňské - Technické univerzity Ostrava. Řada strojní [online]*, 52(2):13–18, 2006.

[108] S. Tokat. Sliding mode controlled bioreactor using a time-varying sliding surface. *Transactions of the Institute of Measurement and Control*, 31(5):435–456, 2009.

[109] A. Bartoszewicz. Time-varying sliding modes for second-order systems. *IEE Proceedings-Control Theory and Applications*, 143(5):455–462, 1996.

[110] S. Tokat, I. Eksin, and M. Güzelkaya. A new design method for sliding mode controllers using a linear time-varying sliding surface. *Proceedings of the Institution of Mechanical Engineers, Part I: Journal of Systems and Control Engineering*, 216(6):455–466, 2002.

[111] H. Temeltas. A fuzzy adaptation technique for sliding mode controllers. In *IEEE International Symposium on Industrial Electronics. Proceedings*, volume 1, pages 110–115, 1998.

[112] H. Lee, E. Kim, H. J. Kang, and M. Park. Design of a sliding mode controller with fuzzy sliding surfaces. *IEE Proceedings-Control Theory and Applications*, 145(5):411–418, 1998.

[113] Q. P. Ha, D. C. Rye, and H. F. Durrant-Whyte. Fuzzy moving sliding mode control with application to robotic manipulators. *Automatica*, 35(4):607–616, 1999.

[114] S. Tokat, I. Eksin, and M. Güzelkaya. New approaches for on-line tuning of the linear sliding surface slope in sliding mode controllers. *Turkish Journal of Electrical Engineering and Computer Sciences*, 11(1):45–54, 01 2003.

[115] F. Yorgancıoğlu and H. Komurcugil. Single-input fuzzy-like moving sliding surface approach to the sliding mode control. *Electrical Engineering*, 90:199–207, 02 2008.

[116] H. Komurcugil. Rotating-sliding-line-based sliding-mode control for single-phase ups inverters. *IEEE Transactions on Industrial Electronics*, 59(10):3719–3726, 2011.

[117] B. Iliev and I. Hristozov. Variable structure control using Takagi-Sugeno fuzzy system as a sliding surface. In *2002 IEEE World Congress on Computational Intelligence. 2002 IEEE International Conference on Fuzzy Systems. FUZZ-IEEE'02. Proceedings*, volume 1, pages 644–649. IEEE, 2002.

[118] J. B. Pomet and L. Praly. Adaptive nonlinear regulation: Estimation from the Lyapunov equation. *IEEE Transactions on Automatic Control*, 37(6):729–740, 1992.

[119] D. Peaucelle and H. Leduc. Adaptive control design with S-variable LMI approach for robustness and l2 performance. *International Journal of Control*, 93(2):194–203, 2020.

[120] C. Pittet, J. Mignot, and C. Fallet. LMI based multi-objective H infty control of flexible microsatellites. *Proceedings of the IEEE Conference on Decision and Control*, 4:4000 – 4005 vol.4, 02 2000.

Appendix A

Flexible spacecraft

This appendix presents the flexible spacecraft used for numerical simulations in Sections 5.3 and 5.4, and modeled how explained in Subsection 2.68. Therefore, this spacecraft consists of a main rigid body (Figure A.1a) to which four flexible solar panels (Figure A.1b) are attached as shown in Figure A.1c. In addition, the mass and dimensions of both the main body and the solar panels in their respective reference frames are in Table A.1.

In order to build the mathematical model of the spacecraft attitude dynamics (2.68), (2.64), which includes the flexibility of the solar panels, it is necessary to obtain the natural modes of the solar panels. Therefore, a FEM analysis is conducted with *Patran/Nastran*, realizing the geometry in Patran with a central surface that represents the top part of the satellite, and the four surfaces for the solar panels as in Figure A.2. The panels are modelled as aluminium plates with the 2D shell property. The body is assumed to be rigid, and the four surfaces are connected to it through a fixed constraint. In Figure A.2, it can be noted a mesh with quad-elements. Then, a modal analysis is performed using the solver Nastran to obtain the natural modes of

Table A.1 Size of the spacecraft

mass of the main body [kg]	143
size of the main body $(x \times y \times z)$ [m]	$0.9 \times 1.1 \times 0.8$
mass of each solar panel [kg]	3.6
size of each solar panel $(x \times y \times z)$ [m]	$1.1 \times 0.002 \times 0.6$

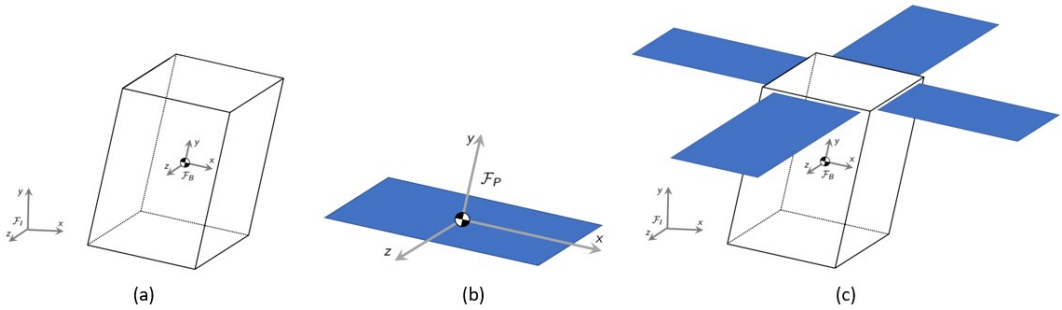

Fig. A.1 Spacecraft main rigid body (a), solar panels (b), assembly (c)

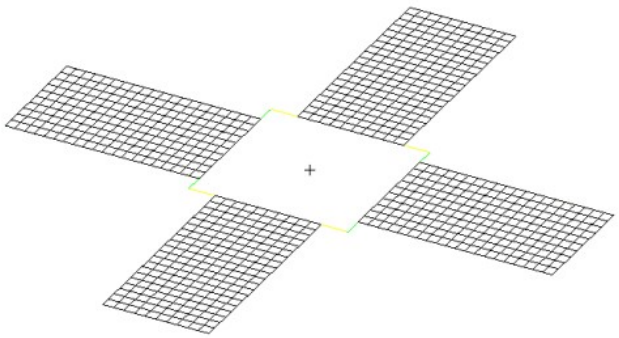

Fig. A.2 Solar panels model on Patran

the structures, and the first three are used to build the mathematical model of attitude dynamics. In particular, the first is a bending mode (Figure A.3), the second one is a torsional mode (Figure A.4), and the third one is again a bending mode (Figure A.5). As discussed in Subsection 2.2.3, for each natural mode we need both the natural frequency and eigenvectors corresponding to the centre of the mass of the sub-panels in which each panel is divided. In this work, each panel is divided in 9 sub-panels (Figure A.10) to compute the cupling matrix δ, as detailed in Subsection 2.2.3, and the eigenvectors of the nodes corresponding to the centre of the mass of each sub-panels are in Figures A.6 to A.9, where T and R are translational and rotational eigenvectors respectively, and associated to the axis given by the subscript. Instead, the natural frequencies are in Table A.2.

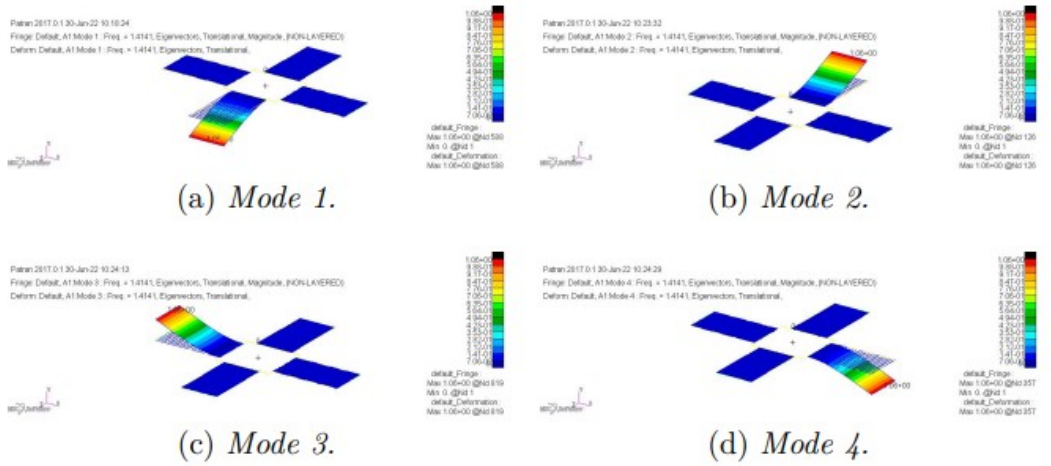

(a) *Mode 1.* (b) *Mode 2.* (c) *Mode 3.* (d) *Mode 4.*

Fig. A.3 First bending mode, panel 1 (a), panel 2 (c), panel 3 (b), and panel 4 (d)

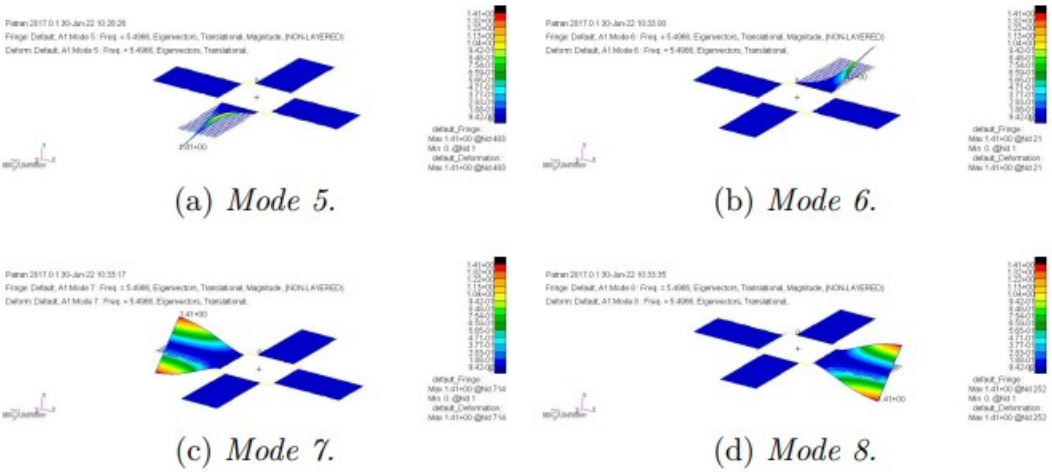

(a) *Mode 5.* (b) *Mode 6.* (c) *Mode 7.* (d) *Mode 8.*

Fig. A.4 Torsional mode, panel 1 (a), panel 2 (c), panel 3 (b), and panel 4 (d)

Table A.2 Natural frequencies of the first three natural modes

First bending mode	$f_1 = 0.141$ Hz
First torsional mode	$f_2 = 0.550$ Hz
Second bending mode	$f_3 = 0.877$ Hz

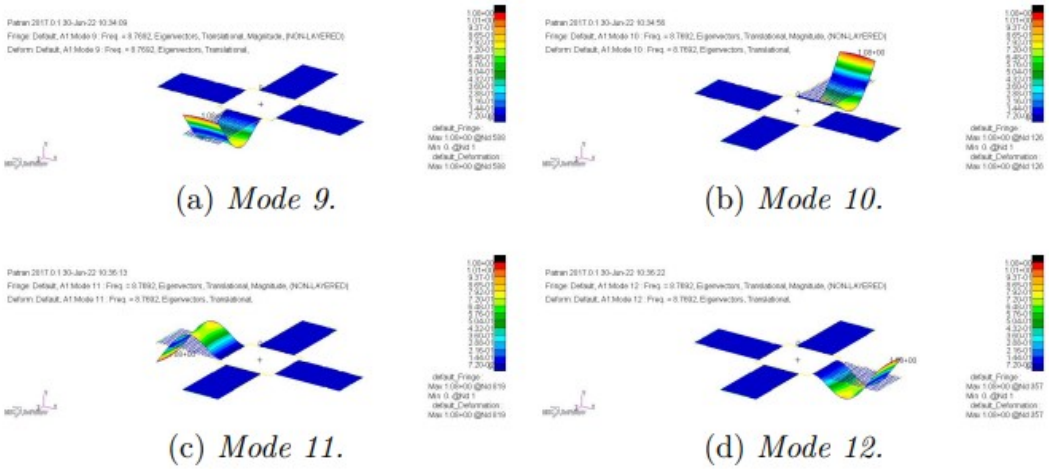

(a) *Mode 9.* (b) *Mode 10.*

(c) *Mode 11.* (d) *Mode 12.*

Fig. A.5 Second bending mode, panel 1 (a), panel 2 (c), panel 3 (b), and panel 4 (d)

	T_x	T_y	T_z	R_x	R_y	R_z
	First bending mode					
sub-panels 1 to 9	-3.310853E-19	-7.628315E-01	-2.828233E-18	2.777559E-02	2.415653E-18	-1.322813E+00
	5.467767E-20	-7.654160E-01	-2.765073E-18	-2.537359E-11	1.887323E-18	-1.317519E+00
	3.468879E-19	-7.628315E-01	-2.731578E-18	-2.777558E-02	1.628657E-18	-1.322813E+00
	-3.593901E-19	-3.530964E-01	-1.907780E-18	5.386637E-02	2.948408E-18	-1.117007E+00
	-5.049281E-20	-3.578381E-01	-1.881371E-18	-1.926588E-11	2.567427E-18	-1.111641E+00
	2.913170E-19	-3.530964E-01	-1.993296E-18	-5.386635E-02	2.958794E-18	-1.117007E+00
	-2.761151E-19	-6.543202E-02	-7.391529E-19	4.461358E-02	2.403925E-18	-5.667112E-01
	-7.755915E-20	-6.882154E-02	-6.870753E-19	-7.012529E-11	2.410411E-18	-5.843091E-01
	1.541466E-19	-6.543202E-02	-6.880580E-19	-4.461356E-02	2.961422E-18	-5.667113E-01
	First torsional mode					
sub-panels 1 to 9	8.921770E-20	7.618907E-01	3.627079E-19	4.201039E+00	-1.374472E-19	5.521415E-01
	7.507493E-20	-5.611015E-11	3.504754E-19	4.248955E+00	8.739796E-20	1.184077E-09
	7.647196E-20	-7.618905E-01	3.412121E-19	4.201039E+00	1.962530E-19	-5.521414E-01
	8.706548E-20	5.007568E-01	3.479745E-19	2.770658E+00	-2.579623E-19	1.010085E+00
	6.453506E-20	-1.912377E-10	3.346168E-19	2.787315E+00	-1.625388E-19	-3.784443E-10
	3.981887E-20	-5.007567E-01	3.592888E-19	2.770658E+00	-3.122116E-19	-1.010085E+00
	6.571060E-20	1.415457E-01	1.472655E-19	8.034177E-01	-3.622329E-19	1.023372E+00
	3.452031E-20	3.079585E-11	1.371372E-19	7.770521E-01	-4.439681E-19	-5.168720E-10
	1.315367E-20	-1.415457E-01	1.328694E-19	8.034177E-01	-5.589394E-19	-1.023371E+00
	Second bending mode					
sub-panels 1 to 9	5.231882E-21	5.690736E-02	5.743460E-20	-4.372769E-01	-3.454068E-20	4.101915E+00
	4.630541E-22	9.681178E-02	5.433632E-20	-4.291923E-09	-1.638468E-20	4.060350E+00
	-2.456847E-21	5.690738E-02	5.331143E-20	4.372768E-01	1.035287E-21	4.101915E+00
	7.859931E-21	-7.508989E-01	4.407063E-20	-4.959589E-01	-4.700948E-20	3.732377E-01
	2.228233E-21	-7.076874E-01	4.530155E-20	-2.833944E-09	-5.016986E-20	4.194617E-01
	-4.172294E-21	-7.508989E-01	4.519157E-20	4.959587E-01	-4.792022E-20	3.732377E-01
	6.704908E-21	-3.113510E-01	1.578354E-20	-1.391993E-01	-4.847731E-20	-2.195539E+00
	3.038687E-21	-2.974399E-01	1.592267E-20	-1.148759E-09	-5.826324E-20	-2.100348E+00
	-2.326183E-21	-3.113510E-01	1.630609E-20	1.391992E-01	-6.601996E-20	-2.195539E+00

Fig. A.6 Eigenvectors of panel 1

	T_x	T_y	T_z	R_x	R_y	R_z
	First bending mode					
sub-panels 1 to 9	5.109702E-19	-7.628296E-01	-5.835513E-19	1.322810E+00	1.375830E-18	2.777551E-02
	5.123039E-19	-7.654141E-01	-3.767009E-19	1.317516E+00	1.427500E-18	1.353546E-12
	4.701035E-19	-7.628296E-01	-2.245691E-19	1.322809E+00	9.029738E-19	-2.777551E-02
	2.580672E-19	-3.530955E-01	-3.733025E-19	1.117005E+00	4.290830E-19	5.386623E-02
	2.292983E-19	-3.578372E-01	-2.692903E-19	1.111638E+00	1.597815E-19	-4.610875E-15
	2.464700E-19	-3.530955E-01	-1.238622E-19	1.117005E+00	9.903982E-20	-5.386621E-02
	1.073111E-19	-6.543187E-02	-1.357185E-19	5.667099E-01	8.328349E-19	4.461347E-02
	1.269033E-19	-6.882138E-02	-7.889096E-21	5.843077E-01	4.191759E-19	-6.518938E-11
	2.108755E-19	-6.543187E-02	-6.111161E-20	5.667099E-01	7.051937E-19	-4.461345E-02
	First torsional mode					
sub-panels 1 to 9	-9.684848E-19	7.618958E-01	4.448490E-19	-5.521452E-01	-2.310478E-18	4.201067E+00
	-9.260966E-19	-5.082161E-11	9.595839E-20	-1.204379E-09	-2.095160E-18	4.248984E+00
	-9.534222E-19	-7.618957E-01	-1.773535E-19	5.521451E-01	-1.600529E-18	4.201067E+00
	-5.250173E-19	5.007602E-01	2.561354E-19	-1.010092E+00	-1.364297E-18	2.770677E+00
	-4.931470E-19	-1.909083E-10	6.062396E-20	3.710291E-10	-4.411098E-19	2.787334E+00
	-5.549789E-19	-5.007601E-01	-1.087215E-19	1.010092E+00	-7.114623E-19	2.770677E+00
	-1.160957E-19	1.415467E-01	1.022323E-19	-1.023379E+00	-9.308913E-19	8.034233E-01
	-1.658790E-19	3.057847E-11	-9.501586E-22	5.182037E-10	-8.584379E-19	7.770575E-01
	-2.466658E-19	-1.415467E-01	-5.401610E-20	1.023378E+00	-1.310854E-18	8.034233E-01
	Second bending mode					
sub-panels 1 to 9	-9.214330E-20	5.690734E-02	1.609336E-20	-4.101912E+00	-1.438416E-19	-4.372765E-01
	-8.901173E-20	9.681173E-02	-7.759855E-21	-4.060347E+00	-1.332846E-19	-4.304835E-09
	-8.779445E-20	5.690736E-02	-3.223710E-20	-4.101912E+00	-1.253138E-19	4.372764E-01
	-5.173412E-20	-7.508983E-01	1.267263E-20	-3.732376E-01	-1.375685E-19	-4.959584E-01
	-4.910736E-20	-7.076869E-01	-7.623330E-21	-4.194616E-01	-1.042799E-19	-2.837498E-09
	-5.125515E-20	-7.508983E-01	-2.401235E-20	-3.732376E-01	-1.023049E-19	4.959583E-01
	-8.797356E-21	-3.113508E-01	5.456149E-21	2.195537E+00	-5.143801E-20	-1.391992E-01
	-1.093600E-20	-2.974397E-01	-1.331667E-21	2.100346E+00	-7.269182E-20	-1.150589E-09
	-1.169311E-20	-3.113508E-01	-1.073946E-20	2.195537E+00	-7.924750E-20	1.391991E-01

Fig. A.7 Eigenvectors of panel 2

	T_x	T_y	T_z	R_x	R_y	R_z
	First bending mode					
sub-panels 1 to 9	-3.946726E-19	7.628315E-01	-1.420171E-18	2.777559E-02	-5.092205E-19	-1.322813E+00
	-2.529749E-19	7.654160E-01	-1.326561E-18	-2.321060E-11	-1.037181E-18	-1.317519E+00
	-3.109992E-20	7.628315E-01	-1.356573E-18	-2.777558E-02	-1.022004E-18	-1.322813E+00
	-3.970630E-19	3.530964E-01	-1.121864E-18	5.386637E-02	-1.516729E-18	-1.117007E+00
	-1.970113E-19	3.578381E-01	-1.075257E-18	-1.688753E-11	-1.596953E-18	-1.111641E+00
	9.616939E-20	3.530964E-01	-1.075053E-18	-5.386635E-02	-1.890674E-18	-1.117007E+00
	-2.452649E-19	6.543202E-02	-3.625204E-19	4.461358E-02	-1.438190E-18	-5.667112E-01
	-3.723995E-20	6.882154E-02	-3.342433E-19	-6.943552E-11	-1.538844E-18	-5.843091E-01
	1.058404E-19	6.543202E-02	-3.205507E-19	-4.461356E-02	-1.311352E-18	-5.667113E-01
	First torsional mode					
sub-panels 1 to 9	-4.295739E-20	-7.618907E-01	-2.946753E-19	4.201039E+00	-1.525420E-19	5.521415E-01
	-1.090028E-22	5.557675E-11	-2.900889E-19	4.248955E+00	-2.831052E-19	1.189043E-09
	7.548028E-20	7.618905E-01	-2.920649E-19	4.201039E+00	-3.089971E-19	-5.521414E-01
	-5.262609E-20	-5.007568E-01	-2.340478E-19	2.770658E+00	-4.132570E-19	1.010085E+00
	6.524030E-21	1.920672E-10	-2.109510E-19	2.787315E+00	-4.319156E-19	-3.765904E-10
	7.443431E-20	5.007567E-01	-1.900359E-19	2.770658E+00	-4.419466E-19	-1.010085E+00
	-4.483653E-20	-1.415457E-01	-5.033211E-20	8.034177E-01	-2.932761E-19	1.023372E+00
	2.101642E-20	-3.041943E-11	-4.314267E-20	7.770521E-01	-4.525168E-19	-5.196646E-10
	4.904311E-20	1.415457E-01	-2.411183E-20	8.034177E-01	-3.545836E-19	-1.023371E+00
	Second bending mode					
sub-panels 1 to 9	3.206943E-20	-5.690736E-02	9.468035E-20	-4.372769E-01	1.255711E-19	4.101915E+00
	1.298693E-20	-9.681178E-02	9.839007E-20	-4.299623E-09	1.224960E-19	4.060350E+00
	-1.225148E-20	-5.690738E-02	9.606017E-20	4.372768E-01	1.288434E-19	4.101915E+00
	2.738711E-20	7.508989E-01	6.171637E-20	-4.959589E-01	1.047643E-19	3.732377E-01
	9.129968E-21	7.076874E-01	5.854910E-20	-2.834026E-09	1.219636E-19	4.194617E-01
	-1.132990E-20	7.508989E-01	5.726428E-20	4.959587E-01	1.337601E-19	3.732377E-01
	1.684352E-20	3.113510E-01	1.276480E-20	-1.391993E-01	9.965743E-20	-2.195539E+00
	-1.632531E-21	2.974399E-01	1.027406E-20	-1.148894E-09	9.997893E-20	-2.100348E+00
	-5.451501E-21	3.113510E-01	6.808561E-21	1.391992E-01	8.628179E-20	-2.195539E+00

Fig. A.8 Eigenvectors of panel 3

	T_x	T_y	T_z	R_x	R_y	R_z
	First bending mode					
sub-panels 1 to 9	-9.504941E-19	7.628296E-01	-2.598029E-20	1.322809E+00	6.668085E-19	2.777551E-02
	-1.010611E-18	7.654141E-01	-1.618745E-19	1.317516E+00	9.874817E-19	8.648523E-11
	-1.052423E-18	7.628296E-01	-3.713508E-19	1.322810E+00	1.497259E-18	-2.777551E-02
	-4.604642E-19	3.530955E-01	3.609893E-20	1.117005E+00	1.625681E-18	5.386621E-02
	-4.596050E-19	3.578372E-01	-1.854141E-19	1.111638E+00	1.350415E-18	5.696387E-11
	-4.973512E-19	3.530955E-01	-3.461548E-19	1.117005E+00	1.211396E-18	-5.386623E-02
	5.138549E-20	6.543187E-02	-4.557028E-21	5.667099E-01	6.566454E-19	4.461345E-02
	1.322441E-20	6.882138E-02	-7.916142E-20	5.843077E-01	3.924514E-19	8.036732E-11
	-1.039634E-19	6.543187E-02	-1.771425E-19	5.667099E-01	8.985522E-19	-4.461347E-02
	First torsional mode					
sub-panels 1 to 9	1.569983E-20	-7.618957E-01	5.719969E-20	-5.521451E-01	2.338012E-19	4.201067E+00
	2.561565E-20	-6.700397E-11	2.403048E-20	1.160239E-09	1.048420E-19	4.248984E+00
	3.795443E-20	7.618958E-01	2.374040E-20	5.521452E-01	-8.528269E-20	4.201067E+00
	-1.437082E-20	-5.007601E-01	2.042716E-20	-1.010092E+00	-2.030516E-19	2.770677E+00
	-1.770229E-20	-1.954140E-10	3.604152E-20	-3.947345E-10	-1.242756E-19	2.787334E+00
	5.219223E-21	5.007602E-01	2.808056E-20	1.010092E+00	-4.218864E-20	2.770677E+00
	-5.286471E-20	-1.415467E-01	1.967709E-20	-1.023378E+00	4.851527E-20	8.034233E-01
	-4.663740E-20	3.021697E-11	6.349899E-21	-5.223604E-10	1.133415E-19	7.770575E-01
	-2.254943E-20	1.415467E-01	1.747875E-20	1.023379E+00	-1.292450E-20	8.034233E-01
	Second bending mode					
sub-panels 1 to 9	5.155362E-20	5.690736E-02	-2.809869E-20	4.101912E+00	-1.898157E-19	4.372764E-01
	4.000886E-20	9.681173E-02	-3.966295E-21	4.060347E+00	-1.142654E-19	-4.283159E-09
	3.315686E-20	5.690734E-02	6.023819E-21	4.101912E+00	-5.562749E-20	-4.372765E-01
	4.178079E-20	-7.508983E-01	-1.985530E-20	3.732376E-01	4.253034E-20	4.959583E-01
	3.462999E-20	-7.076869E-01	-1.715223E-20	4.194616E-01	-2.676557E-20	-2.835874E-09
	3.273435E-20	-7.508983E-01	-1.494439E-22	3.732376E-01	-5.893640E-20	-4.959584E-01
	3.572766E-20	-3.113508E-01	-1.825802E-20	-2.195537E+00	-6.951261E-20	1.391991E-01
	3.022775E-20	-2.974397E-01	-5.977194E-21	-2.100346E+00	-6.047725E-20	-1.151323E-09
	1.082473E-20	-3.113508E-01	-6.495585E-21	-2.195537E+00	-1.081609E-20	-1.391992E-01

Fig. A.9 Eigenvectors of panel 4

With the data in Figures A.6 to A.9, the truncated matrix of eigenvectors $\overline{\Phi}$ for each solar panel is as follows:

$$\overline{\Phi}^T = \begin{bmatrix} (T_{x_1}^1 & \dots & R_{z_1}^1) & \dots & (T_{x_9}^1 & \dots & R_{z_9}^1) \\ \vdots & \vdots & \vdots & \vdots & \vdots & \vdots & \vdots \\ (T_{x_1}^3 & \dots & R_{z_1}^3) & \dots & (T_{x_9}^3 & \dots & R_{z_9}^3) \end{bmatrix}, \tag{A.1}$$

where the subscript 1-9 is referred to each sub-panel (see Figure A.10), while the apex 1-3 is referred to the natural mode. By applying the division shown in Figure A.10 to each solar panel, we obtain R and r for each sub-panel, which are the position vector from the center of the mass of the spacecraft to the point on the interface between the rigid body and the flexible appendage and the position vector from the point on the interface between the rigid body and the flexible appendage and the center of mass of the sub-body i respectively, as described in Subsection 2.2.3. These quantities are extrapolated from the geometry of the satellite, as is the generalized inertia matrix of sub-bodies M. Indeed, each sub-panel i has mass m_i and dimensions

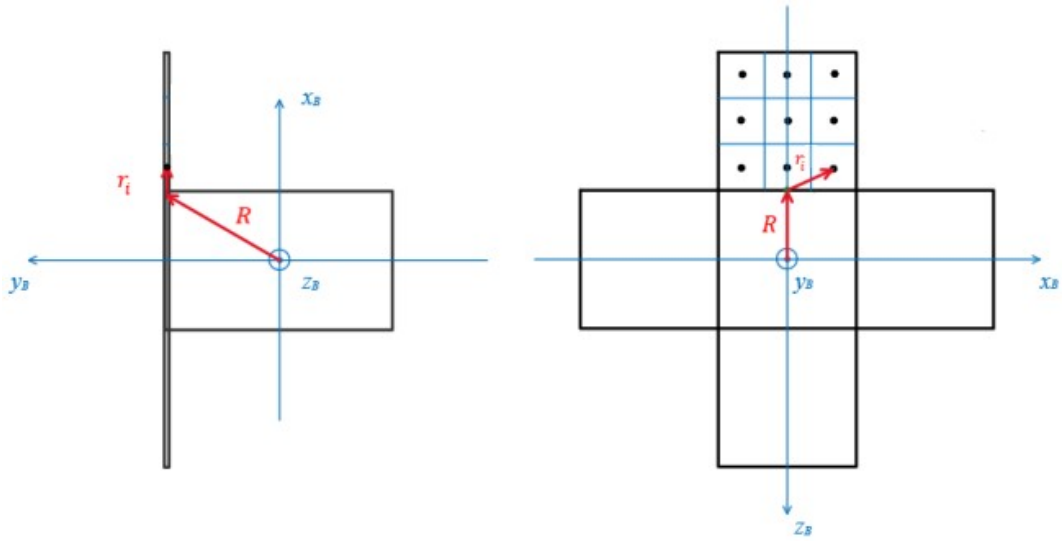

Fig. A.10 Front and upper view of spacecraft with sub-panels division

l_{x_i}, l_{y_i}, and l_{z_i} as follows:

$$m_i = \frac{m_{\text{sp}}}{9}, \quad l_{x_i} = \frac{l_{x_{\text{sp}}}}{3}, \; l_{y_i} = l_{y_{\text{sp}}}, \; l_{z_i} = \frac{l_{z_{\text{sp}}}}{3}, \tag{A.2}$$

where m_{sp}, $l_{x_{\text{sp}}}$, $l_{y_{\text{sp}}}$, $l_{z_{\text{sp}}}$ are the mass of a solar panel and its dimensions in the frame in Figure A.1b. Therefore, the inertia tensor of the sub-body i is

$$J_i = \frac{m_i}{12} \begin{bmatrix} l_{y_i}^2 + l_{z_i}^2 & 0 & 0 \\ 0 & l_{x_i}^2 + l_{z_i}^2 & 0 \\ 0 & 0 & l_{x_i}^2 + l_{y_i}^2 \end{bmatrix}, \tag{A.3}$$

and M_i is obtained as in eq. (2.59). We now have all the instruments to apply eq. (2.58) and can then calculate the coupling matrix for each solar panel, the result of which is in Table 5.4. Finally, the stiffness matrix K is obtained from the natural frequencies in Table A.2 by means of eq. (2.65), and the results are also in Table 5.4.